Characterization, Experimentation and Modeling of Mn-Fe-Si-P Magnetocaloric Materials.

by

Theodor Victor Christiaanse
B.Eng., TH-Rijswijk, Netherlands, 2009
M.Sc., Technical University of Delft, Netherlands, 2013

A Dissertation Submitted in Partial Fulfillment of the
Requirements for the Degree of

DOCTOR OF PHILOSOPHY

in the Department of Mechanical Engineering

Characterization, Experimentation and Modeling of Mn-Fe-Si-P Magnetocaloric Materials.

by

Theodor Victor Christiaanse
B.Eng., TH-Rijswijk, Netherlands, 2009
M.Sc., Technical University of Delft, Netherlands, 2013

Supervisory Committee

Dr. Andrew Rowe, Supervisor
(Mechanical Engineering - University of Victoria)

Dr. Mohsen Akbari, Departmental Member
(Mechanical Engineering - University of Victoria)

Dr. Jens Bornemann, Outside Member
(Electrical and Computer Engineering - University of Victoria)

Supervisory Committee

Dr. Andrew Rowe, Supervisor
(Mechanical Engineering - University of Victoria)

Dr. Mohsen Akbari, Departmental Member
(Mechanical Engineering - University of Victoria)

Dr. Jens Bornemann, Outside Member
(Electrical and Computer Engineering - University of Victoria)

ABSTRACT

The objective of this work is to assess the potential of Mn-Fe-Si-P for magnetic heat pump applications. Mn-Fe-Si-P is a first order transition magnetocaloric material made from safe and abundantly available constituents. A significant magnetocaloric effect occurs at the transition temperature of the material. The transition temperature can be tuned by changing the atom ratios to a region near room temperature.

Mn-Fe-Si-P in magnetic heat pumps is investigated by determining the material's properties, 1D system modeling and experiments in a magnetic heat pump prototype. We characterize six samples of Mn-Fe-Si-P, based on their heat capacity and magnetization. The reversible component of the adiabatic temperature change is found from the entropy diagram and compared to cyclic adiabatic temperature change measurements. Five of the six samples are selected to be formed into epoxy fixed crushed particulate beds, which can be installed into a magnetic heat pump prototype.

A system model is constructed to understand the losses of the magnetic heat pump prototype. Several experiments are performed with Gd with rejection temperatures around room temperature. Including dead volume and casing losses improves the modeling outcomes to match the experimental results closer.

Experiments with Mn-Fe-Si-P are performed. Five materials are formed into modular beds that can be combined into two layer configurations. Six experimental configurations are tested, one single layer regenerator test with a passive lead second layer, and five experiments using two layers with varying transition temperature spacing between the materials. The best performance of the beds was found at close spacing at suitable rejection temperatures. It was found that at far spacing, the performance of stronger materials would produce a lower temperature span than that of weaker materials at close spacing.

The experiments provide results that are used to validate the system modeling approach using the material data obtained of the Mn-Fe-Si-P samples. We integrate material properties into a system model. A framework is proposed to take into account the hysteresis. This framework shows an improvement of the predicted trend for a single layer case. The proximity of simulation and experimental multi-layering results are dependent on the rejection temperature. At the higher end of the rejection temperature the modeling results over-predict the temperature span around the active region. At lower rejection temperatures the simulation under predicts the experimental temperature span. The inclusion of experimental pressure drop improved the trends found at higher rejection temperatures. A further improvement was found varying the interstitial heat transfer term. Modeling future research should focus on characterizing the thermo-hydraulic closure relationships for crushed particulate epoxy fixed beds, and improvements to the heat loss model.

Mn-Fe-Si-P is able to produce a temperature span, when a suitable set of Mn-Fe-Si-P materials are selected based on minimal hysteresis, making it a viable material for magnetic heat pump applications. The performance of Mn-Fe-Si-P is further improved by layering materials with closely spaced transition temperature. Future research should focus on increasing the production of Mn-Fe-Si-P materials with low hysteresis, and improving the regenerator matrix geometry and stability.

Table of Contents

List of Tables

List of Figures

Abbreviations

AMR	Active Magnetic Regenerator	-
AVE	Anhysteretic low field to Anhysteretic high field thermal path	-
CC	Cooling low field to Cooling high field thermal path	-
CH	Cooling low field to Heating high field thermal path	-
$\mathrm{COP_c}$	Coefficient Of Cooling Power	-
ΔT_{ad}	Adiabatic Temperature Change	K
Δs_{mag}	Specific Magnetic Entropy Change	J/kgK
FOM	First Order Transition Material	-
FWHM	Full Width Half Maximum	K
GHG	Greenhouse Gasses	-
GS	Glass Spheres	-
HCFC	Hydrochlorofluorocarbons	-
HC	Heating low field to Cooling high field thermal path	-
HFC	Hydrofluorocarbons	-
HH	Heating low field to Heating high field thermal path	-
mDSC	In-field Differential Scanning Calorimeter	-
MCE	Magnetocaloric Effect	-
MCM	Magnetocaloric Material	-
PM1	Permanent Magnetic Refrigeration Prototype 1	
RCP	Relative Cooling Potential	J/kg
SOM	Second Order Transition Material	-

VSM	Vibrating Scanning Magnetometer
VV	Void Volume

Chemical elements

As	Arsenic	-
B	Boron	-
Ca	Calcium	-
Co	Cobalt	-
Dy	Dysprosium	-
Er	Erbium	-
Fe	Iron	-
Gd	Gadolinium	-
H	Hydrogen	-
Ho	Holmium	-
La	Lanthanum	-
Mn	Manganese	-
O	Oxygen	-
P	Phosphorus	-
Si	Silicon	-
Sr	Strontium	-
Tb	Terbium,	-
Y	Yttrium	-

List of Symbols

A	Surface Area	m^2
B	Magnetic Field	T
Bi	Biot Number	–
c	Specific Heat Capacity	J/kgK
C	Numerical Heat Capacitance Term	J/mK
d	Added Length	m
D	Diameter	m
DF	Degrading Factor	–
E	Exergetic Cooling Power	W
f	Frequency	Hz
F	Numerical Mass Transport Term	W/K
f_0	Adjustable Function	–
Fo	Fourier Number	–
h	Heat Transfer Coefficient	$\mathrm{W/m^2K}$
H	Magnetic Field	A/m
k	Thermal Conductivity	W/mK
K	Numerical Conduction Term	W/K
L	Length	m
L	Numerical Loss Term	W/mK
m	Mass	kg
$\dot{m}$	Mass Flow Rate	kg/s

M	Magnetic Moment per unit Mass	Am^2/kg
$\mathcal{N}$	Demagnetising Factor	–
n_{amr}	Number of Regenerators PM1	2
Nu	Nusselt Number	–
p	Pressure	N/m^2
P	Perimeter	m
Pe	Peclet Number	–
Pr	Prandtl Number	–
Q	Power	W
r	Radius	m
Re	Reynolds Number	–
R_m	Magnetic Field Reduction Factor	–
s	Specific Entropy	J/kgK
S	Numerical Source Term	W/mK
T	Temperature	K
t	Time	s
$\tilde{t}$	Nondimensionalized Time	-
U	Global Heat Transfer Coefficient	W/m^{2}K
u_d	Darcy Flow	m/s
V	Volume	m^3
$\dot{V}$	Volumetric Flow Rate	m^3/s
W	Work	J
w_o	Time Step Weighting Factor	–
z	Spatial Axis	m
$\tilde{z}$	Nondimensionalized Length	–

Greek Symbols

α	Thermal Diffusivity	m^2/s
α_o	Weighting Function	–

α_{ch}	Material Properties Selection Parameter	$-$
β	Specific Surface Area per unit Volume	$\mathrm{m}^2/\mathrm{m}^3$
ϵ	Porosity	$-$
η_m	Q_{MCE} material reduction factor	$-$
θ	Rotational Angle	degree
Λ_o	Dead Volume fraction	$-$
ϕ_H	Degrading Factor	$-$
μ	Dynamic Viscosity	$\mathrm{Pa} \cdot \mathrm{s}$
μ_0	Vacuum Permeability	N/A^2
ρ	Density	m^3/kg
τ	Cycle Period	s
Ω	Numerical Interstitial Heat Transfer Term	W/K

Subscripts	
air	Air
amb	Ambient
an	Anhysteretic
apl	Applied
bl	Base Line
c	critical values, refers to the regenerator
$casing$	Casing
co	Cooling
$cold$	Cold side
cy	Cycle
d	Displaced/Displacer
de	Demagnetization
eff	Effective
f	Fluid
f	Final

fs	Field Shift
gr	Gross
$g10$	G10 tubing
he	Heating
$high$	High Position
hot	Hot side
$housing$	Housing
i	Numerical Node Index
i	Initial
int	Internal
$leak$	Leak
low	Low Position
ls	Lead Spheres
max	Maximum
net	Net Cooling Power
o	Void / Dead Volume
r	Regenerator
rh	Regenerator Housing
s	Solid
sh	Shape
sp	Sphere
$span$	Temperature Difference Hot and Cold side
$ultem$	Ultem

Superscript

’	Per unit length	$1/m$
*	Dummy Integration Variable	
n	Numerical Temporal Node Index	

ACKNOWLEDGEMENTS

I would like to thank:

Andrew Rowe for sending me to the gym, mentoring, support, encouragement, and patience.

Paulo V. Trevizoli for mentoring me and helping me to write my publications.

Rodney Katz is the biggest asset of the UVic engineering department. He has taught me everything I know how to optimally use machines, craft drawings and design prototypes.

Research Colleague's and Friends, Reed Teyber, Iman Niknia, Oliver Campbell, Prem Govindappa whom have been inspiring to work with. There is some true courage and intelligence that goes through this program and I'm happy to have had such great peers.

My Parents and friends for supporting me throughout this process. It has been a bumpy road with lots of ups and down.

Pauline and Sue for organising the IESVic coffee and supporting me throughout my PhD. You keep and make IESVic feel alive and a community.

BASF New Business, BASF Netherlands, BASF SE Throughout my PhD I have had a wonderful experience due to the efforts of the BASF team. I had the opportunity to work with several professionals at BASF. I would like to thank, in no specific order, Sumohan Misra for producing the materials I needed. Florian Scharf for being inquisitive and guiding. David van Asten and Lian Zhang for diligently working on gathering the material data. Colman Carroll and Markus Schwind for producing the regenerator beds. Daniel Barrera-Medrano as team leader you are always upbeat and motivating. And multiple others, among them Florian Doetz and Bennie Reesink .

Natural Sciences and Engineering Research Council & Compute Canada
for their support of this research.

Chapter 1

Introduction

1.1 Background

Vapour compression heat pump systems provide heating and refrigeration for a broad range of applications; however, vapour compression refrigeration systems are subjected to increasing regulations concerning refrigerant use [1, 2]. The regulations concern the fade out of refrigerants based on Hydrofluorocarbon's (HFC's) and hydrochlorofluorocarbon's (HCFC's). HFC's and HCFC's are powerful greenhouse gases (GHG) and ozone depleting substances. Currently, these refrigerants are used by an estimated 3 billion operating refrigeration devices, and 7.8 % of global greenhouse gases are attributed to refrigeration. With roughly two-thirds due to indirect emissions; carbon emissions from grid scale electricity production. The other one-third are direct emissions of refrigerants, which leak into the atmosphere during maintenance or improper handling of the units at end-of-life [3]. Developing replacements for these refrigerants is currently a major field of research [4]. Hydrocarbons have shown to be a good alternative for small domestic applications, and CO_2 for large scale industrial applications [4]. Hydrocarbons are flammable and bring with them safety concerns. However, it is projected that in 2020 75 % of domestic refrigeration units sold will use isobutane (HC-600a). As for CO_2, it requires high pressures and costly equipment. Recent developments in CO_2 system have made them a viable option and are finding adoption in Europe mainly [5]. Vapour compression continues to be researched; however, other novel technologies are sought out to provide a combination of higher energy efficiency and use only environmentally friendly materials and liquids.

Magnetic refrigeration is seen as a promising alternative to vapour-compression cycles due to high theoretical efficiency and use of benign heat transfer liquids [6, 7]. If the high theoretical efficiency is realized and implemented, significant amounts of primary energy and CO_2 emissions are mitigated by electricity savings. The use of benign liquids eliminates the use of refrigerants and therefore, removes the danger of these GHG leaking into the atmosphere. An additional benefit is that the compressors can be replaced with a pump, suggesting quieter refrigeration systems could be realized.

Magnetic heat pumps were exclusively used for cryogenic applications before the seminal paper of Brown [8]. Brown was able to achieve a temperature span of 47 °C around room temperature using a 7 T superconducting magnet. Near room temperature, Gadolonium (Gd) temperature increases with approximately 15 °C when exposed to a field from a 7.5 T field change [9]. Brown showed that this temperature increase could be enhanced by regeneration of a fluid column. Barclay and Steyert describe the opposite principle in their patent [10], where heat transfer fluid is oscillated while a porous matrix of Gd material is used as the regenerator. By alternating the heat transfer fluid and magnetic field a temperature gradient is created in the regenerator. This device is called the *active magnetic regenerator* (AMR). The AMR functions as a *passive* regenerator, responsible for the heat exchange between the porous matrix and the heat transfer liquid as well as an *active* component referring to the temperature change in the solid as a function of applied field values. Using the AMR design, Zimm et al. show that magnetic refrigeration can achieve similar cooling power and coefficient of power (COP) as vapour compression. Zimm et al. present a refrigerator capable of producing 500 W of cooling power with a COP of five with a temperature span 12 K [11].

The commercialization of efficient magnetic heat pumps still face challenges with respect to the design of an apparatus and the active materials used [12, 13]. Trevizoli et al. highlight some of the main loss mechanisms that need to be addressed to increase performance of the magnetic heat pump: demagnetizing effects, housing heat leaks and dead volume losses, to name some. These issues will be discussed at length later. The active materials used are known as magnetocaloric materials. These materials exhibit a temperature change and entropy change with varying magnetic field termed the magnetocaloric effect (MCE). The magnitude of these properties impact magnetic heat pump performance. An additional challenge is that these materials also need to be shaped into effective regenerators with a low pressure drop, while maintaining a high volumetric density [14]. Lastly, the materials should remain intact and maintain their MCE properties during cycling.

Mn-Fe-Si-P is a novel magnetocaloric material which consists of abundantly available non-toxic constituents [15]. It provides a substantial MCE effect around its transition temperature, and the transition temperature can be tuned near room temperature by changing the ratio of the constituents used. These benefits make Mn-Fe-Si-P a prime contender as a magnetocaloric material for commercial, high efficiency magnetic heat pumps.

1.2 Magnetocaloric Effect

The magnetocaloric effect (MCE) is the physical phenomena that powers magnetic heat pumps. The MCE is characterized by two components, the entropy change due to magnetic ordering, and the adiabatic temperature change, both driven by changing magnetic field values. In Fig. 1.1, a representative entropy diagram, demonstrates the field and temperature dependence of a magnetocaloric material. For a given temperature, the high field entropy curve is lower than the low field entropy curve. The resulting isothermal specific entropy change, Δs, and adiabatic isentropic temperature change, ΔT_{ad}, are shown for an arbitrary temperature at zero applied field.

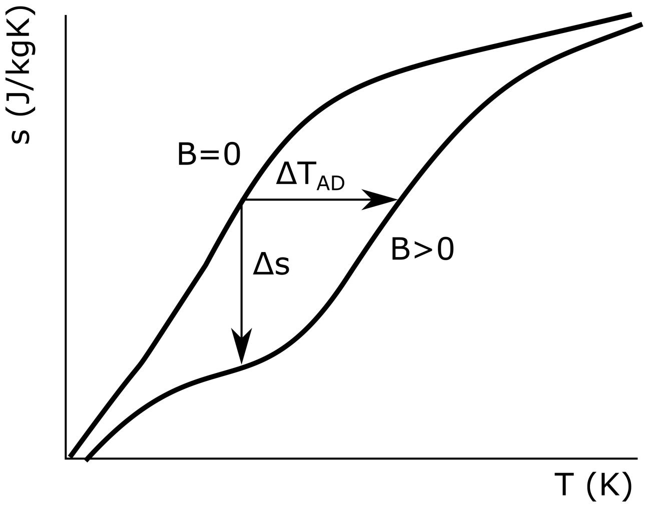

Figure 1.1: A sketch of the entropy diagram of a magnetocaloric material at the transition temperature.

In the ordinary magnetocaloric effect, when the magnetic field is increased the temperature of the solid increases. Subsequently, when the field is removed the temperature of the solid decreases. Likewise, the application of a magnetic field results in a decrease in entropy, while the removal of field results in a increase in entropy.

A large MCE is associated with the presence of a phase change. Magnetocaloric materials are classified into two types of phase changes. A distinction is made between first order (FOM) and second order (SOM) transitions material. Theoretically, the FOM's exhibits a discontinuity in the first order differential of the entropy at the 'Curie' or transition temperature, Eq. 1.1. Whereas, SOM's exhibit a discontinuity in the second order differential of the entropy, Eq. 1.2. In real systems the discontinuity of the first order transition is not found due to impurities and spatial variations in material composition. However, the transition is distinct from the second order transition due to a latent heat at the transition temperature [13].

$$\text{First order} \quad \left(\frac{\partial S}{\partial T}\right) = \text{undefined} \qquad \text{at } T = T_C \tag{1.1}$$

$$\text{Second order} \quad \left(\frac{\partial^2 S}{\partial T^2}\right) = \text{undefined} \qquad \text{at } T = T_C \tag{1.2}$$

Gd is used as a benchmark material for magnetocaloric heat pumps. This material undergoes a second order magnetic transition near 293 K. The origin of the second order transition of the Gd material is the transition from the ferromagnetic to paramagnetic state at the 'Curie' temperature [16, 13]. The transition temperature can be tuned between 235K and 293K by forming alloys of Gd with Dysprosium (Dy), Terbium (Tb), Yttrium(Y), or Erbium (Er). The second order transition materials (SOM's) are easy to characterize [17] and can be modeled theoretically using mean field theory [16]. As such, they are often used for prototype testing and modeling; however, Gd and these other rare-earth constituents are costly and therefore difficult to commercialize.

Mn-Fe-Si-P is a novel first order transition material. The first order transition in Mn-Fe-Si-P material is classified as a magneto-elastic first order transition [18]. Here the lattice symmetry remains unchanged, but there is an anisotropic change in the cell parameters $\Delta c/a$ [19]. Unlike FOM's La(Fe,Co,Si)H or Mn-Fe-As-P, it does not contain any rare-earth elements or toxic elements. The first order transition of this material brings with it two challenging aspects. The first is the hysteresis which accompanies the first order transition. For example, in Fig. 1.2 the infield specific heat of Gd [17] and a sample of Mn-Fe-Si-P [20] is shown at 0 T and 1 T. The hysteresis in the Mn-Fe-Si-P material is characterized by measuring the properties while heating and cooling the samples. For Mn-Fe-Si-P, the difference in specific heat peak for fixed field values is due to the hysteresis of the samples. The hysteresis in these materials can be reduced by careful selection of the right constituent ratios, purity, and production process.

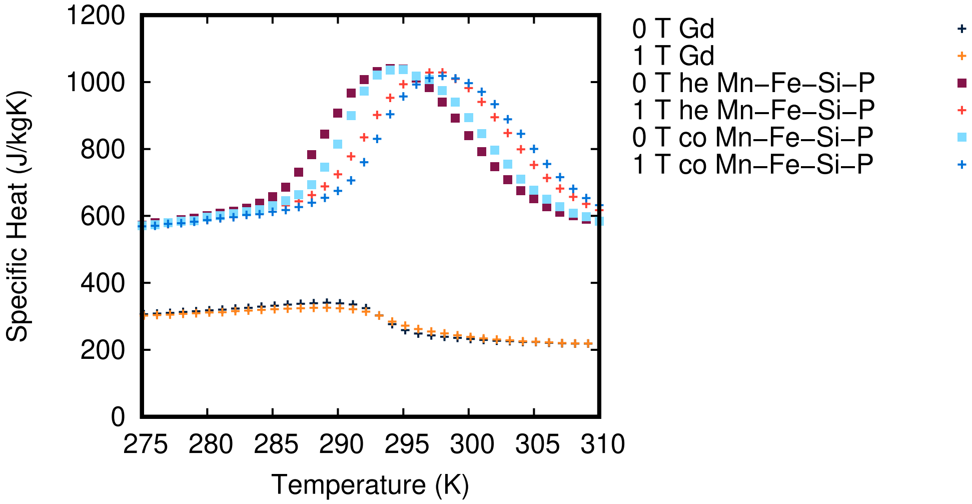

Figure 1.2: The specific heat of Gd compared to a sample of Mn-Fe-Si-P material. For Mn-Fe-Si-P the heating (he) and cooling (co) curves are presented at 0 T and 1 T.

The second challenge with Mn-Fe-Si-P is the limited range in which these materials exhibit a useful MCE. The MCE is distributed as a peak around the transition temperature. The width of this peak, for moderate field changes of 1 T, in SOM's can exceed 20 K, while in FOM's this is often below 10 K. To overcome this limited temperature range, FOM's have to be layered in a AMR system. We will first discuss the active magnetic regenerator cycle and follow with the layering of materials in an AMR.

1.3 Active Magnetic Regenerator Cycle

Using the magnetocaloric effect a magnetic heat pump cycle can be designed [21]. A magnetocaloric cycle based on the Brayton cycle goes through four steps to provide cooling. In Fig. 1.3 a depiction of this regenerator cycle is shown, the image follows the following four steps:

Step one: The field is applied, increasing the temperature of the regenerator throughout the bed. The red line indicates the rise of the average temperature of the bed with applying field from the starting temperature indicated by the dotted state.

Step two: A piston moves fluid from the cold to the hot side. This is called the cold blow of the cycle. The fluid colder than the regenerator removes the heat from the regenerator. A decrease in temperature is indicated by the blue solid line from the last temperature state of step one depicted by the dotted line. The removed heat from the regenerator is rejected using the hot side heat exchanger (HEX).

Step three: The field is removed from the regenerator, lowering the temperature of the regenerator. The new temperature along the bed is represented by the solid line.

Step four: The piston moves back to the original position pushing fluid from the hot side to the cold side. This is called the hot blow of the cycle. The regenerator at a colder temperature than the fluid removes heat from the fluid hence cooling the fluid. This chilled fluid can be used to absorb heat at the cold heat exchanger.

Back to step one: The cycle can return to the first step to continue pumping heat.

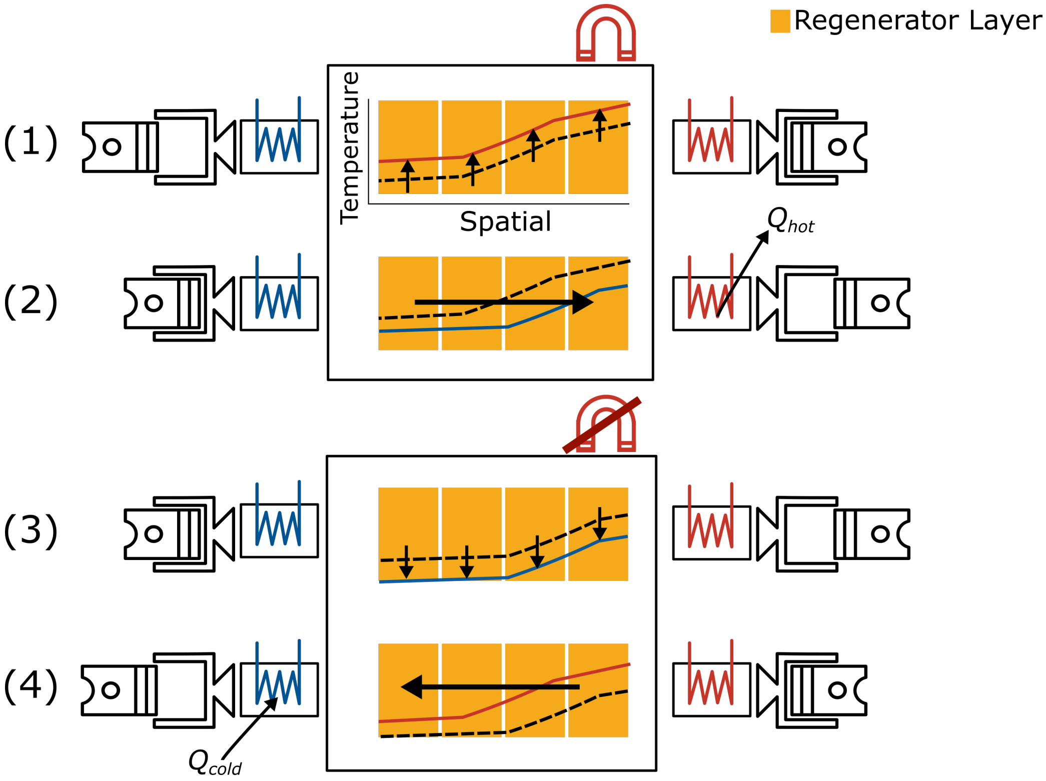

Figure 1.3: Four step process of the active regenerative process. The solid line is the current temperature profile along the regenerator while the dotted line is temperature from the previous step.

Ideally, the regenerator produces a larger temperature span than a single stage magnetic cycle. Each layer of the regenerator goes through its own thermodynamic Brayton cycle. Since the MCE is temperature dependent, each layer's MCE can be tuned to an expected temperature for each location in the regenerator. Mn-Fe-Si-P MCE can be tuned between a lower bound temperature of 220 K and a higher bound temperature of 380 K [15], making it ideal for room temperature applications. By layering various Mn-Fe-Si-P samples with cascading transition temperatures in an AMR, MCE properties are maintained along the regenerator temperature gradient. This effectively provides a consistent MCE along the designed regenerator temperature gradient.

1.4 Layering of Materials

The entropy change and adiabatic temperature change for magnetocaloric materials are bound to a limited temperature region. To expand the operating temperature of a regenerator, multiple magnetocaloric materials are cascaded to cover a broader temperature range. Fig. 1.4 and Fig. 1.5 show how multiple Mn-Fe-Si-P materials compare to Gd based on their entropy change and adiabatic temperature change, respectively. A single Mn-Fe-Si-P material would not perform well due to the limited temperature region where the material is active. Multiple materials, however, span a large temperature range. As can be seen in Fig. 1.4, the entropy change is much larger for Mn-Fe-Si-P, while, in Fig. 1.5, the adiabatic temperature change is less than Gd.

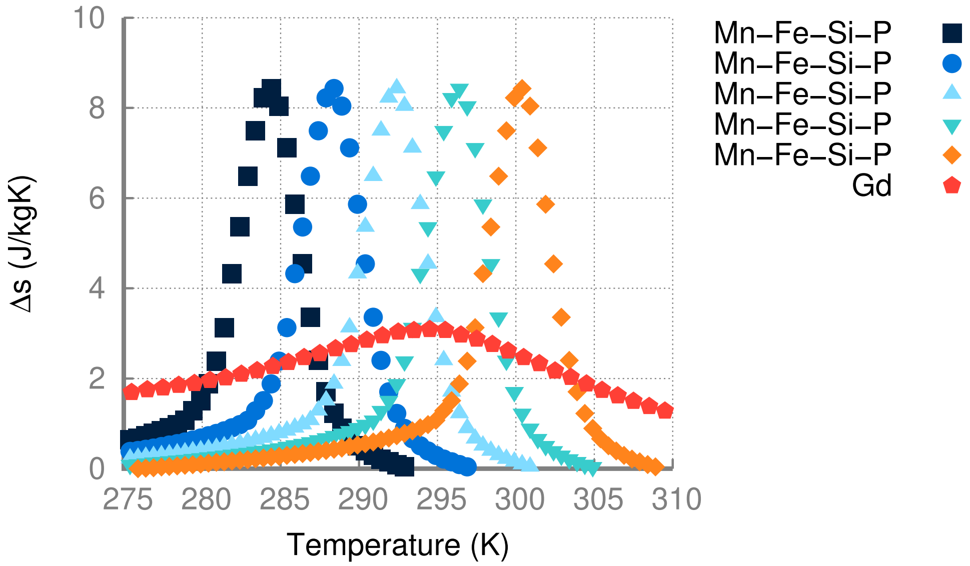

Figure 1.4: Entropy change of five Mn-Fe-Si-P materials shifted with transition temperature compared to Gd for a magnetic field value change of 0 to 1 T.

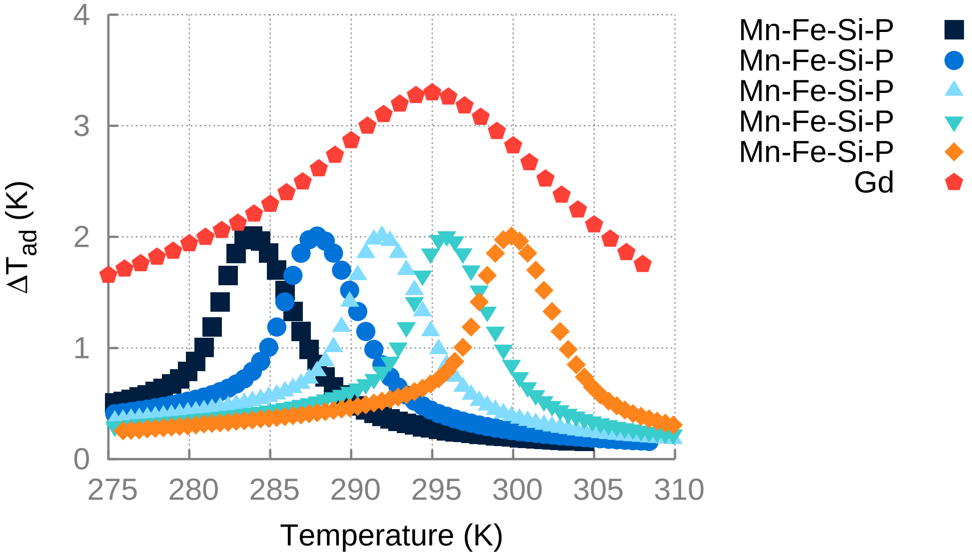

Figure 1.5: Adiabatic temperature change of five Mn-Fe-Si-P materials shifted with transition temperature compared to Gd for a magnetic field value change of 0 to 1 T.

The materials need to be optimally distributed along the regenerator. From experimental work, we have found that the temperature gradient along the regenerator is dependent on the active region of the materials used in that layering. The active region of FOM's is defined by their adiabatic temperature change curves full width half maximum [22, 20]. Govindappa et al. showed that the active region is correlated to the maximum temperature span that can be obtained in layering experiments [22]. Some trends emerge from the experimental literature review for layered AMR experiments (See Table A.1 for a summary). The transition temperature of SOM's tend to be spaced further apart from each other than FOM's. This is due to their broad active region. The stronger the magnetic field, the larger the active region becomes of each material, the Curie spacing between the layers may be increased [23, 24, 25, 26], in contrast low fields demand a closer spacing [27]. FOM's that are spaced apart further than 5 °C often not fully utilize all layers given that FOM FWHM's are smaller than those of SOM's. In most experimental studies the maximum temperature span condition will span the operating range of the materials. In some of the reviewed experimental works this was not achieved [23, 28, 29, 30, 22].

There are various reasons for not all materials being utilized in the experiments with layered AMR's. Several aspects are important to creating a temperature span, which includes the active region of all the materials in the regenerator:

1. Heat transfer properties between fluid and MCM
2. Casing heat leaks
3. MCM selection
4. Optimized operating parameters

The heat transfer properties between the fluid, are important to couple the temperature change of the materials to the fluid temperature change. Tušek et al. showed that when plates are used, the fluid is unable to interact with the plates optimally. This results in the colder layers inability to further increase the temperature span [31]. The heat transfer properties depend on the geometry of the regenerator and operating conditions of the experiment. Different geometries have been evaluated for their heat transfer characteristics and losses [14].

Heat leaks are unwanted interactions with the ambient environment. These heat leaks occur at the heat exchangers and along the casing housing the regenerator. The casing heat leaks inject heat at each point along the regenerator, increasing the cooling power needed to maintain the temperature span [32]. Using an interface thermocouple between two layers of SOM's Teyber et al. showed that the temperature gradient may be disturbed by casing heat leaks [33].

The selection of the materials is important as they determine the active region of the AMR. When materials are selected where the active region is spaced too far apart the temperature span may not be the result of all layers. For example, Green et al. layer two SOM's in a AMR. The AMR uses Gd and Tb as first and second layer, respectively, with a Curie temperature of 293 and 235 K [23]. The Gd layer is unable to lower the heat transfer gas temperature to within the temperature that Tb becomes active [23]. For FOM's, this temperature difference between layers may be much smaller at which we see this failure. Legait et al. used a set of FOM's and spaced the transition temperature between the materials further than 5 °C, resulting in a temperature span that did not cover all material's active regions [28].

Typically, experimental settings can be optimized by changing the rejection temperature, displaced volume and frequency of a device. For some conditions, increasing the displaced volume and frequency can mitigate the impact of the heat leaks [34]. Govindappa et al. also showed the importance of layer thickness and operating conditions [22]. Using eight layers of Mn-Fe-As-P, it was found that a regenerator using shorter layers was unable to build a temperature span covering the range of all materials, as compared to a regenerator using thicker layers where this condition was achieved. At low displaced volume, in a six layer configuration, the temperature span only span the first three layer's active region. When the displaced volume is increased, the temperature span was found to span all the layers.

1.5 Modeling

Modeling of the regenerator system can improve understanding of experimental results. Several modeling studies have been performed examining layered regenerators: first order materials [35, 36, 37], second order materials [38, 39, 40, 41, 42, 43, 33] and comparing first and second order materials [44, 35, 45, 46].

Most modeling approaches are based on 1D numerical methods [47]. A comparison between a 1D and 2D model of a thin plate regenerator showed little differences in modeling outcomes for temperature span and cooling power [48]. Recently, 3D models have been developed for AMR applications using software packages FLUENT [46] and OpenFOAM [49]. These models incur a larger computational cost than 1D modeling approaches. Simplified modeling approaches exist for AMR that treat the AMR as a single heat pump unit [39, 50, 51]. Another simplified method uses a thermodynamic analysis of the magnetic Erickson cycle [42]. 1D methods have shown to produce good agreement in modeling the peak obtained temperature span, when considering layered FOM's [45]. Modeling provides detailed insight on emergent performance of the system due to material and system design choices.

The distinction between implementing FOM's and SOM's in to 1D modeling is due to the material properties. The material properties of the FOM's vary sharply with magnetic field and temperature compared to SOM's. This leads in some models to the use of a high number of temporal nodes. For example, for SOM's 400 time nodes was sufficient [52], for FOM's Monfared and Palm use 8000 time steps [41] and Zhang et al. use 40000 time nodes [37].

An additional difficulty is the implementation of the hysteresis of the first order transition. Hysteresis results in entropy generation at the transition and results in history dependent values for specific heat, magnetisation and entropy of the material. The hysteresis has been numerically implemented by reducing the magnetocaloric effect with an irreversible magnetisation component [35], by using only the reversible adiabatic temperature change [53, 20]. Both these techniques have been adopted in modeling to account for the hysteresis; however, more validation is needed to determine the accuracy of these methods.

Methods to understand the history dependent behaviour of the magnetocaloric materials is an active area of research. Success has been made with Preisach modeling [54, 55]. Preisach modeling has shown to reproduce the temporal behaviour of magnetocaloric material Gd-Si-Ge for fixed temperature and field values [56]. However, no implementation has been made combining Preisach modeling with 1D modeling as of yet.

1.6 Objectives and Approach

The objective of this work is to assess the potential of Mn-Fe-Si-P for magnet heat pump applications. The materials exhibit a first order transition at the transition temperature. A significant magnetocaloric effect is found in a small temperature region around the transition temperature that is linked to the ratio of the constituents

[57]. To achieve large temperature span, the materials need to be layered in an AMR. To properly understand the optimal layering strategy using these material samples, a system model needs to be developed that captures the details of experiments. Using this model,the size of each layer and order of materials can be optimized for a magnetic heat pump system.

The investigation of Mn-Fe-Si-P materials involves the following steps:

1. Characterize material properties;
2. development of system model;
3. experimental study of layered FOM's in AMR; and,
4. a numerical study of the experimental results.

In the first step, six samples of Mn-Fe-Si-P are characterized based on their infield-specific heat capacity and magnetization data [58]. The first five samples are selected based on low hysteresis and transition temperatures around room temperature. The sixth sample is selected with a large hysteresis. The hysteresis, inherent in these samples, is determined by measuring the material's properties in heating and cooling direction. The entropy diagram based on this measured data is constructed for heating and cooling direction [53]. The adiabatic temperature change is measured using a direct measurement that cycles the material in and out of an applied field. This cyclically measured direct measurement represents the reversible component of the adiabatic temperature change [59]. The adiabatic temperature change from the entropy diagram is compared to this cyclically measured adiabatic temperature change to determine the function of the materials in an AMR cycle [20].

In the second step, a system model is developed to simulate a permanent magnet prototype device under experimental conditions [60]. The model is based on a 1D numerical approach that provides a good balance between experimental details and computational cost [47]. The model is validated using a well known material, Gd, as magnetocaloric material. Key device parameters of the system are dead volume and casing losses. A set of experiments are designed to test varying dead volume and casing boundary condition assumptions.

The third step involves testing of regenerator structures in a permanent magnet prototype device. Five of the previously characterized materials are used to construct regenerator consisting of two layers. The set of experiments use a variation of transition temperature spacing between layers. This allows us to understand how transition temperature spacing impacts the performance of the temperature span versus the rejection temperature [61].

Finally, the two layer experimental data is studied numerical using the model. The Mn-Fe-Si-P material data is used in the model taking into account the hysteresis of each material. Simulation outcomes are compared to the experimental Mn-Fe-Si-P multi layering dataset. The validation of the layered FOM model provides a tool for future work to include optimization of the Mn-Fe-Si-P layered structures.

1.7 Outline of the Thesis

The thesis is based on a sequence of papers. Each Chapter is a paper published, under review or to be submitted.

In Chapter 2, we describe the characterization of six samples of Mn-Fe-Si-P materials. The demagnetizing field corrected entropy diagram is constructed for each of the materials from magnetization and infield-specific heat. Due to the thermal hysteresis of these samples they are characterized by measuring the properties while applying (heating) and removing (cooling) heat. Cyclic adiabatic temperature change measurements are made of each of the samples to find the reversible component of the adiabatic temperature change. The adiabatic temperature is reconstructed from the entropy diagrams to be compared to the cyclic adiabatic temperature change measurements.

In Chapter 3, we outline the system model developed for the PM1. The heat leaks of the system need to be understood using regenerator of a known substance to understand the material models of the first order materials. Loss models are outlined to find a good fit between Gd regenerator experimental results and the system model.

In Chapter 4, a layering study using FOM's Mn-Fe-Si-P is presented. The layering study uses five of the previously measured and studied Mn-Fe-Si-P samples. The samples are tested in six different configurations which have different transition temperature spacing between the layers. The beds are tested for zero and 2 W net loading conditions at rejection temperatures between 9 and 40 °C.

In Chapter 5, the FOM data is incorporated in the system model. The material data is incorporated using a new material model, which takes into account the hysteresis of each sample and allows for continuously varying applied magnetic field. The results of the model are compared to the experimental results from Chapter 4.

In Chapter 6, conclusions and recommendations of future work on the use of Mn-Fe-Si-P for AMR applications is given.

Chapter 2

Materials

The content of this Chapter is published, Journal of Physics D:Applied Physics. The methods, experimental data and validation methods described in this Chapter are published [20]. The paper discusses the validation of the entropy diagram by comparing the constructed adiabatic temperature change from the entropy to the measured adiabatic temperature change.

A concise approach for building the s-T diagram for Mn-Fe-P-Si hysteretic magnetocaloric material

T.V. Christiaanse[1], O. Campbell[1], P.V. Trevizoli[1], Sumohan Misra[2], David van Asten[3], Lian Zhang[3], P. Govindappa[1], I. Niknia[1], R. Teyber[1], A. Rowe[1]

[1]University of Victoria, Victoria, B.C. Canada
[2]BASF SE Ludwigshafen, Luwigshafen am Rhein, Germany
[3]BASF Nederland, De Meern, The Netherlands

Accurate material data is important to understand the functioning of these materials in the AMR. Material data is gathered for six samples of Mn-Fe-Si-P materials with the purpose to model experimental data.

2.1 Abstract

The use of first order transition magnetocaloric materials (FOM's) in magnetic cycles is of interest for the development of efficient magnetic heat pumps. FOM present promising magnetocaloric properties; however, hysteresis reduces the reversible adiabatic temperature change (ΔT_{ad}) of these materials and, consequently, impacts the performance of a magnetic heat pump. The present chapter evaluates the reversible ΔT_{ad} in a FOM. Six samples of the Mn-Fe-P-Si material with different transition temperatures are examined. The samples are measured for heat capacity, magnetization, and adiabatic temperature change using heating and cooling protocols to characterize hysteresis. After correcting demagnetizing fields, the entropy-temperature (s-T) diagrams are constructed and used to calculate adiabatic temperature change using four different thermal paths. The post-calculated ΔT_{ad} is compared with experimental data from direct ΔT_{ad} measurements. Most of the samples of Mn-Fe-P-Si show that post-calculated ΔT_{ad} resulting from the heating zero field and cooling in-field entropy curves align best with the ΔT_{ad} measurements. The impact of the demagnetizing field is shown in term of absolute variation to the post-calculated ΔT_{ad}. A simplified model is used to explain observed data sensitivities in the post-calculated ΔT_{ad}.

2.2 Introduction

First order transition magnetocaloric materials (FOM's) are of interest, as they can be an inexpensive alternative to more costly materials used in state-of-the-art magnetocaloric refrigeration [62, 13]. The magnetocaloric effect (MCE) which manifests as reversible temperature and entropy change is the driving force in the operation of a magnetic cycle. FOM exhibit a large MCE around a narrow temperature range near the order-disorder transition temperature. Arranging materials in layers according to transition temperature, also known as cascading, creating an active magnetic regenerator (AMR) has been proposed to overcome the narrow MCE [10]. A layered AMR comprised of FOM's should equal or better the performance that can be achieved with conventional, and more expensive, rare earth materials [19]. However, the impact of the thermal and magnetic hysteresis that are inherent to FOM's [63], can result in poor performance. This is a topic in need of in-depth investigation [13, 53].

The development of numerical models with reliable FOM magnetocaloric properties is essential to evaluate the technology potential, understand the physics of the AMR and optimize design parameters [47]. In numerical modeling, the magnetocaloric effect is commonly implemented via an entropy-temperature (s-T) diagram of the material. From the s-T diagram the magnetic field induced adiabatic temperature change (ΔT_{ad}), from any temperature, can be computed assuming hysteresis is negligible. Nevertheless, building the s-T diagrams from sample measurements is not straightforward. There are three methods described in the literature to determine the s-T diagram. One approach is the use of magnetization data and zero field specific heat [64]. The second method is the so-called direct measurement of the entropy change [65, 54] and the third, and most commonly used, is combining in-field specific heat data with magnetization data [66].

The last method is used in this paper to construct the s-T diagram. The specific heat and magnetization data are acquired from two different measurement devices. The specific heat capacity at different isofields is measured with an in-field differential scanning calorimeter (mDSC) [54, 67] and the magnetization is measured with a vibrating scanning magnetometer (VSM) [68]. To validate the constructed s-T diagram, directly measured ΔT_{ad} data is compared to post-calculated ΔT_{ad} [53].

Engelbrecht et al. [53] analysed one sample of $\mathrm{MnFeP_{1-x}As_x}$ FOM (As-alloy) to determine ΔT_{ad} and implemented the resulting properties in an AMR numerical model. In their work, the s-T diagram was constructed from specific heat and magnetization data. Both measurements are repeated when sweeping sample temperatures in a heating and cooling direction as to characterize the thermal hysteresis of the sample. An extensive description of hysteresis characterization can be found in the paper of Basso [69]. Engelbrecht et al.[53] use the heating and cooling at low and high magnetic field leading to create four entropy curves in the s-T diagram. Comparing measured ΔT_{ad} to the post-calculated ΔT_{ad} it is found that for their As-alloy the best match is obtained using an isentropic path between the heating-low field to the cooling-high field entropy curves.

This results in a performance reduction that would be available from other isentropic paths. Von Moos [56] modeled FOM $Ge_5Si_2Ge_2$ by fitting a Preisach model to its magnetization data. The model is tested against directly measured ΔT_{ad} data closely representing the functioning of a AMR. From the model, the ΔT_{ad} extracted from heating-low field and cooling-high field isoterms matched well this functioning.

The Chapters paper advances on the construction of s-T diagrams and evaluation of the ΔT_{ad} in FOM. First, a description of the demagnetizing field correction for the data is presented. Second, six different samples of Mn-Fe-P-Si [15] (Si-alloys) with different ordering temperatures are examined by comparing their direct and post calculated ΔT_{ad} values. Lastly, the s-T diagram construction method is discussed. A simple model of hypothetical FOM is used to identify how several data sensitivities influence the post-calculated ΔT_{ad}. This hypothetical FOM can be manipulated to show the effects of varying the order-disorder transition properties. A detailed description is given in the discussion section.

2.3 Methods

2.3.1 Post-calculating ΔT_{ad} thermal paths from s-T diagrams

The s-T diagram consist of isofield entropy curves constructed based on in-field specific heat and magnetization data. Since Si-alloys exhibit thermal hysteresis, both specific heat and magnetization are experimentally measured following heating and cooling protocols. The heating protocol is defined as data collected while the FOM sample temperature is increased through a temperature range. The opposite definition is true for the cooling protocol. Both protocols are repeated for a range of applied field strengths H (in the present paper $\mu_0 H_{low} = 0$ T). Hence, for a particular H_{high} four different entropy curves are obtained: two for $0T$ and two for H_{high}, from which the ΔT_{ad} is post-calculated following four isentropic paths as presented in Fig. 2.1. The four isentropic paths are: (HH) heating 0 T → heating H_{high}; (CC) cooling 0 T → cooling H_{high}; (CH) cooling 0 T → heating H_{high}; (HC) heating 0 T → cooling H_{high}.

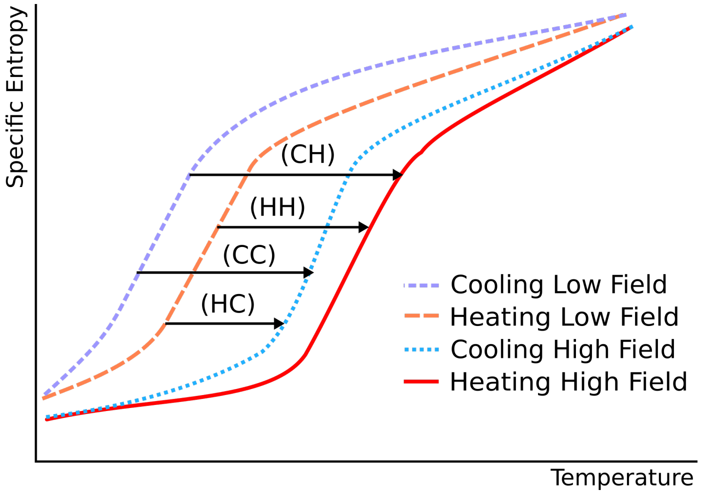

Figure 2.1: Schematic s-T diagram for a FOM illustrating the four possible isentropic paths when magnetizing a FOM: (HH) heating 0 T → heating H_{high}; (CC) cooling 0 T → cooling H_{high}; (CH) cooling 0 T → heating H_{high}; (HC) heating 0 T → cooling H_{high}.

Determining the temperature difference along isentropes between low and high isofield entropy curves ($s(T_i, H)|_{low} = s(T_f, H)|_{high}$) yields the adiabatic temperature change:

$$\Delta T_{ad}\,(T_{\mathrm{i}}, H_{low} \to H_{high}) = T_{\mathrm{f}}(s, H)|_{high} - T_{\mathrm{i}}(s, H)|_{low} \tag{2.1}$$

where, T_{i} is the initial temperature at H_{low} and T_{f} is the final temperature (after applying magnetic field) at H_{high}. In the next section the construction from specific heat and magnetization data to isofield entropy curves is discussed.

2.3.2 Construction of Isofield Entropy Curve

The experimental measurements for specific heat and magnetization are performed over a temperature region of interest. The region of interest starts in the pure ferromagnetic phase and ends in the pure paramagnetic phase. The total entropy $s(T_1, H_1)$ is determined with respect to reference temperature T_1 and field H_1, by changes due to temperature and field. The temperature induced entropy changes found using specific heat:

$$s(T,H) = s(T_1,H) + \int_{T_1}^{T} \frac{c_H(T^*,H)}{T^*} dT^* \tag{2.2}$$

Where T^* is a dummy variable of integration and H is the isofield condition. The entropy change due to magnetic field is computed from the following Maxwell relation:

$$\left(\frac{\partial s}{\partial H}\right)_T = \mu_o \left(\frac{\partial M}{\partial T}\right)_H \tag{2.3}$$

Where M is the magnetic moment per unit mass. By integrating Eq. 2.3, resulting in Eq. 2.4, the entropy change due to field change from H_1 to H at the reference temperature, T_1, is found,

$$\Delta s_{mag}\left(T_1, H_1 \to H\right) = \mu_0 \int_{H_1}^{H} \left(\frac{\partial M(T_1,H^*)}{\partial T}\right)_{H^*} dH^* \tag{2.4}$$

Where H^* is a dummy variable of integration. Combining Eq. 2.2 and Eq. 2.4 the total entropy at a given temperature and field is:

$$s(T,H) = s_{ref}(T_1,H_1) + \int_{T_1}^{T} \frac{c_H(T^*,H)}{T^*} dT^* + \mu_0 \int_{H_1}^{H} \left(\frac{\partial M(T_1,H^*)}{\partial T}\right)_{H^*} dH^* \tag{2.5}$$

The specific heat and magnetization data are measured with two different instruments that utilize different sample receptacles. An accurate construction of entropy using Eq. 2.5 requires magnetization and specific heat data at equivalent internal fields. Therefore, in order to properly make a combination of Eq. 2.2 and Eq. 2.4, the demagnetizing field effect of each instrument needs to be accounted for.

2.3.3 Demagnetizing Field Factors

A sample within the applied magnetic field, H_{apl}, experiences a lower internal field, H_{int}, due to a demagnetizing field, H_{de} [16]:

$$H_{int} = H_{apl} - H_{de} \tag{2.6}$$

The demagnetizing field is a function of magnetization M:

$$H_{de} = \mathcal{N}\rho M(T, H_{int}) \tag{2.7}$$

Where $\mathcal{N}$ is the demagnetizing factor and ρ is the material density. The demagnetizing factor is dependent on the geometric shape and porosity of the sample, as given in Eq. 2.8 [16]. The porosity, ϵ, is taken into account by correcting the demagnetizing shape factor, $\mathcal{N}_{sh}$,

$$\mathcal{N} = \frac{1}{3} + (1 - \epsilon)\left(\mathcal{N}_{sh} - \frac{1}{3}\right) \tag{2.8}$$

Where $\mathcal{N}_{sh}$ is the demagnetizing factor due to the solid body shape equivalent of the receptacle. Eq. 2.8 is for spherical particles which is assumed to approximate the specific heat and magnetization measurements using crushed particulate in a cylindrical receptacle [16]. The demagnetizing factor due to the receptacle shape is based on the inner dimensions of the receptacle. Joseph [70] gives an analytical expression for the demagnetizing factor of a solid cylinder with radius, r, and length, L. For the direct measurements of the ΔT_{ad}, the crushed particulate is housed in a conical structure. A COMSOL 3D finite element simulation is performed to determine the demagnetizing factor of the conical shape. The simulation assumes a solid conical body, with magnetization properties similar to Si-alloys, subjected to an applied field strength equal to the field found in the direct measurement apparatus. The demagnetizing factor is then extracted from the volumetric average internal field of the receptacle. Table 2.1 lists shape and porosity corrected demagnetizing factors for each measurement device. Each device is limited to measure within a temperature range. These temperature ranges are listed in the table 2.1.

Table 2.1: $\mathcal{N}_{sh}$ and $\mathcal{N}$ are shape and correction of porosity. The limited temperature range of each measurement device is additionally listed.

Device	$(1-\epsilon)$	L (mm)	$(2 \cdot r)$ (mm)	$\mathcal{N}_{sh}$	$\mathcal{N}$	Temperature Range
Magnetization	0.66	0.66	2.45	0.619	0.513	250-313
Specific heat	0.5	0.82	5	0.141	0.237	260-321
ΔT_{ad}	0.6			0.406	0.374	251-322

The demagnetizing factors listed are used to correct field values of specific heat, magnetization and ΔT_{ad} experimental data.

2.3.4 Applying the Demagnetizing Field Correction

Magnetization data, M, is corrected first as it is used for the correction of specific heat and ΔT_{ad} measurements. $M(T, H_{int})$ is dependent on internal field but is recorded in terms of applied field, H_{apl}. Combing Eq. 2.7 and Eq. 2.6 the internal field of the sample can be calculated from the measured magnetization, $M(T, H_{int})$, demagnetizing factor, $\mathcal{N} = 0.513$, and the bulk density, ρ, of the sample using the following relationship.

$$H_{int} = H_{apl} - \mathcal{N}\rho M(T, H_{int}) \tag{2.9}$$

The bulk density of the material is estimated to be 6 (g/cm^3) for all samples. At each recorded applied field and temperature point, the demagnetizing field correction is computed to find the internal field. Afterwards, the internal isofield magnetization curves are found by interpolation. The result of this correction for one sample of Si-alloy can be seen in Fig. 2.2. The raw magnetization data is measured in field increments of 0.1 T at lower field values between 0 T and 0.6 T, and increments of

0.2 T between 0.6 T and 2 T. The temperature sweeping rate during the cooling and heating protocol of the magnetometer is 2 K/min. All of the samples are pre-cycled (20x) to remove the virgin effect of the Si-alloy [71].

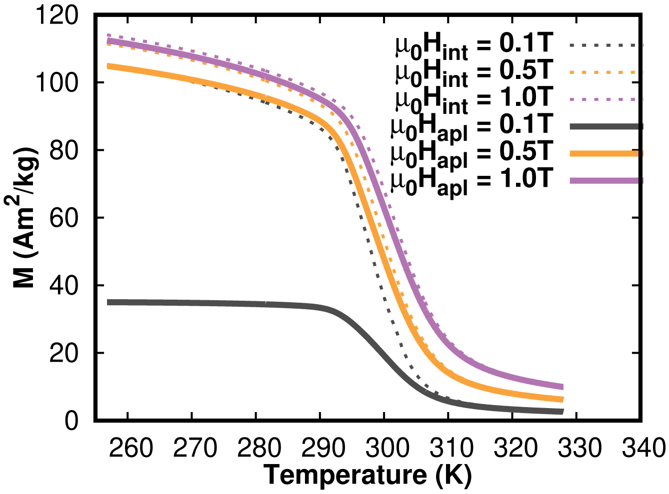

Figure 2.2: Heating magnetization data of a Si-alloy. The dashed lines are magnetization data at constant internal field, H_{int}, while the solid lines are magnetization data at constant applied field, H_{apl}.

The in-field specific heat measurements are performed at a sweeping rate of 3 K/min at 0 T, 1 T and 1.5 T applied field. For each temperature and applied field, internal fields are computed using corrected magnetization data and demagnetizing factor $\mathcal{N} = 0.237$. The original specific heat data is converted to the entropy domain using Eq. 2.2 to provide a monotonic function. Then the internal isofield entropy curves are found by interpolating along the isentropes in the s-T diagram. This is performed for both heating and cooling protocols. The resultant entropy curves are differentiated to find the specific heat curves due to internal field and temperature.

Fig. 2.3 displays an example s-T diagram of a given FOM comparing applied and internal magnetic field values.

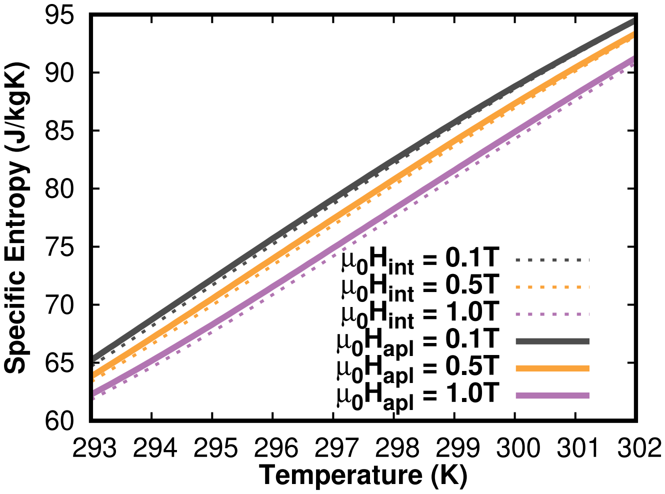

Figure 2.3: Example of constructed s-T diagram for a Si-alloy. The dashed lines are entropy data at constant internal field, H_{int}, while the solid lines are entropy data at constant applied field, H_{apl}.

The last demagnetizing field correction is on the ΔT_{ad} data. In a direct ΔT_{ad} device the sample is cycled between a low applied field, $\mu_0 H_{apl,low} = 0$ T, to a high applied field, $\mu_0 H_{apl,high} = 1.1$ T. The temperature is swept in both heating and cooling direction at 0.5 K/min. No field is applied at the low field position, so no correction is needed. However, for the high applied field state the high internal field $\mu_0 H_{int,high}$ is computed, using Eq. 2.9, with a demagnetization factor $\mathcal{N} = 0.374$ and the field corrected magnetization data. This $\mu_0 H_{int,high}$ represents the highest internal field possible for a specific sample within the direct ΔT_{ad} device. As can be seen in Fig. 2.4, due to temperature dependence and thermal hysteresis of the sample magnetization, the resulting $\mu_0 H_{int,high}$ (T) varies with temperature and according to the heating and cooling protocols.

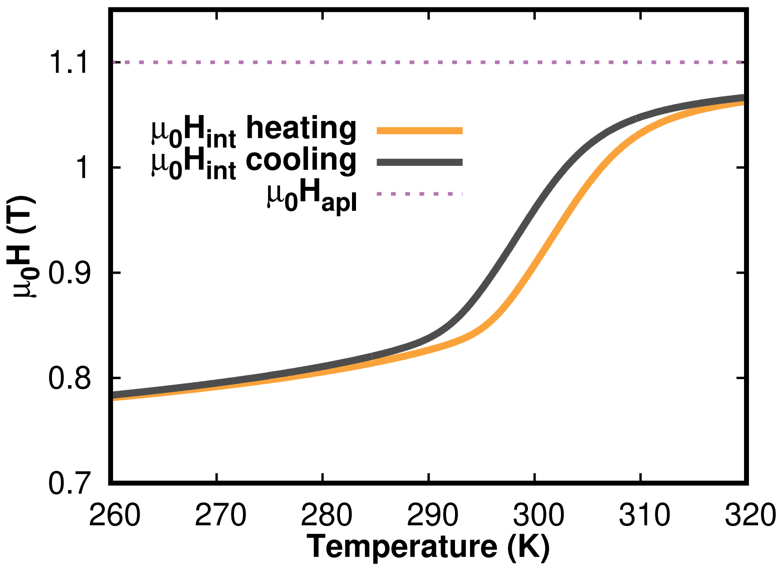

Figure 2.4: The high internal field value within the ΔT_{ad} measurement device are history and temperature dependent.

While the measured ΔT_{ad} data are for a constant applied field, the resulting corrected data have varying internal fields. This varying internal field is used with the corrected s-T curves to find the post-calculated ΔT_{ad}. The entropy curves are interpolated along isentropes for each $(T, H_{int,low} \rightarrow H_{int,high})$ pair corresponding to the ΔT_{ad} measurements where T is the zero-field temperature.

2.4 Results

Table 2.2 lists the six different Mn-Fe-P-Si alloys analyzed. The measured heating and cooling transition temperature is given based on the peaks of the zero field specific heat measurements, and the ΔT_{ad} peak is the maximum value obtained from the direct ΔT_{ad} measurements. A suggestion of the sample phase purity is made by the specific heat peaks. Fig. 2.5 shows the specific heat data corrected for the demagnetization field.

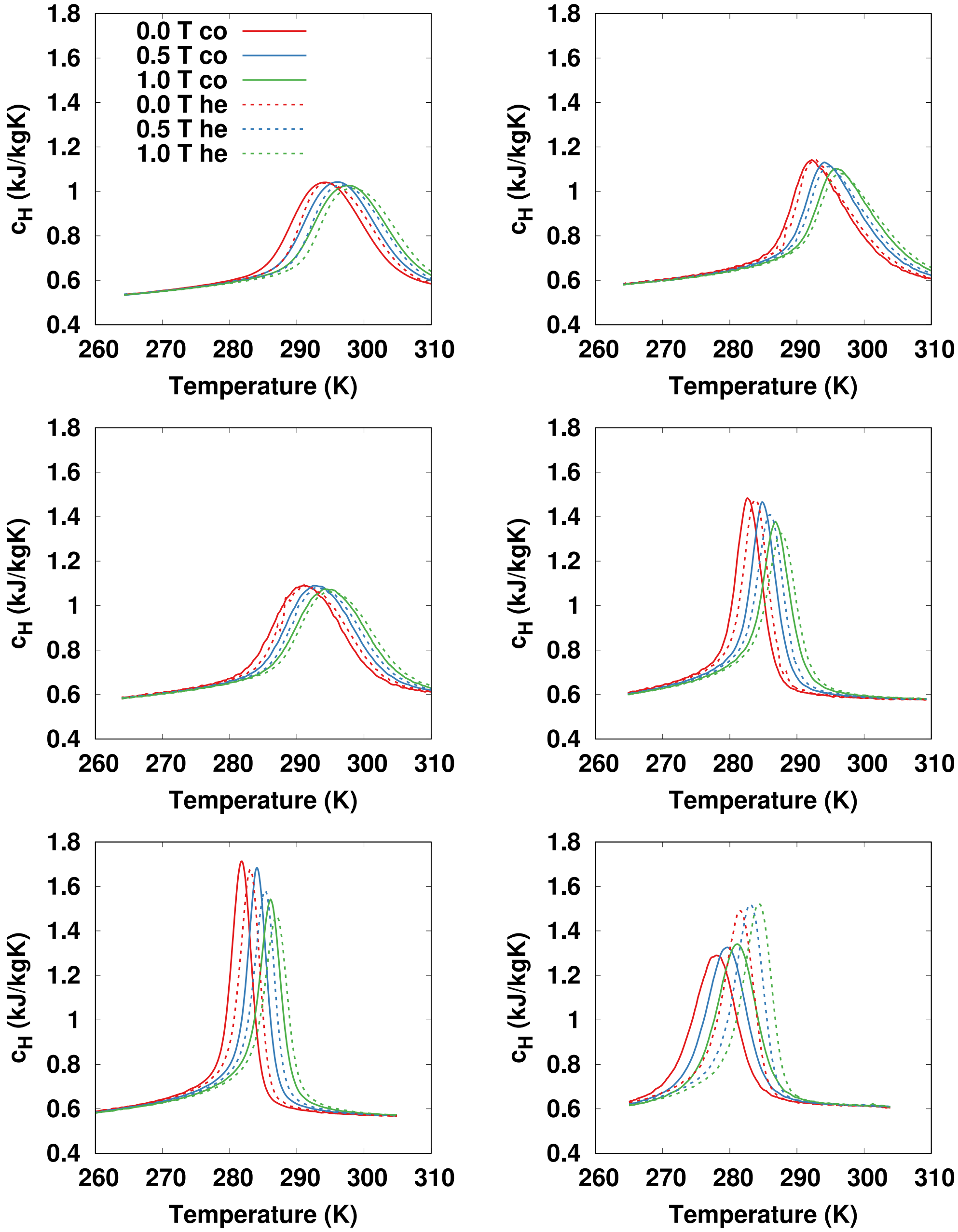

Figure 2.5: Specific heat data of all the samples for 0 T and 1 T field due to heating (he) or cooling (co) protocol. The in-field data is corrected for the demagnetizing field.

Table 2.2: Material properties of the Si-alloys studied. Transition temperature (T_{tr}) for the heating (he) and cooling (co) is based on the zero field specific heat peak. The peak ΔT_{ad} is taken from the directly measured data. The c_H peak data is from the zero-field and corrected 1 T specific heat data.

name	T_{tr} (K)		ΔT_{ad} Peak (K)		c_H Peak 0 T (J/kgK)		c_H Peak 1 T (J/kgK)	
	he	co	he	co	he	co	he	co
M1	294.7	294.5	1.2	1.1	1040	1040	1010	1030
M2	292.6	292	1.3	1.3	1140	1140	1080	1100
M3	290.7	290.7	1.2	1.2	1100	1090	1060	1080
M4	283.6	282.4	1.8	1.8	1480	1480	1330	1380
M5	282.9	281.5	1.9	1.9	1680	1720	1470	1550
M6	281.3	277.8	0.6	0.6	1490	1290	1520	1340

The results of post-calculated ΔT_{ad} and measured ΔT_{ad} for all Si-alloys are shown in Fig. 2.6. The post-calculated ΔT_{ad} are according to the four thermal paths defined in Fig. 2.1 HH, CC, HC, and CH. The reconstruction temperature range is limited by the capacity of the various devices; thus, the reconstructed data is limited between 260K and 310K.

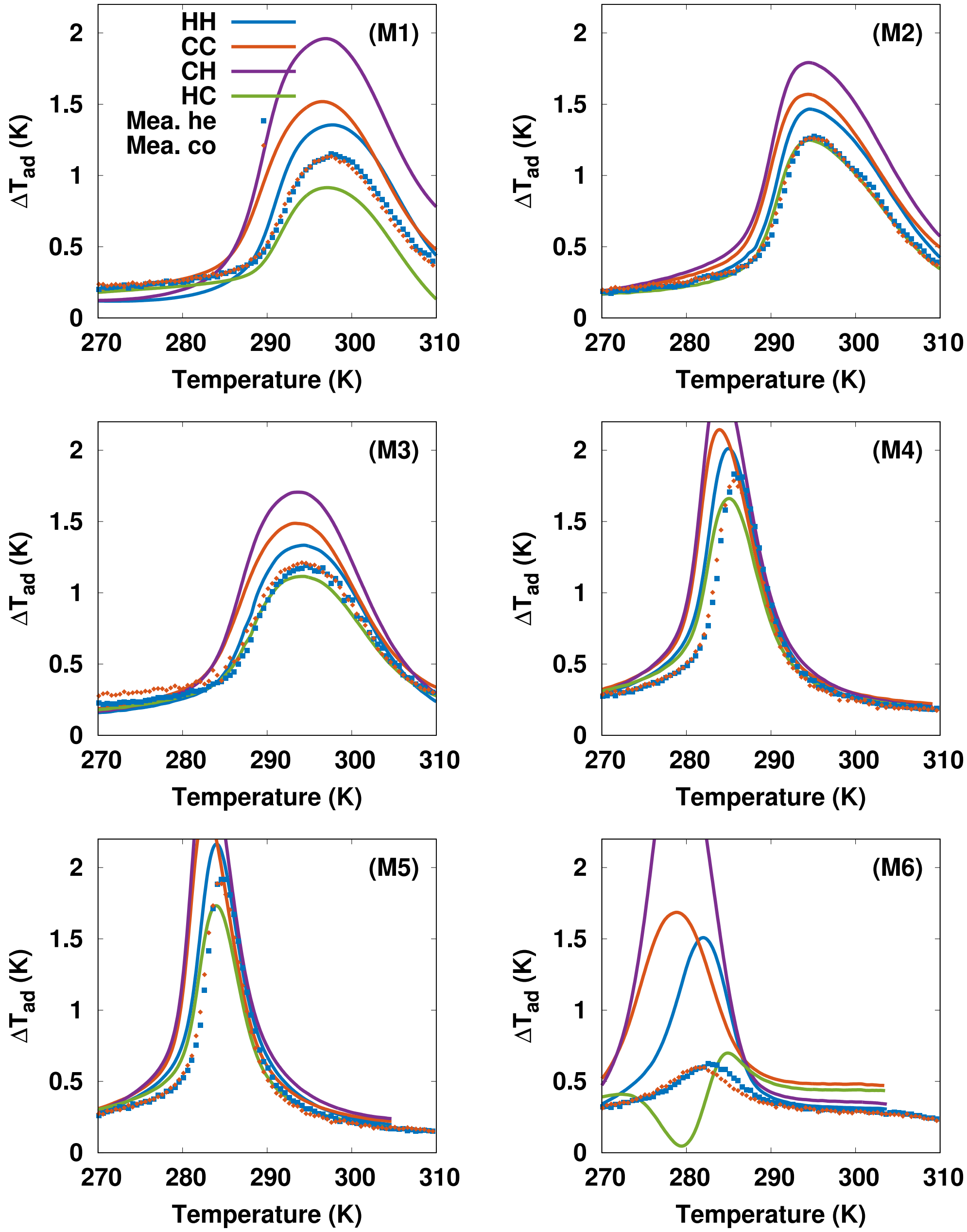

Figure 2.6: Comparison between the post-calculated ΔT_{ad} and measured ΔT_{ad} as a function of the temperature for the six Si-alloys.

The results for M2 and M3 showed similar trends to those found by Engelbrecht et al. [53], where the calculated ΔT_{ad} using low field heating and high field cooling entropy curves (HC) closely match the measured ΔT_{ad}. For M1, the direct ΔT_{ad}

measured values lie between the HC and HH thermal path. In M2 and M3 the peak values match well with the HC thermal path. For M4 and M5, the measured peak value is offset to the right, toward higher temperatures. As a result, for temperatures less than the peak location, the adiabatic temperature change predicted by the HC thermal path over-predicts the measured values. The M6 material has the largest hysteresis of all the samples tested and a small adiabatic temperature change is found in the measured data. Unlike the other samples, the post-calculated thermal path does not overlap the measured ΔT_{ad} values due to the higher hysteresis of this sample.

For all Si-alloys samples measured, there is little difference between the heating and cooling curves of the directly measured ΔT_{ad}. It can be inferred that the ΔT_{ad} measured is fully reversible under cyclic ΔT_{ad} conditions.

To show the impact of correcting for the demagnetizing field, the variation between corrected and non-corrected data is plotted in Fig. 2.7. The variation plot shows the impact of demagnetizing field correction on the post-calculated curves. By correcting for demagnetizing field the variation in the post-calculated curves is up to 0.2 K in the region of interest. The variation between corrected and non-corrected in the M2-5 samples is proportional to the measured adiabatic temperature change.

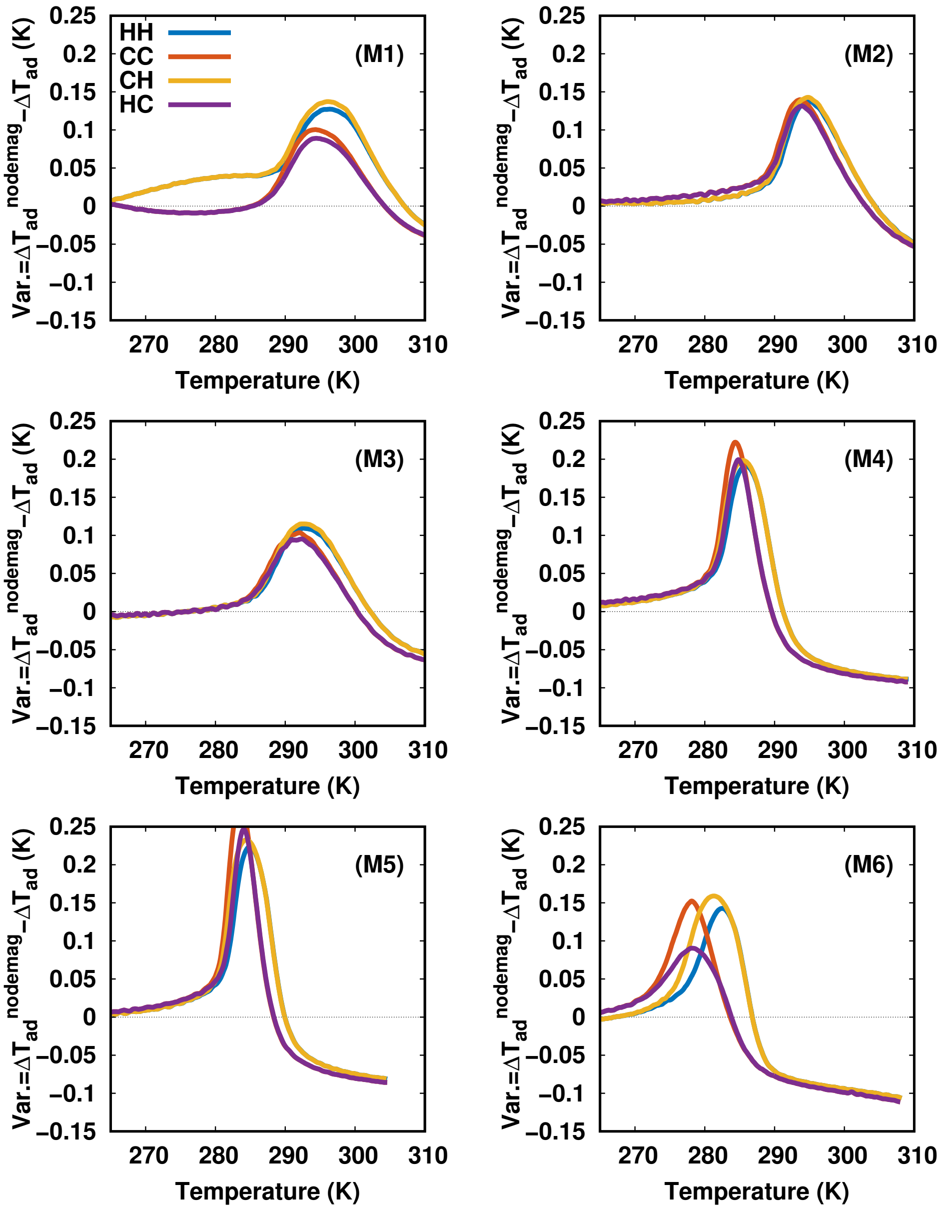

Figure 2.7: Variation (Var.) between corrected (ΔT_{ad}) and non-corrected post-calculated $\Delta T_{ad}^{nodemag}$.

2.5 Discussion

Guillou et al.[59] argue that when the thermal hysteresis becomes as large as the field induced shift on the transition temperature (dT_{tr}/dB), a strong decrease in the reversible temperature change occurs. In the present work, thermal hysteresis is defined as the difference in the temperature of the peak specific heat between heating and cooling measurements. The field induced shift on the transition temperature is the difference in temperature of the peak specific heat between H_{low} and H_{high}, in units of (K/T).

Table 2.3: Hysteresis, field shift based on heating (he) and cooling (co), internal field of max measured ΔT_{ad} and hysteresis to field shift ratio of all alloys studied and the sample studied by Engelbrecht et al. [50] are presented.

Alloy	Hysteresis (K)	Field shift (K/T)		Hysteresis/field shift (T)	
	$\mu_0 H = 0$ T	he	co	he	co
M1	0.2	3.2	3	0.06	0.07
M2	0.6	3.6	3.5	0.17	0.17
M3	0	3.9	3.1	0.00	0.00
M4	1.2	3.7	4.1	0.32	0.29
M5	1.4	3.8	4.3	0.37	0.33
M6	3.5	3.1	2.8	1.13	1.25
As-Alloy[53]	3	-	6	-	0.5

Table 2.3 lists the field-induced shift in transition temperature and hysteresis for the Si-alloys studied here. Data for the sample described by Engelbrecht et al. [53] is also included. When the ratio of hysteresis to transition shift is less than one, based on the arguments of Guillou et al. [59], a nearly reversible ΔT_{ad} should exist. For values larger than one, this reversibility disappears. In the M6 sample a ratio larger than one is found, corresponding to a small reversible ΔT_{ad}.

The sensitivity of the material data to the curves and the effect described by Guillou et al.[59] can also be understood by studying the s-T diagram.

The study of the s-T diagram, constructed from specific heat and magnetization data, is performed using a simplified model. The simplified model of the s-T diagram is based on the concept of a hypothetical FOM. This FOM has a baseline specific heat and goes through an order-disorder transition which leads to an entropy equation, Eq. 2.10. The equation has three parts,

$$s_{syn} = s_{M,off} + 3R(\ln(T) - \ln(270)) + \frac{b}{1 + \exp(k \cdot (T - T_{\mathrm{i},tr} - T_{fs} \pm \frac{1}{2}T_{hyst}))} \tag{2.10}$$

where the first part is the entropy offset due to the magnetic field component; this is set by the $s_{M,off}$ constant. The second part is the result of Eq. 2.2, assuming a c_H baseline equal to the 3R constant of $\mathrm{Mn_{1.25}Fe_{0.7}(Si_{0.5}P_{0.5})}$, and integrating from 270K to temperature T. The third part is a sigmoid function (S-curve), which represents the order-disorder transition. The strength of the order-disorder transition is represented by the slope of the S-curve; this is set by the k and b constants. Each FOM has a transition temperature, a field shift temperature with field and a hysteresis component. The initial transition temperature at zero field with no hysteresis of the FOM is determined by the $T_{\mathrm{i},tr}$ constant. For in-field entropy curves a temperature field shift, T_{fs}, is added to the initial transition temperature. Heating and cooling protocols introduce hysteresis which is represented by a temperature offset, T_{hyst}. Changing the constants allows for the creation of the zero field heating and cooling entropy curves, and the in-field heating and cooling entropy curves.

The specific heat is obtained by differentiating the s-T diagram, and the ΔT_{ad} thermal paths are post-calculated from the isentropes described in Section 2.3.1. Though this is not meant to be an accurate representation of the FOM s-T diagram, it does allow us to examine the sensitivities of material data on the post-calculated ΔT_{ad} curves. An interactive app has been constructed to allow for the reader to play with the material data and how it impacts the adiabatic temperature curves [1]. The original source code for this app is open source and can be found in the Github repository[2]. Fig. 2.8 shows a screen shot of the app. Using the sliders below the plots several

---

[1] `https://mybinder.org/v2/gh/TheoChristiaanse/TadFromS/master?filepath=Sliders%20Hyst%20App.ipynb`

[2] `https://github.com/TheoChristiaanse/TadFromS`

key properties can be changed. Using Thyst the hysteresis between the heating and cooling curves can be altered, k0T and k1T change the steepness of the low field and high field position respectively, Tshift shifts the temperature difference between the high and low field curves and Moff is the magnetic entropy offset between the high and low field curves.

Using Eq. 2.2, four different cases are described that can occur in material data measurements.

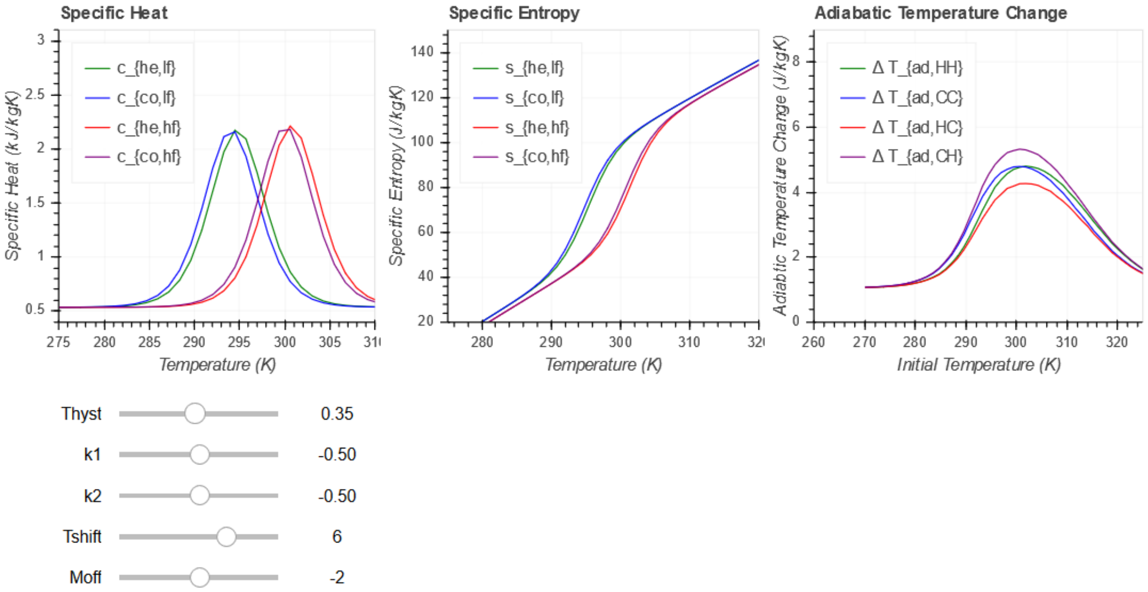

Thyst 0.35
k1 -0.50
k2 -0.50
Tshift 6
Moff -2

Figure 2.8: Screen-shot of the interactive app in which hysteresis can be shifted.

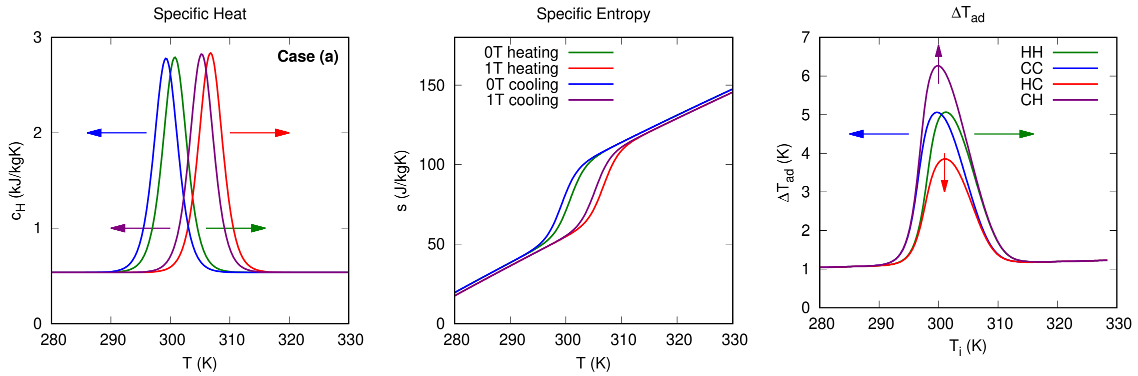

Figure 2.9: Case (a) showing the impact of increasing hysteresis.

In Fig. 2.9 the first case (a) shows the impact of hysteresis. Here the initial transition temperature and field shift temperature are fixed. The arrows indicate the direction the curves move when hysteresis (T_{hyst}) is increased, while the field-induced transition shift remains constant. For the specific heat as hysteresis increases, the cooling in-field and heating zero field move closer together and the heating in-field and cooling zero field move further apart. As a result, the post-calculated ΔT_{ad} shows a decreasing HC thermal path, increasing the CH thermal path and moves the HH/CC thermal paths apart.

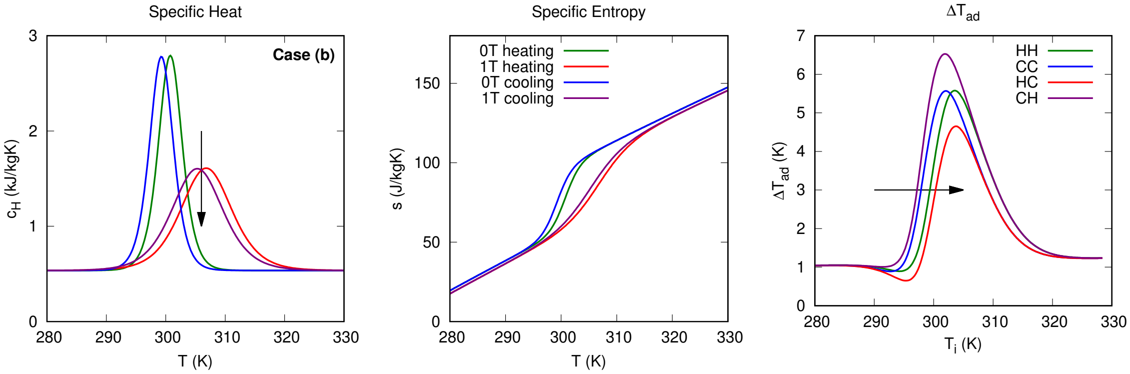

Figure 2.10: Case (b) the impact of decreasing specific heat peak.

In Fig. 2.10 the second case (b) shows the impact when the in-field specific heat peak is lowered and more broad. To achieve this, the in-field entropy curves $k2$ constant decreases to half of its original value. A reduced slope in the S-curve at the in-field transition is found. As a result, the peak of the HC thermal path shifts to the right, higher temperatures, and the CH shifts to the left, lower temperatures. Where the peak of the HC and the CH thermal paths are aligned with each other before, the CH peak aligns now with the CC peak and the HC peak aligns with the HH peak.

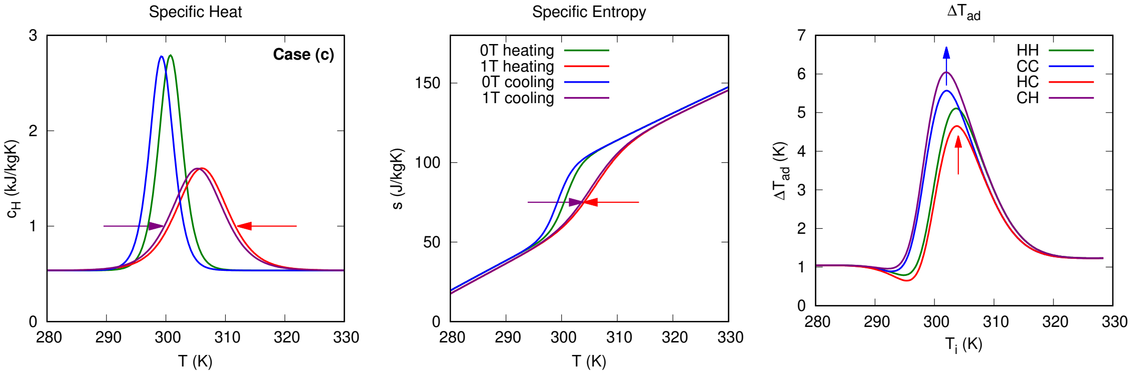

Figure 2.11: Case (c) the impact of decreasing hysteresis at high field values.

In Fig. 2.11 the third case (c) expands on (b) with a lower hysteresis in-field. The in-field hysteresis is gradually reduced to zero by lowering the T_{hyst} value. As the in-field hysteresis is lowered, the heating and cooling entropy curves at the in-field position move closer together. This moves the HC up toward the HH thermal path, and the CC up toward the CH thermal path. Ultimately, the HC and HH thermal paths will converge and the CC thermal path will converge with the CH thermal path into one.

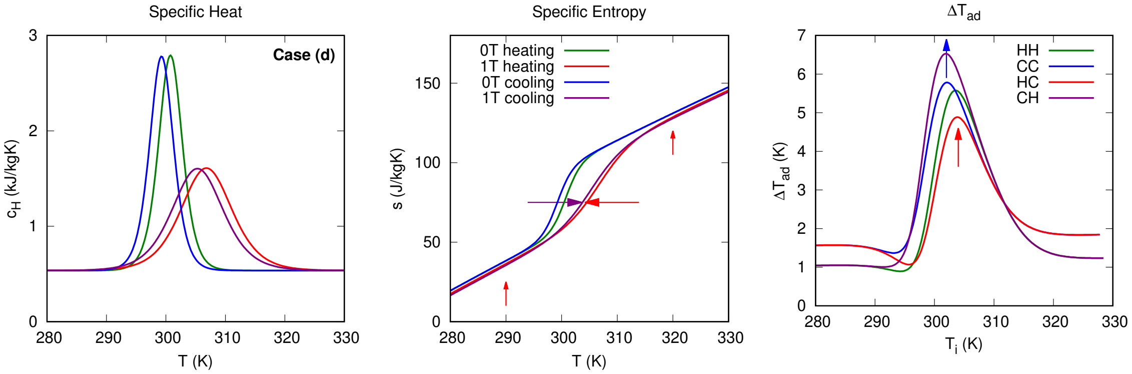

Figure 2.12: Case (d) variable magnetic entropy correction at the infield position.

Fig. 2.12 the last case (d) mimics the effect of lowering hysteresis with increasing field (c). Due to incomplete cycling the fully ferromagnetic phase is not reached at the reference temperature. A smaller magnetization derived entropy correction on the in-field heating curve than on the in-field cooling curve is found. A variation is not seen in the specific heat data but in the s-T diagram and post-calculated ΔT_{ad}. As the magnetization derive entropy correction is smaller, the in-field heating entropy curve is shifted upward. Thus, around the transition temperature the in-field entropy curves are squeezed into each other, lowering the hysteresis on the s-T diagram. The distinction between case (c) and case (d) is seen beyond the transition point on either side of the post-calculated ΔT_{ad}. For previous cases, all post-calculated ΔT_{ad} align from starting to ending temperature, but case (d) results in an offset between the baseline of the post-calculated ΔT_{ad} far away from the transition point.

Among the six samples studied here two Si-alloys (M2 and M3) show that the HC thermal path is the best match with directly measured ΔT_{ad}. Guillou et al. [59] observe that by maintaining field shift and increasing hysteresis the reversible component is reduced. This is corresponds to case (a); however, only the HC thermal path reduces, therefore represents closely [59] observation on the experimentally determined reversible ΔT_{ad} of the sample.

Field shift and hysteresis can explain large variations in ΔT_{ad} peaks measured. The M1-2-3-4-5 samples show a significant variation in ΔT_{ad} peaks compared to M6 material. Smaller variations between the samples can be understood by discerning heating from cooling shift. For example, we see that the field shift due to heating is similar across the M3-4-5 materials but the hysteresis is smaller in the M3 sample compared to the M4-5 samples. In Tab. 2.3 we observe for some samples a variation between the heating and cooling field shift of one degree. If the heating peak shifts over a less than the cooling peak, the HC thermal path, between heating 0T and cooling 1T, is shortened, resulting in a lower adiabatic temperature change.

With previously described sensitivities, we analyse the produced post-calculated ΔT_{ad} to find the cause of misalignment directly measured and post-calculated ΔT_{ad}. All materials have some hysteresis and therefore have four distinct post-calculated ΔT_{ad} thermal paths (a). Similarly, all samples show a smoother transition in the in-field position (b). Samples M4 and M5 show a close match with the HC thermal path but peak values are slightly offset to higher temperatures. The misalignment of the post-calculated ΔT_{ad} peaks in M4 and M5 could be due to two factors. First, the overall hysteresis of the sample might be over-predicted (a). Second, a specific heat peak in zero field is higher than measured, leading to shift of the post-calculated ΔT_{ad} to lower temperatures (b).

A possible reason for the misalignment of the For M1 material is a incomplete measurement cycle. If the measurement cycle does not reach the fully ferromagnetic or paramagnetic state at the end of its cycle, the material will move along a meta state between the heating or cooling entropy path. The working temperature range of the devices and the offset found between specific heat and magnetization leads to this conclusion. The M1 material is at the hot end his working range. Considering that the transition temperatures of M1-2-3 are close to each other, the misalignment is observed from no mis-alignment in M3 to increasing in M1.

2.6 Conclusions

An in depth analysis of the s-T diagram construction is done on six Si-alloys. The entropy curves constructed from specific heat and magnetization which, leads to the post-calculated ΔT_{ad}. These are compared to directly measured ΔT_{ad}. The demagnetizing field correction is crucial to proper reconstruction of the post-calculated ΔT_{ad}. In the region of interest an maximum offset of 0.2K is found between corrected and non-corrected post-calculated ΔT_{ad}.

In the analysis a distinction is made between the observed measured values and HC modeled thermal path. The observed values the phase shift over hysteresis ratio are contributors to degree of measured adiabatic temperature change. In the model the behavior of the HC curve is connected to changing material properties and measurement method.

From the Si-alloys examined it is concluded that the post-calculated ΔT_{ad} HC thermal path, zero field heating and high field cooling, match best directly measured ΔT_{ad} in M2 and M3 samples. This agrees with the result found in the publication of

Engelbrecht et al.[53].

It was proposed by Guillou et al. [59] that phase shift over hysteresis is critical to the reversible ΔT_{ad} of the FOM. These observations agree with the Si-alloy samples shown in this work. An analysis of the construction method of the s-T diagram shows how increasing hysteresis while keeping field shift the same diminishes only the HC thermal path. None of the other cases discussed show a reduction in the post-calculated ΔT_{ad}. This leads to the conclusion that the HC thermal path is the reversible ΔT_{ad} in the analysis of Guillou et al. This is re-enforced by the work of Engelbrecht et al. [53] and Von Moos et al.[56] concluding that the reversible component of the ΔT_{ad} is given by the HC thermal path.

Furthermore, the simplified model is used to understand sensitivities of the source data to the post-calculated curves. This leads to four described cases that explain how measured data and s-T diagram construction shape the post-calculated ΔT_{ad}.

The measurement method and sensitivity of the instrumentation is critical for analyzing material properties. Sweeping rate and region of interest should be well-defined beforehand. Improvements for further work would be to expand the capabilities of the measurement devices to higher temperatures and lower temperature regions and remeasure M1 material to see if the working range was the limiting factor of the reconstruction method.

Chapter 3

Modeling

A redacted version of this Chapter has been accepted to the International Journal of Refrigeration as:

Incorporating Device and Experimental Loss Mechanisms in AMR Modelling

T.V. Christiaanse[1], P.V. Trevizoli[1,2], P. Govindappa[1], R. Teyber[1], A. Rowe[1]

[1]University of Victoria, Victoria, B.C. Canada
[2] Department of Mechanical Engineering. Ingá University Center (UNINGÁ),
Rod. PR-317, 6114 - Parque Industrial 200, Maringá, PR, 87035-510, Brazil.

This Chapter describes a 1D numerical model developed to analyze the loss mechanisms of the PM1. The model looks into the integration of casing losses and dead volume on several packed bed Gd configurations.

3.1 Abstract

Active magnetic regenerators need magnetocaloric materials of sufficient size, shape, and quantity to create a matrix for characterization in a test apparatus. Limited availability of some novel magnetocaloric materials in a suitable form leads to regenerator beds which are smaller than desired and, when implemented in a test apparatus, result in unwanted loss mechanisms such as void spaces between the regenerator and heat exchangers. Because the potential cooling power is reduced with dead volume losses and thermal interactions with the ambient environment, an investigation of the effects of void volumes and ambient interactions when using small regenerators is done with experimental and 1D numerical methods. Experimental results from packed beds with varying size composed of gadolinium spheres are used to validate a system model. In the 1D model, additional nodes are included to incorporate dead volume sections and ambient interactions are treated as an energy term in fluid governing energy equation. These interactions are a function of the regenerator fluid temperature and the boundary condition temperature assumed at the outer casing of the regenerator. Due to uncertainty regarding the casing thermal state, a range of cases are numerically tested including: a fixed temperature and a linear temperature profile from hot to cold end using the simulation boundary conditions. The modeling predictions disagree with the experimental results when dead volume sections are not included. The casing heat leaks shift predicted temperature span for net cooling power up to 2.5 W; however, they do not vary the predicted temperature span for higher net cooling power.

3.2 Introduction

Magnetocaloric materials are possible working substances for refrigeration and heat pumping; they are typically used in an active magnetic regenerator (AMR) cycle. Novel first order materials are proposed as good, lower-cost alternatives to rare earth alloys but are not widely available in large quantities for experimentation [61]. Furthermore, material availability is compounded by the fact that laboratory testing in a regenerator requires specific geometries suitable for creating effective thermal matrices [31, 14]. Useful geometries can be difficult to manufacture with some material systems. A test apparatus may be developed with a material like gadolinium as a readily available baseline material, but, when used with a small amount of material, only a portion of the design volume available in the device may be utilized. For example, for a fixed diameter, small amounts of novel material lead to shorter regenerator beds in the PM1 device [60]. This can increase experimental loss mechanisms in the form of larger void volumes between the regenerator and heat exchanger than desired.

To clearly distinguish the impact of material and device on measured AMR performance requires an understanding of the impact of device-specific loss mechanisms. This is an important problem when material availability leads to testing of regenerators that are smaller than the nominal design for a device. We experimentally and numerically investigate the impact of device losses on short regenerator beds by using a well known magnetocaloric material Gadolinium (Gd) [17]. The terms *short* and *small* are used here to describe a regenerator which is a fraction of the nominal design length in a particular device.

Trevizoli and Barbosa describe several device-specific loss mechanisms for AMR systems. Some of the common loss mechanisms are related to magnetic field demagnetization, void volumes, and unwanted heat interaction between ambient and fluid - called casing losses. Some of these losses have been quantified based on their individual contribution to temperature span and cooling power. Dead volume ratio is used to describe the size of void space compared to the regenerator interstitial fluid. One definition for dead volume ratio is the void volume on a single side of a regenerator relative to the volume occupied by the fluid in the regenerator [72].

A previous study found the contribution of void volumes to be small when dead volume ratio is small [44]. Jacobs uses a 1D model to show that when experimental settings are optimised for a fixed temperature span, cooling power remains similar for dead volume ratios up to 0.06 [44]. Jacobs also showed for larger dead volume ratios a reduction of up to 50% in cooling power can be found. Since the dead volume ratio is increased when a short regenerator is used, it is important to include this loss mechanism in system models.

The loss in cooling power and temperature span with increasing dead volume is due to an imperfect thermal link between AMR and HEX. Park et al. provide experimental data and modeling results quantifying this imperfect thermal link between the hot side of the regenerator and the hot heat exchanger [73]. Many studies consider the void volume to be of equal size on either side of the regenerator, but Park et al. [73] examine configurations where the dead volume on the hot and cold side are not equal. The fluid temperature along the regenerator assembly at each point in the cycle for different hot side void volume sizes and displaced volumes are presented. When a large displaced volume is used, the thermal link between regenerator and hot HEX is strong, e.g. a small temperature difference is found between AMR and hot HEX after the hot blow. However, when using a smaller displaced volume with the same dead volume, the thermal link is weak and a steep thermal gradient between the end of the AMR and the hot HEX is found after the hot blow.

Three studies look at the effectiveness of passive regenerators effected by dead volume [72, 74, 75]. Liu and Trevizoli and Barbosa use experimental and numerical results to study various passive regenerators [72, 74]. Numerous dead volume ratios and utilisations are compared and good agreement is found between experiments and modeling outcomes. This passive modeling work gives high confidence in the thermal-hydraulic closure relationships that are used for 1D modeling. In a recent publication Trevizoli et al. expand on earlier work by experimentally investigating the maldistribution of the inlet fluid flow with decreasing the void space [75]. A range of diffusers with decreasing void space are tested on different regenerator lengths. Two aspects are noted, as the length of the regenerator decreases with fixed void space, the effectiveness of the regenerator decreases, and as void space is reduced for any length of the regenerator the effectiveness also decreases. With decreasing diffuser size the maldistribution of the inlet flow at the entrance of the regenerator increases. The smaller diffusers cause recirculating flow at the ends of the regenerator making these regions ineffective. This work shows that there are trade-offs between flow distribution at the inlet and dead volume.

The numerical models used in these studies are 1D representations of the regenerator [76, 47] where thermal non-equilibrium between solid and fluid domains is assumed. Additional fluid and solid computational nodes are added to either side of the AMR to represent the dead volume sections. The governing equations are modified to match the physics of the geometry of the flow channel and its content. In the study performed by Jacobs the dead volume is modelled by extending the AMR with additional passive stainless-steel sphere spheres [44], while Park et al., Liu, Trevizoli and Barbosa, Trevizoli et al. model the void space as an empty tube attached to the AMR.

Trevizoli et al. included unwanted interactions from the ambient to the fluid, called casing losses [32]. These casing losses are included on the AMR domain but are neglected in the added void space. The casing losses can be neglected when sufficient insulation is in place around the AMR or void space. Ambient interactions are considered in the radial direction of the AMR and are added as an energy term to the fluid governing equation [32]. This energy term is a function of the outer housing boundary condition temperature and the fluid temperature. The outer housing boundary condition is determined using a 2D conduction model of the AMR system.

Nielsen et al. expand a previously developed 2D model adding additional unwanted heat interactions producing a so called 2.5D model [77]. The unwanted heat interaction are included using a energy loss term on both fluid and solid governing equations. The energy loss term is a function of local temperature, casing temperature and a global heat transfer coefficient. The thermal resistance is determined for each node from the casing to the local node. These losses improve the simulation outcomes as they produce results closer to experimental results.

We use experimental and numerical methods to investigate the impact of small regenerators in the PM1 [60]. Established numerical AMR methods are used in a numerical model written in python [32, 72, 47, 76]. The code has been made publicly available [1]. To validate the modeling approaches experiments are performed with regenerators of varying length in the PM1.

3.3 Experimental Methods

Four experimental regenerator configurations are prepared for the PM1 device. An experiment using a long regenerator (55 g) and three short (23 g) regenerators placed at different locations with respect to the PM1 magnetic field source. Fig. 3.1 depicts a sketch of each prepared regenerator assembly. The configuration of each regenerator assembly consists of connectors (void space), packed glass spheres (GS) and packed Gd spheres as AMR (AMR). The width of the nested Halbach arrays and its placement along the z-dimension is depicted by the light grey region. The four configurations capture a number of effects: (1) size and location of dead volume; (2) changing contact area and heat leak through the casing in void spaces; and (3) varying magnetic field distribution and waveform.

The short regenerators use the same mass and Gd material to construct the packed beds. By varying the location, the short cold side regenerator has the smallest cold side dead volume and the largest hot side dead volume. The short hot side regenerator has the largest cold side dead volume and the smallest hot side dead volume. The centre bed's void space on the hot side and cold side is of similar volume. The magnetic field drop at the ends of the Halbach, therefore the highest field variation is with the centre beds. The average field for the hot and cold side beds is lower but similar to each other. The field distribution along the regenerator; however, for both regenerators differ since the field drops of in opposite directions.

---

[1] Python AMR model: `https://github.com/TheoChristiaanse/AMRmodel`

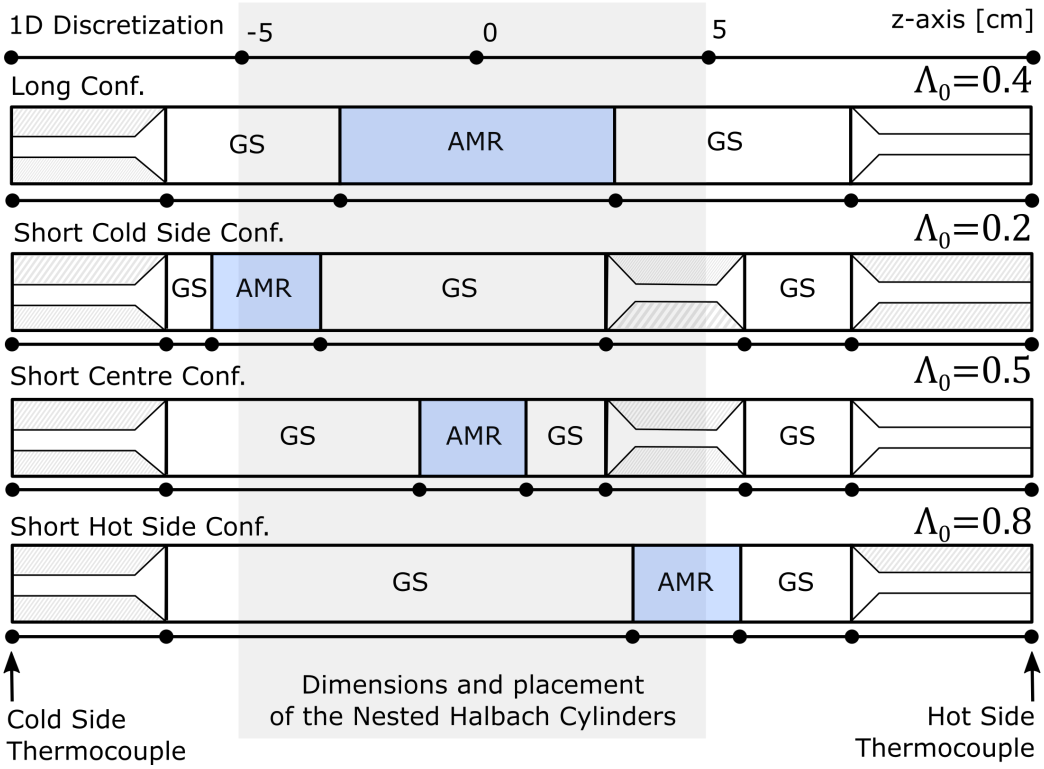

Figure 3.1: The various prepared experimental configurations tested in the PM1. Gd spheres (AMR) are packed, between glass spheres (GS). The other parts of the housing are connectors. The hatching indicates where the structural material of the connector is. These connectors are considered as void spaces of the assembly.

Each regenerator consists of Gd spheres held in place by stainless steel meshes. The mesh is fixed in place by glass spheres filling the void spaces between regnerator and connectors. Gd material is an established magnetocaloric material for room temperature magnetic refrigeration [17, 9]. The glass spheres serve two functions; (i) they reduce the dead volume in between the regenerators and (ii) they aid in fixing Gd regenerator's position. Furthermore, they also act as passive regenerators. The long and short-hot side configurations are constructed using two end connectors and glass spheres on either side of the regenerator. The cold and centre configurations are assembled using two G10 tubes and, therefore, have an additional intermediate connector.

In Tab. 3.1 the regenerator properties and operating parameters used in the experiments are listed. Eight experiments are performed at different net applied cooling loads, Q_{net}. The performance of each regenerator is evaluated for rejection temperatures between 26 °C and 18 °C. The displaced volume, V_d, in the long configuration is fixed at 4 cm^3 and, for the short beds, 2 cm^3. The frequency in all experiments is set to 1 Hz. Initially, the large regenerator is tested which is less prone to losses due to a relatively larger cooling power. This is followed by the three shorter configurations.

Table 3.1: Regenerator properties and operating parameters of the configurations.

	m (g)	L_r (mm)	D_{sp} (μm)	V_d (cm^3)	f (Hz)	Q_{net} (W)
long	55	55	450-550	4	1	0, 10
short	23	23	250-300	2	1	0, 2.5
Glass Spheres	-	-	3125	-	-	-

Since the dead volume is not of equal size on either side of the regenerator a term is introduced to easily identify each experimental configuration. The dead volume fraction, Λ_0, is defined in terms of the cold-side void space relative to the total voids space. Dead volume fraction is calculated using the following equation

$$\Lambda_0 = V_{o,cold}/V_o \tag{3.1}$$

with

$$V_o = V_{o,cold} + V_{o,hot} \tag{3.2}$$

where $V_{o,cold}$ is the total void space between the cold side regenerator face and the cold thermocouple. $V_{o,hot}$ is the total void space between the hot side regenerator face and the hot thermocouple. Therefore, V_o is the total dead volume in the regenerator assembly. The dead volume fraction for each configuration is shown in Fig. 3.1.

Tab. 3.2 lists the dead volume for each of the prepared configurations. In addition the volume of the regenerator, V_r, and the interstitial regenerator fluid, $V_{f,r}$, the dead volume fraction and ratio are also listed. Lastly, the ratio of the cold side dead volume and the displaced volume is given.

Table 3.2: Dead volume details for all the experiments performed.

	V_d	$V_{o,cold}$	$V_{f,r}$	V_r	$V_{o,hot}$	V_o	Λ_0	$V_{o,cold}/V_{f,r}$	$V_{o,cold}/V_d$
			(cm^3)					(-)	
long	4.0	3.3	4.0	7.1	5.2	8.5	0.4	0.8	0.8
cold	2.0	1.4	1.6	2.9	8.3	9.8	0.2	0.9	0.7
cen	2.0	4.9	1.6	2.9	4.8	9.8	0.5	3.1	2.5
hot	2.0	8.5	1.6	2.9	2.5	11.0	0.8	5.3	4.3

3.4 Modeling Methods

The system model is based on a 1D approximation of the structure and components shown in Fig. 3.1. The 1D z-axis is considered through the centre of the housing. Both the glass and the Gd spheres are treated as a regenerator in which fluid and solid governing equations are solved. In the void volumes, only the fluid domain is solved which is discussed later.

The governing equations for the regenerator section are based on an assummed thermal non-equilibrium between fluid and solid domains [78]. The governing equation for the fluid domain is given by Eq. 3.3

$$\rho_f c_f A_{rh} \epsilon \frac{\partial T_f}{\partial t} + \frac{\partial}{\partial z}\left(\dot{m} c_f T_f\right) - \frac{\partial}{\partial z}\left(k_{\text{eff},f} A_{rh} \epsilon \frac{\partial T_f}{\partial z}\right) = \left|\frac{\dot{m}}{\rho_f}\frac{\partial p}{\partial z}\right| + Q'_{leak}(T_{casing}, T_f) + A_{rh}\beta h_{\text{eff}}(T_r - T_f) \quad (3.3)$$

where T_f is the fluid temperature and z, t are the spatial and time coordinates. ρ_f is the fluid density, $c_{p,f}$ is the fluid specific heat. Both fluid density and specific heat are a function of fluid temperature. A_{rh} is the cross section of the regenerator housing, ε is the regenerator porosity, $k_{\text{eff},f}$ is the effective conduction of the fluid, $\dot{m}$ is the mass flow rate as a function of time, $\frac{dp}{dz}$ is the fluid pressure drop along the z axis, Q'_{leak} is the energy term that describes the unwanted heat interaction between fluid and casing boundary condition per unit length, β is surface area per unit volume of the regenerator and h_e is the effective heat transfer coefficient between the solid and fluid domain. The governing equation for the solid domain is given by Eq. 3.4 [47, 78]

$$\rho_s c_s A_{rh} (1-\epsilon) \frac{\partial T_r}{\partial t} - \frac{\partial}{\partial z}\left(k_{\text{eff},r} A_{rh} (1-\epsilon) \frac{\partial T_r}{\partial z}\right) = Q'_{MCE} + A_{rh}\beta h_{\text{eff}} (T_f - T_r) \quad (3.4)$$

with

$$Q'_{MCE} = -\rho_s A_{rh} (1-\epsilon) T_r \left.\frac{\partial s}{\partial \mu_0 H_{int}}\right|_{T_r} \frac{\partial \mu_0 H_{int}}{\partial t} \quad (3.5)$$

where c_r is the solid specific heat, ρ_r is the solid density, T_r is the solid temperature, $k_{\text{eff},r}$ is the effective conduction of the regenerator solid, Q'_{MCE} is the magnetocaloric effect energy term per unit length, s is the entropy of the solid, μ_0 is the vacuum permeability and H_{int} is the internal field value. In the case of the glass spheres this magnetocaloric energy term is not included. The boundary conditions at the edges of the domain are listed in Tab. 3.3.

Table 3.3: Boundary conditions for fluid and solid domains.

domain		Cold Side	Hot Side
fluid	hot blow $u_d >= 0$	$T_f = T_{cold}$	$\frac{\partial T_f}{\partial z} = 0$
fluid	cold blow $u_d < 0$	$\frac{\partial T_f}{\partial z} = 0$	$T_f = T_{hot}$
solid		$\frac{\partial T_r}{\partial z} = 0$	$\frac{\partial T_r}{\partial z} = 0$

3.4.1 Closure Relationships

Eq. 3.6 gives the fluid mass flow rate produced by the PM1 piston

$$\dot{m} = \rho_f \cdot V_d \cdot \pi f sin(t 2\pi f) \quad (3.6)$$

where V_d is the displaced volume and f is the frequency of piston.

The Reynolds number, Re_{sp}, is calculated using the mass flow rate and sphere diameter of the regenerator particle:

$$\mathrm{Re}_{sp} = \frac{\dot{m} D_{sp}}{A_c \mu_f} \tag{3.7}$$

where D_{sp} is the particle diameter and μ_f is the temperature dependent dynamic viscosity of the fluid. Eq. 3.8 is the effective conductivity of the fluid [78]

$$k_{\mathrm{eff},f} = k_f + \rho_f c_{p,f} \frac{0.75 \alpha_f \mathrm{Pe}_p}{2} \tag{3.8}$$

with

$$\mathrm{Pe}_p = \mathrm{Pr} \cdot \mathrm{Re}_{sp} \tag{3.9}$$

where α_f is the thermal diffusity of the fluid and Pr is the Prandtl number of the fluid. For the solid the effective conductivity is given by Eq. 3.10

$$k_{\mathrm{eff},s} = k_f \left(\frac{(1-\alpha_0)\left(\epsilon f_0 + \frac{(-\epsilon f_0+1)k_r}{k_f}\right)}{\left(1-\epsilon\,(1-f_0) + \frac{k_r \epsilon (1-f_0)}{k_f}\right)} + \alpha_0 \frac{\left(2\frac{k_r^2(1-\epsilon)}{k_f^2} + \frac{(1+2\epsilon)k_r}{k_r}\right)}{\left(\frac{(2+\epsilon)k_r}{k_f} + 1 - \epsilon\right)} \right) \tag{3.10}$$

with

$$\alpha_0 = 10^{-1.084-6.778(\epsilon-0.298)} \tag{3.11}$$

and

$$f_0 = 0.8 + 0.1\epsilon \tag{3.12}$$

where k_r is the static conduction coefficient of the regenerator material. The energy exchange between solid and fluid is governed by the local temperature difference of solid and fluid, the area per volumetric unit, β, and the effective heat transfer coefficient, h_{eff}

$$h_{\mathrm{eff}} = \frac{\mathrm{Nu}_{sp} \cdot k_f}{D_{sp}} \cdot DF \tag{3.13}$$

with

$$\mathrm{Nu}_{sp} = 2 + 1.1\mathrm{Re}_{sp}^{0.6}\mathrm{Pr}^{1/3} \tag{3.14}$$

The Nusselt number, Nu_{sp}, for spheres is taken from [79]. The Hausen degradation factor, DF, to correct for the internal temperature gradient of the spheres [80]

$$DF = \frac{1}{1 + \frac{\mathrm{Bi}}{5}\phi_H} \tag{3.15}$$

with

$$\mathrm{Bi} = \frac{\mathrm{Nu}_{sp} k_f}{2k_r} \tag{3.16}$$

and

$$\phi_H = 1 - \frac{4}{35 \cdot \mathrm{Fo}} \tag{3.17}$$

with

$$\mathrm{Fo} = \frac{\alpha_s}{f\left(\frac{D_{sp}}{2}\right)^2} \tag{3.18}$$

where α_s is the thermal conductivity of the solid.

The pressure drop term is calculated using Ergun's relationship for spheres [81]

$$\frac{dp}{dz} = \frac{1.75{u_d}^2\left(1-\epsilon\right)\rho_f}{D_{sp}\epsilon^3} + \frac{150u_d\left(1-\epsilon\right)^2\mu_f}{{D_{sp}}^2\epsilon^3} \tag{3.19}$$

with

$$u_d = \frac{\dot{m}}{\rho_f A_{rh}} \tag{3.20}$$

The material properties for Gd are taken from REF. [17] and the glass sphere material properties are listed in Table 3.4.

Table 3.4: Relevant material data that is used for the simulation.

	Gd	Glass Spheres [82]
Density (kg/m^3)	7900 [83]	2230
Conduction (W/mK)	10.5 [83]	1.2
Specific Heat (J/kgK)	REF. [17]	800
Magnetisation (Am^2/kg)	REF. [17]	-
Entropy (J/K)	REF. [17]	-

3.4.2 Applied Field

The magnetic field source in the PM1 is created by two nested Halbach arrays. The inner Halbach array rotates with respect to the outer array, which results in varying applied field values along the centre axis of the Halbach arrays through the bore. Fig. 3.2 shows the field values along the bore as a function of inner magnet rotation. It is important to note that at the centre of the bore the highest field variation values are found. These drop off as we move away from the centre to the edges of the magnet. By placing the regenerator close to the edge of the high field region, the material is subjected to a lower applied field variation compared to the centre.

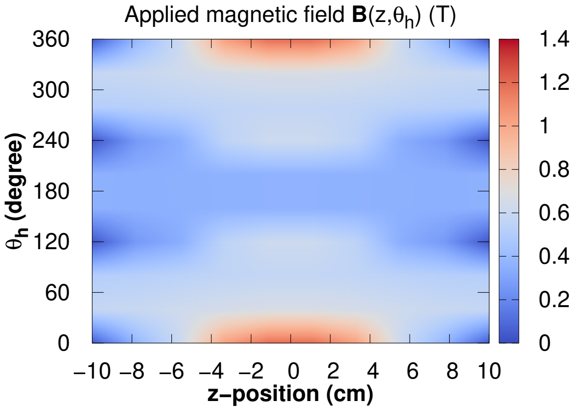

Figure 3.2: Interpolated values of the measured applied field of the PM1 Halbach arrays along the bore. Measurements are done at the center of the bore each 0.05cm and with increments of 30 degrees of rotation.

The MCE is determined based on the internal field value in the regenerator. The applied field values are corrected for the demagnetising field to find the internal field values. The demagnetising field is calculated using an average demagnetising coefficient given by Eq. 3.21 [52, 84]

$$\mathcal{N} = \mathcal{N}_{sp} + (1 - \epsilon)(\mathcal{N}_{sh} - \mathcal{N}_{sp}) \tag{3.21}$$

where $\mathcal{N}$ is the regenerator demagnetising coefficient, $\mathcal{N}_{sp} = 1/3$ is the demagnetising coefficient of a single sphere, ϵ is the porosity of the regenerator, and $\mathcal{N}_{sh}$ is the demagnetising coefficient due to the overall shape of the regenerator. $\mathcal{N}_{sh}$ is found using the look-up tables provided by [85]. In Tab. 3.5 the overall shape demagnetising coefficient and the regenerator demagnetising coefficient is given for short and long regenerators.

Table 3.5: Demagnetisation coefficient for the long and short regenerators.

	L (mm)	D_{rh} (mm)	ϵ	$\mathcal{N}_{sh}$	$\mathcal{N}$
long	55	16	0.36	0.447	0.406
short	23	16	0.36	0.387	0.368

The internal field in the simulation is approximated by reducing the applied field based on a reduction factor. In Eq. 3.22 the applied field for each position along the regenerator is modified with a location dependent reduction factor

$$H_{int}(z) = R_m(z) \cdot H_{apl}(z) \tag{3.22}$$

where H_{int} is the internal field in the regenerator, H_{apl} is the applied field, and R_m is the field reduction factor. The field reduction factor is calculated using a location based maximum internal and maximum applied field (see Eq. 3.23):

$$R_m(z) = \frac{H_{int,max}(z)}{H_{apl,max}(z)} \tag{3.23}$$

The maximum location based internal field, $H_{int,max}$, is calculated using Eq. 3.24

$$\mu_0 H_{int,max}(z) = \mu_0 H_{apl,max}(z) - \mu_0 \rho_r \mathcal{N} M\left(T_{cy,ave}, H_{apl,max}(z)\right) \tag{3.24}$$

where μ_0 is the vacuum permeability constant, $H_{apl,max}$ is the location based maximum applied field and M is the magnetisation of Gd at the maximum applied field value and the cycle average temperature. For each cycle, the temperature of the solid is averaged over the cycle at each location and used to determine average magnetization. This field reduction factor allows for a fast approximation of the internal field values that the regenerator experiences at each location.

3.4.3 Dead Volume Implementation

The dead volume is implemented by modeling both void space and passive regenerator (glass sphere) sections. For the glass sphere section both solid and fluid governing equations (as stated earlier Eq. 3.4 & Eq. 3.3) are solved neglecting the MCE energy term. The void space due to the connectors contain no glass spheres, hence only the fluid governing equation is solved and reduces to Eq. 3.25.

$$\langle \rho c \rangle_f A_c \epsilon \frac{\partial T_f}{\partial t} + \frac{\partial}{\partial z}\left(\dot{m} \langle c \rangle_f T_f\right) - \frac{\partial}{\partial z}\left(k_f A_c \epsilon \frac{\partial T_f}{\partial z}\right) = Q'_{leak}(T_{casing}, T_f) \tag{3.25}$$

Most of the pressure drop is due to the packed beds, therefore we neglect the pressure drop term in the void space.

3.4.4 Casing Losses

The unwanted heat interaction between the fluid and the casing are included in the model using the Q'_{leak} term. This term is added to the fluid governing energy equation of the regenerator - Eq. 3.3 - and the void space - Eq. 3.25. The heat leak is considered in the radial direction. In Eq. 3.26 the general form of the equation is given

$$Q'_{leak} = P_{rh}U(T_{casing} - T_f) \tag{3.26}$$

where P_{rh} is the perimeter based on the inner diameter of the regenerator housing wall, U is the global heat transfer coefficient, T_f is the temperature of the fluid, and T_{casing} is the temperature boundary condition of the outer housing components.

To simplify our simulation, we have replaced the 2D conduction model used by Trevizoli with an assumed casing temperature [52]. Two casing boundary conditions are tested; we will refer to these cases using the acronyms **(Tamb)** and **(grad)**. The first assumes a constant outer casing temperature along the total length while the second condition assumes a linear temperature variation.

(Tamb)

$$T_{casing} = T_{amb} \tag{3.27}$$

The temperature along the entire boundary is fixed to the ambient temperature of the lab taken from the experimental data.

(grad)

$$T_{casing}(z) = T_{cold} + \frac{z}{L_{housing}} \cdot (T_{hot} - T_{cold}) \tag{3.28}$$

A linear temperature gradient with the T_{cold} at the cold side and T_{hot} at the hot side is assumed. T_{cold} and T_{hot} are set based on the current simulation setting of fluid domain boundary conditions.

The **(grad)** case assumes the casing temperature is driven by the fluid domain boundary conditions T_{hot} and T_{cold}. The **(Tamb)** case looks at a scenario where the casing temperature is fully driven by the ambient temperature.

Fig. 3.3 shows a sketch of the composite system in the radial direction for the regenerator section and the void space section. The boundary condition of the casing temperature is set at the location where the outer casing components start. The outer components of the PM1 consist of the Halbach magnets together with flanges to fix the regenerator housing and Halbach magnets. The components between fluid domain and the outer casing boundary condition are considered a composite system, reducing all the components to a single global heat transfer coefficient, U.

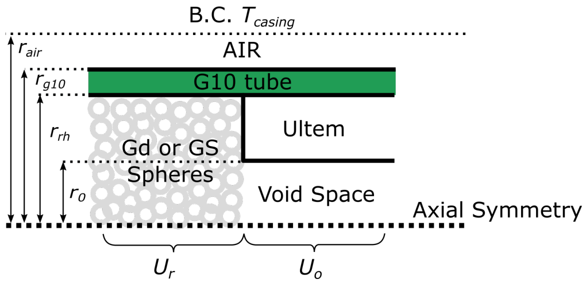

Figure 3.3: A sketch of the regenerator housing including outer system components up to the casing boundary condition.

The Gd and GS spheres represent the casing assumption for the packed glass Gd and glass spheres. Both the packed spheres and the connectors are fitted into the G10 tubing - outer radius $r_{g10} = 9.5$ mm and inner radius $r_{rh} = 8$ mm - followed by an air gap between the housing and outer casing components, $r_{air} = 11$ mm. The rotation of the inner Halbach magnet causes Couvette flow in the air gap [86, 87]. This causes the heat transfer through the air to be dominated by conduction. Therefore, the global heat transfer coefficient for the regenerator section is expressed as Eq. 3.29

$$U_r = \frac{1}{\frac{1}{h_r} + \frac{r_{rh}}{k_{g10}} \ln\left(\frac{r_{g10}}{r_{rh}}\right) + \frac{r_{rh}}{k_{air}} \ln\left(\frac{r_{air}}{r_{g10}}\right)} \tag{3.29}$$

where the thermal conductivity for G10 is 0.608 W/mK [88] and for Air 0.026 W/mK [89], and h_r is heat transfer coefficient between the packed beds and the inner housing diameter [79].

$$h_r = \frac{0.17 Re_{dp}^{0.79}}{D_{sp}} \tag{3.30}$$

The void space section represents the end and intermediate connectors. The void space's inner diameter is calculated using Eq. 3.31 based on a hollow cylinder approximation of the connector void space

$$r_o = \sqrt{\frac{V_o}{\pi L_o}} \tag{3.31}$$

where r_o is the inner radius, V_o is the void space due to the connector, and L_o the length of the connector. The perimeter is then simply calculated by $P_o = 2r_o\pi$.

For the void space section, the global heat transfer coefficient is given by Eq. 3.32.

$$U_o = \frac{1}{\frac{2r_o}{3.66k_f} + \frac{r_o}{k_{ultem}} \ln\left(\frac{r_{rh}}{r_o}\right) + \frac{r_o}{k_{g10}} \ln\left(\frac{r_{g10}}{r_{rh}}\right) + \frac{r_o}{k_{air}} \ln\left(\frac{r_{air}}{r_{g10}}\right)} \tag{3.32}$$

The convection between fluid and the Ultem tube is based on the forced convection term resulting from the laminar flow in a tube, Nu=3.66 [90]. The thermal conductivity of Ultem is estimated at 0.122 W/mK [91].

3.4.5 Numerical Implementation

In Fig. 3.4 the psuedo algorithm of the numerical model is depicted. The first step temperature boundary conditions are input according to Tab. 3.3. In the built geometry step, the regenerator and dead volume properties are binned in an array corresponding to the spatial distribution along the z direction. The fluid mass flow is determined for each time step based on the displaced volume and frequency setting. And an applied field matrix is build that consists of the applied field values for each location and time step. These set of arrays and matricies are used as input variable in the governing equations.

The initial value of the temperature of the solid and fluid are input as a linear temperature distribution between T_{hot} and T_{cold}. The next time step is solved by building the tridiagonal matrix according to the discretization method that is outlined in Attachment B. Using Thomas's algorithm, the fluid tridiagonal matrix is solved yielding an updated fluid temperature array. These updated fluid temperature values are used in the construction of the solid tridiagonal matrix solution. For each time step calculation the updated values of fluid and solid temperature are compared to the previous calculated values. The relative tolerance between these two arrays is calculated to see if it is below the set threshold tolerance value, after which the next time step is calculated.

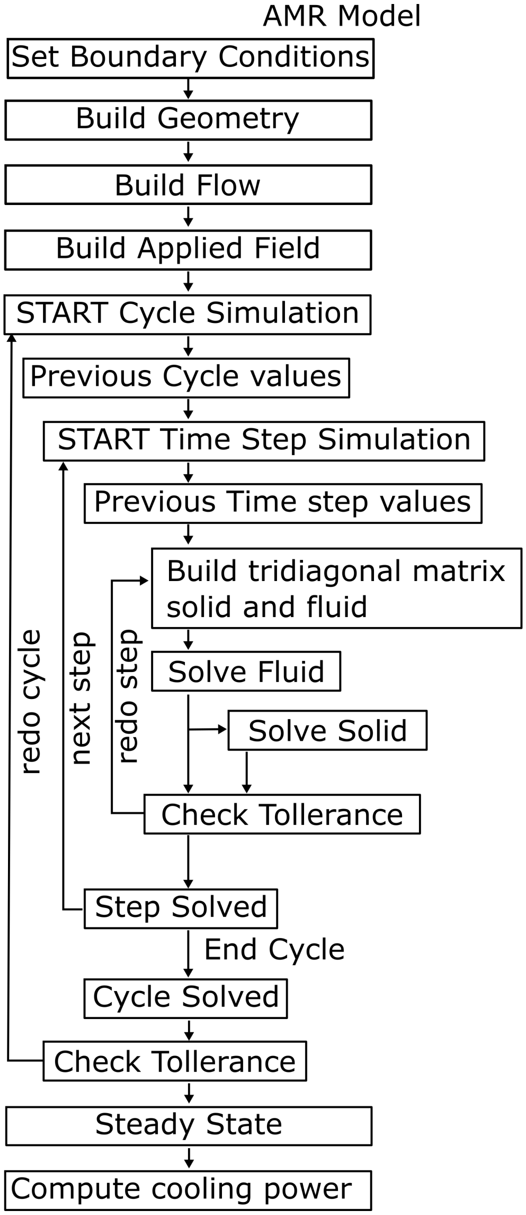

Figure 3.4: Psuedo algorithm of the AMR model.

After a full cycle is calculated, the last time step fluid and solid temperature is set as the first time step value of the cycle. This newly calculated matrix of solid and fluid temperatures is compared against the previously calculated values. When the matrices vary less than 10^{-6}, steady state is reached. At cycle steady state, the gross cooling power is extracted at the cold side of the domain using Eq. 3.33. The cooling power is determined by the temperature variation of the fluid exiting the regenerator

$$Q_{gr} = f \int_{0}^{1/f} c_{p,f}\dot{m}(T_{f,cold} - T_{cold}) \tag{3.33}$$

where $T_{f,cold}$ is the fluid temperature at the cold end.

For each configuration a region of interest, hot and cold side temperatures, are computed based on the experimental steady state points. To compare modeled gross cooling powers with the experimental results, additional correction of the cooling power is required. The gross cooling power is corrected to account for additional heat leaks on the cold side heat exchanger using Eq. 3.34 [34]

$$Q_{net} = 2 \cdot Q_{gr} - 0.28 \cdot (T_{amb} - T_{cold}) \tag{3.34}$$

where T_{amb} is the ambient temperature, 2 stands for the number of regenerators used in the PM1 and 0.28 is an empirically measured constant [92]. After post correcting the gross cooling power at each computed hot and cold side temperature boundary condition, the modelled temperature span is found interpolating cold side temperature from the experimental net applied cooling power and hot side rejection temperatures region.

3.4.6 Speed Improvements

Several improvements are made to the speed of the computation. A passive simulation is run on a laptop with a core i7-4600U. The average of 10 simulations are presented in Fig. 3.5.

The first improvement was found updating from Python 3.5.1 to Python 3.6. Then a variable step tolerance was implemented. Initially a fixed time step tolerance was used; however, it was found that using a variable tolerance increased the speed of the simulation. The first number of cycles are performed using a larger tolerance value starting at 10^{-2} decreasing until 10^{-6}. Lastly, adapting the numerical scheme from full upwind to power law gave an increase for lower frequencies and utilizations.

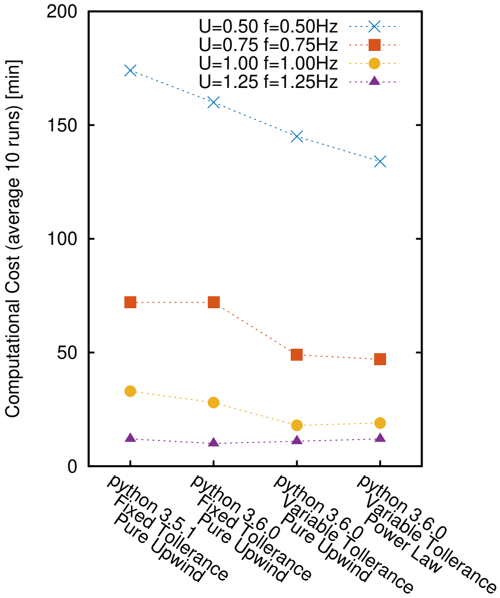

Figure 3.5: Speed increases on passive regenerator modeling for a fixed number of time nodes (nt=400) and spatial nodes (N=200).

3.4.7 Mesh Study

A mesh study was performed on regenerators with and without dead volume. Very fine meshes incur large computational costs; therefore, a compromise between simulation outcome and computation cost is made. For the regenerator without dead volume, it was found that using 400 spatial nodes and 400 time nodes gave consistent results and fast computational times. At 800 spatial nodes and 400 time nodes the simulation results with dead volume are consistent to finer meshes using a reasonable computational cost.

3.5 Results

After collapsing the temperature span by increasing the cooling load the device is let to run at a single set hot side temperature and cooling load. The steady state temperature span at each hot side temperature is reached when the temperature span varies less than 0.1 °C over a 12 minute period. This experimental steady state criteria enables us to find a steady state point at a given hot side within 2 hours of running the PM1. After a steady state point is found the next point can be determined by the device by setting a new hot side temperature. This allows us to take a sweep of different hot side temperatures in a single day. The uncertainty of the experimental steady state point is estimated ±1 °C.

It is important to note that the ambient temperature in the laboratory varies during the day. While small fluctuations tend to relate to small changes in parastic load, this can impact the steady state temperature span for a regenerator due to the small cooling powers available. In Tab. 3.6 the average and standard deviation of the ambient temperature during the experimental days are listed. The ambient temperature variation across experimental days is larger than variation during the day. Therefore the ambient temperature used to correct the gross cooling power is considered fixed for each applied cooling load and experimental configuration. The lab temperature was not recorded for the centre bed, the 2.5 W net applied load experiment, but is estimated to be 20 °C.

Table 3.6: The average ambient temperature, $T_{amb,ave}$, and the standard variation of ambient temperature, $T_{amb,st.dev.}$, between the recorded steady state points for the entire hot side temperature sweep at each net applied cooling load.

	Q_{net} (W)	$T_{amb,ave}$ (°C)	$T_{amb,st.dev.}$ (°C)
cold	0	20.1	0.1
	2.5	19.2	0.4
centre	0	20.5	0.1
	2.5	-	-
hot	0	21.1	0.9
	2.5	20.3	1.0
long	0	20.7	0.6
	10	20.6	0.4

Each experiment is simulated with and without dead volumes: one with just the regenerator section and another including the void volume sections (VV). For both simulations the two casing boundary conditions, as described in Sec. 3.4.4, are considered. Hence, in total four simulations are computed for each experiment.

We first present the results for the long regenerator, afterwards, the results of the short beds are presented.

3.5.1 Long Bed Results

The experimental and simulated results of the long regenerator are plotted in Fig. 3.6. The 0 W net cooling power results are presented separately from the 10 W results. The experimentally determined steady state temperature spans are presented as points and the simulated results as lines.

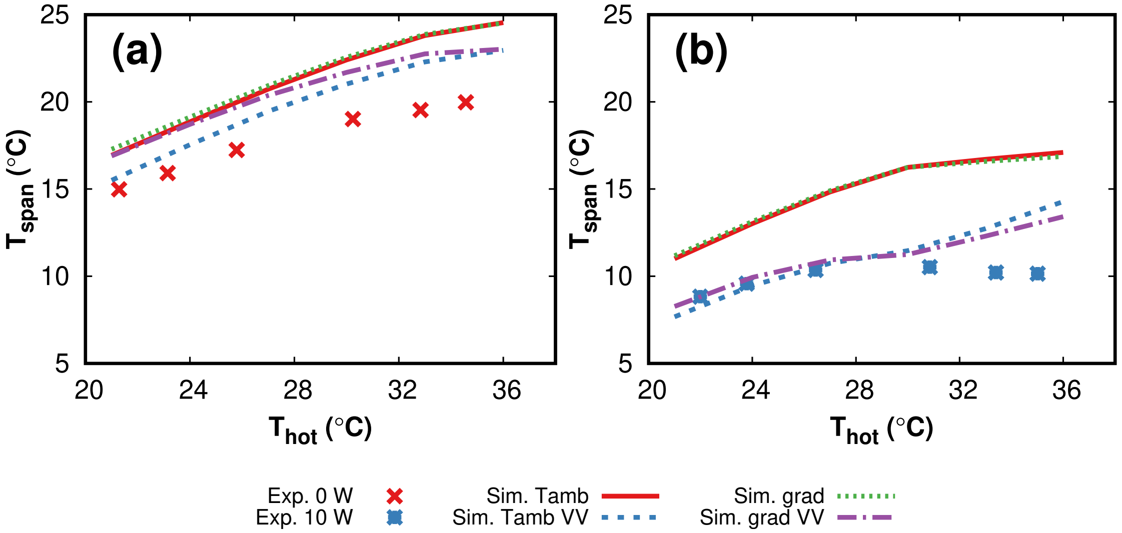

Figure 3.6: Experimental results compared to Simulation results with (VV) and without dead volume sections included for the long configuration. (a) 0 W $T_{amb,ave} =$ 20.7 °C (b) 10 W $T_{amb,ave} =$ 20.6 °C

For the 0 W load case, there is a small decrease in determined temperature span when dead volume sections are included in the simulations. However, in the 10 W case, there is a more significant decrease in temperature span with and without dead volume sections included. The results with dead volume sections better approximate the experimental results. Simulating only the regenerator section significantly overpredicts the experimental results.

When just the regenerator section is modeled the assumed casing boundary condition does not impact the modeled temperature span. Whereas, when the dead volume sections are added, the casing boundary condition assumption does vary the temperature span. The **(grad)** assumption produces the highest temperature span in the 0 W load case among the tested casing boundary conditions. Below 30 °C rejection temperatures, the simulated temperature span of **(grad)** increases compared to the **(Tamb)** approaching the no dead volume scenario.

For the 10 W net applied cooling, below 26 °C rejection temperatures the **(grad)** improves over the **(Tamb)** scenario. At higher rejection temperatures, the **(grad)** assumption produces a lower temperature span than the **(Tamb)** case.

The results from the long beds show that including dead volume sections improves the simulation to approach experimental data. With dead volume sections and varying casing boundary conditions slight variation in temperature span can be found. Using the **(Tamb)** provides the best matching solution for the 0 W case. For the 10 W, the **(grad)** marginally improves the temperature span trend over **(Tamb)**. Furthermore for the 10 W case, above 30 °C hot side temperatures, the temperature span trends upwards for all casing boundary conditions over-predicting the experimental temperature span.

3.5.2 Short Bed Results

The experimental results of the short beds in the cold, centre, and hot configurations are presented in Fig. 3.7. Fig. 3.7 shows that in terms of temperature span, the centre beds perform better than the cold and hot side beds. The main discerning experimental parameter between the centre beds and cold/hot side beds is the applied magnetic field. The average applied field values for the hot and cold bed configurations are similar while the centre beds have the largest peak and variation in applied field values. The results between the cold and hot side bed differ for the 0 W case but are similar for the 2.5 W case. The cold configuration performs better in the 0 W case than the hot side beds.

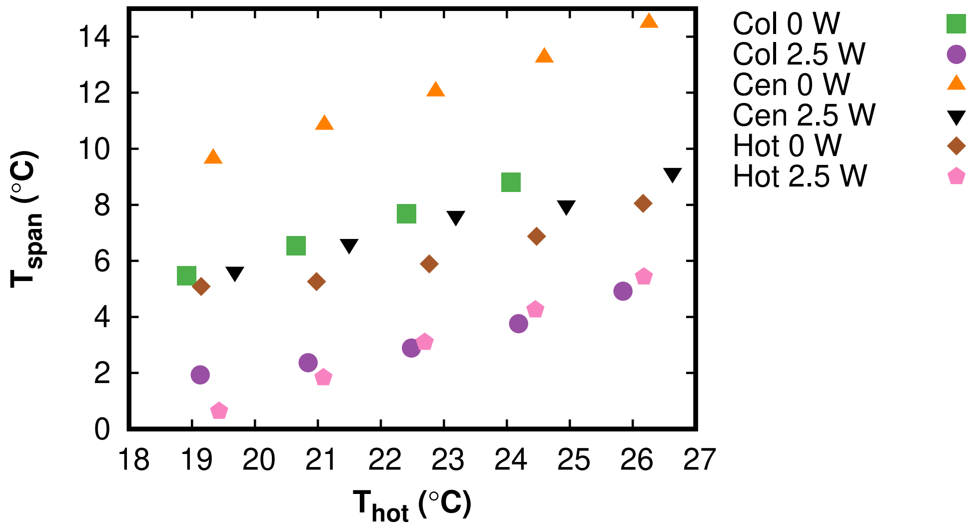

Figure 3.7: Experimental results of the differently placed regenerators. For cold (Col) side, centre (Cen) and hot (Hot) side configurations for 0 W and 2.5 W net applied load.

In Fig. 3.8, Fig. 3.9 and Fig. 3.10 the cold, centre and hot configured beds experimental results, respectively, are compared to simulated results. For each configuration and load the four simulation cases are shown. Since no ambient temperature is known for the centre bed configuration at 2.5 W, the **(grad)** assumption simulation results using T_{amb} = 20 °C results are presented. These values are representative of the ambient temperature range in the lab. T_{amb} = 19 °C was also calculated, but the variability between these results and the T_{amb} = 20 °C for the 2.5 W case are too small to display on the graph.

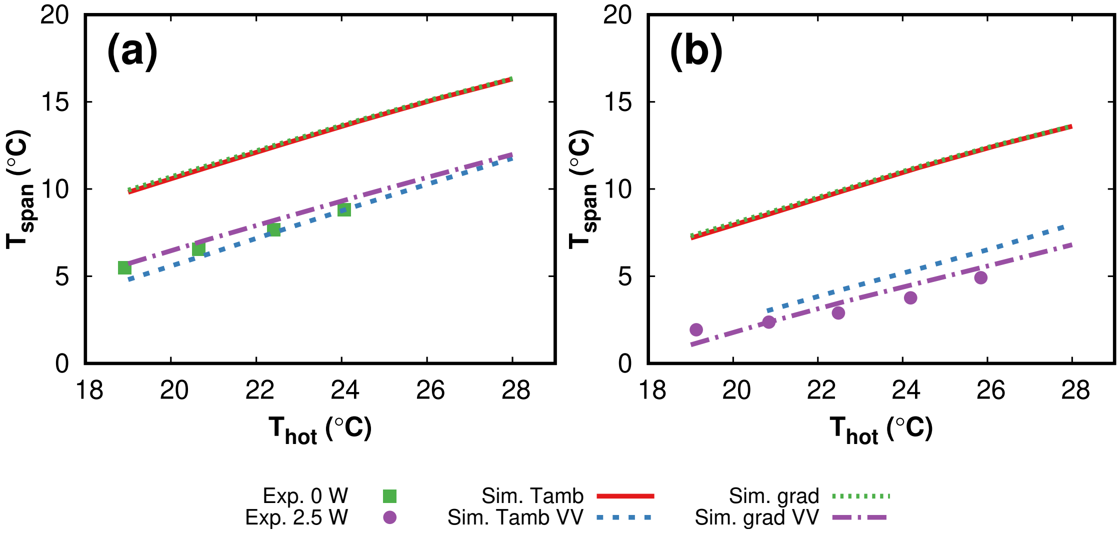

Figure 3.8: Experimental compared to Simulation results with (VV) and without dead volume included for the cold configuration. (a) 0 W $T_{amb,ave} = 20.1$ °C (b) 2.5 W $T_{amb,ave} = 19.2$ °C

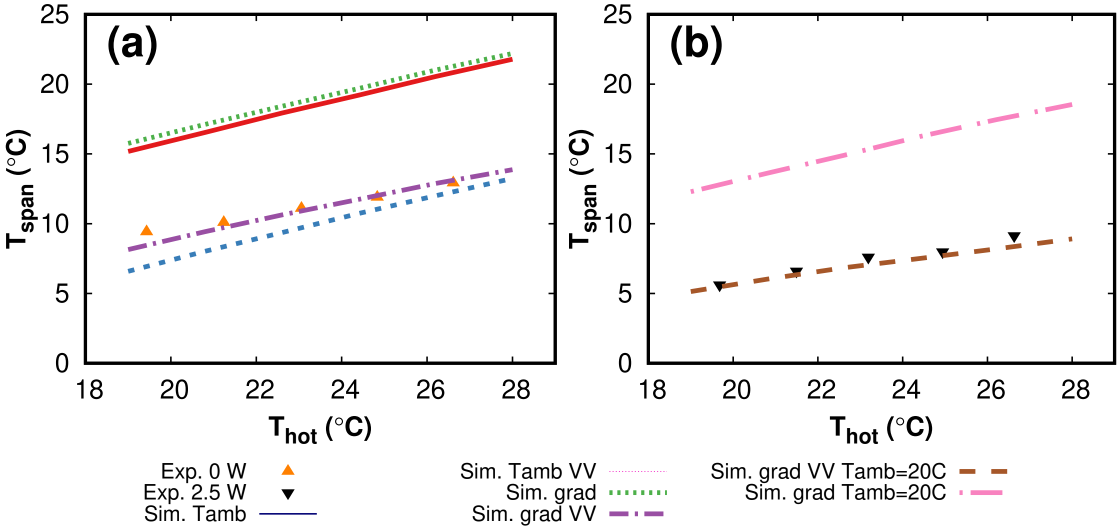

Figure 3.9: Experimental compared to Simulation results with (VV) and without dead volume included for the centre configuration. (a) 0 W $T_{amb,ave} = 20.5$ °C (b) 2.5 W considering only the grad case with $T_{amb,ave} = 20$ °C

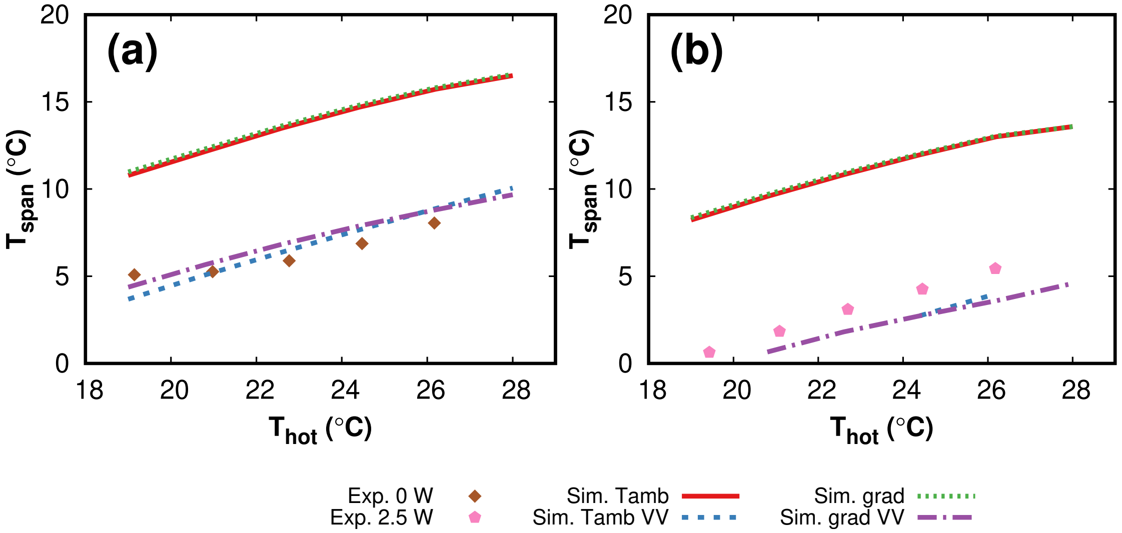

Figure 3.10: Experimental compared to Simulation results with (VV) and without dead volume included for the hot configuration. (a) 0 W $T_{amb,ave}$ = 21.1 °C (b) 2.5 W $T_{amb,ave}$ = 20.3 °C

For all configurations, the simulations considering just the regenerator section over-predict the experimentally determined temperature span. When dead volume sections are included, the simulations match well with the experimental results. The casing boundary condition can be used to fine tune the simulated temperature span to closer match the experimental results; however, the impact of casing boundary condition is small relative to dead volume. In the cases of the cold and hot configurations, the trends for the **(Tamb)** and **(grad)** are very similar since the temperature span is small and all values used are close to room temperature. In the case of the 0 W centre beds the temperature span is larger and the **(grad)** assumption produces the closest match to the experimental results. The fixed boundary condition under predict the temperature span for the 0 W case. Testing the ambient temperature of 20 °C in the 2.5 W case with the **(grad)** assumption results in good matching values between simulations and experimental results. The ambient temperature setting for this simulation only impacts the gross cooling power correction given by Eq. 3.34.

An additional simulation is performed on the centre bed configuration with dead volume sections where the casing energy term is removed. The results of this additional simulation are presented in Fig. 3.11. As can be seen for the zero watt case these losses impact the temperature span; however, for the 2.5 W simulation the temperature span results are similar to the **(grad)** assumption.

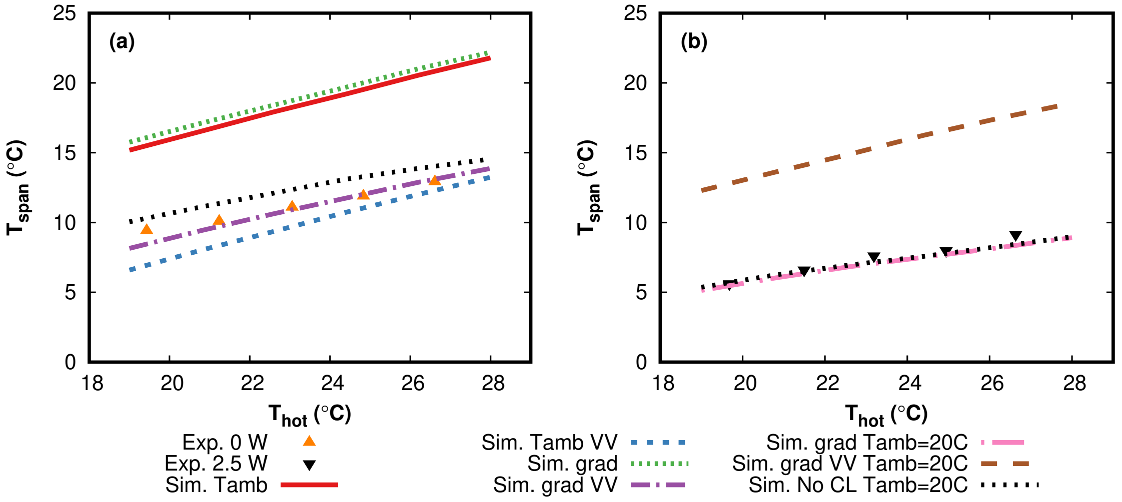

Figure 3.11: Experimental and simulation results with (VV) and without dead volumes for the centre configuration. Two additional cases are shown where casing losses are fully neglected. (a) 0 W $T_{amb,ave} = 20.5$ °C (b) 2.5 W considering only the grad case with $T_{amb,ave} = 20$ °C

In most simulation cases for the short regenerator beds the **(grad)** assumption provides the closest match between experimental and simulation results.

3.6 Discussion

Agreement between experimental and simulation results for the short regenerators requires the inclusion of the dead volume sections and casing losses in the system model. For the configurations tested, the dead volume has the most significant impact with better agreement to experiments for zero and loaded conditions. The casing losses have the largest measurable impact for the low cooling power simulations where the span is larger. At larger cooling powers the impact of casing losses is diminished on the determined temperature span curves. This is shown by the fact, in the long regenerator beds a variation in temperature is found on the zero watt cooling power temperature span curve, but little variation is found for the 10 W curve. Similarly, Fig. 3.11 shows that when the casing loss term is removed for the short centre beds, the 0 W simulated temperature span is found to over-predict the experimental results. However, for the 2.5 W net applied load, the results with no casing losses are similar to the **(grad)** boundary condition results.

The casing losses model considers a single boundary condition along the regenerator outer components. We found that when just the regenerator section is considered the casing losses do not impact the predicted regenerators temperature span performance. When dead volume sections are included a variation in the predicted temperature span is found with different casing boundary condition assumptions. By defining the casing boundary temperature we are assuming that the actual fluid temperature in the regenerator does not have an impact on the casing temperature. This may be a poor assumption since the temperature profile in the fluid may differ considerably from the assumed casing temperature. For example, Fig. 3.12 shows the simulated fluid temperature along the domain at maximum hot and cold blow points in the AMR cycle for the centre configuration.

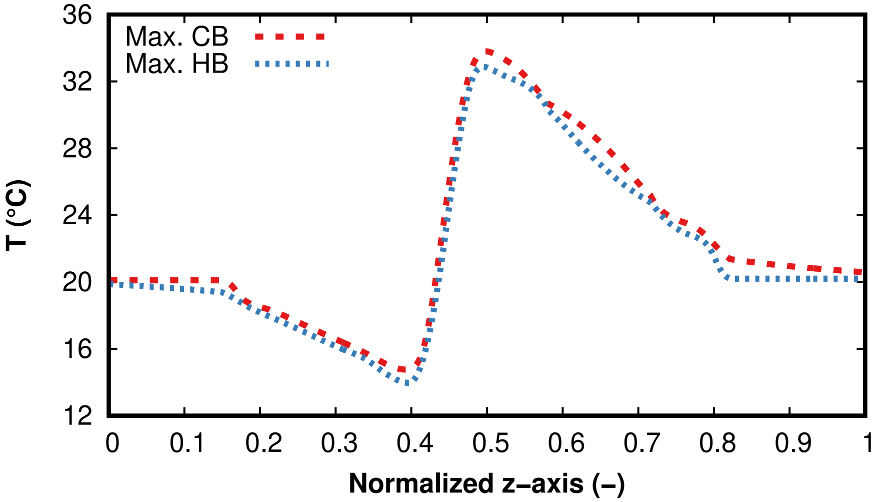

Figure 3.12: The fluid temperature at the maximum hot and cold blow points in the cycle for the short centre place regenerator with T_{hot} and T_{cold} at 20 °C. The casing boundary condition that is tested is the **(grad)**.

The hot and cold side fluid boundary conditions are set at 20 °C and the casing boundary condition is set to **(grad)**. The **(grad)** results in a constant temperature along the casing since the temperature hot and cold side boundary conditions are equal. A weak thermal link between the regenerator and the heat exchangers is found for this configuration on both sides. At the hot side of the regenerator the temperature is at 33 °C while at the cold side the temperature is at 14 °C. This leads to a large temperature difference between the fluid and boundary condition, as well as a large thermal gradient between regenerator and heat exchangers. One would expect the fluid temperature to impact the adjacent system components and those components to thermally interact with each other. This will cause heat interactions with the outer components of the PM1 impacting the casing temperature boundary condition in a dynamic way. As discussed in the introduction, this interaction can be captured by coupling a 2D conduction model of the outer system components to the 1D AMR system model. However, as shown here, the casing loss is less important for this AMR geometry than the dead volume, therefore allowing the use of a simplified boundary condition [52].

The experimental results of the short regenerators vary due to dead volume location as well as differences in magnetic field. The centre beds are placed such that $\Lambda_0 = 0.5$ and the regenerator is subjected to the largest amplitude magnetic field waveform. Between the hot - $\Lambda_0 = 0.8$ - and the cold beds - $\Lambda_0 = 0.2$ - there is a large difference in cold-side dead volume fraction; however, there is little variation in the average applied magnetic field. From the experimental results, we see that the centre beds produce the largest temperature span among the short beds. This is directly correlated with the higher applied field values. The cold side beds perform better than the hot side beds for the 0 W curve; however, cold and hot are similar for the 2.5 W net loading curve. The 0 W curve is highly susceptible to heat leaks.

Experimental results show that the zero-watt temperature span curves for hot and cold configurations vary by approximately 2 K at rejection temperatures of 22 °C and 24 °C. Based on simulated results, the dead volume fraction and the total dead volume difference may explain the performance drop between hot and cold beds. At equal ambient temperature, a larger dead volume fraction will decrease the modelled temperature span. As shown in Fig. 3.12, dead volumes result in reduced thermal coupling between the AMR and the heat exchangers.

The difference in temperature span falls within the uncertainty of the experimentally determined steady state points which makes it difficult to determine if the dead volume variation between hot and cold side regenerators is the cause of the temperature span difference. Another factor is the variation in ambient temperature that may impact the casing heat leaks. The zero watt tests for the cold configuration are taken at a lower ambient temperature than for the zero watt hot configuration. In the latter case, the hot side zero-watt curve experienced an ambient temperature of 21.1 °C while the cold configuration ambient temperature was 20.1 °C. This will benefit the cold side regenerator leading to a larger temperature span. While the differences in ambient temperature are small, the variability on the zero watt curve compared to the 2.5 W cooling power temperature curve are more significant when void volumes are significant.

3.7 Conclusion

In this Chapter we experimentally and numerically study the impact of void volume and casing heat transfer losses on active magnetic regenerator performance. Different regenerator configurations in terms of length and location are tested, varying location results in a change in applied field and the size and volume of void space outside the regenerator.

The two-dimensional structures comprising the AMR system are simplified to a 1D domain. This provides a simpler approach than using a 2D external casing model [52]. This simpler approach is shown to be satisfactory for cases analyzed here due to dead volumes dominating the loss. The casing loss does impact predicted performance, but to a lesser degree for the PM1 device. For this reason, the assumed boundary condition for the casing is found to have a small impact on simulated temperature span.

Improving the ambient temperature control or improving the thermal isolation of the apparatus would benefit experiments using small regenerators with dead volumes. The void spaces outside the regenerator can be reduced by using small capillary tubing, glass spheres and check valves; however, small dead volume can impede performance due to flow maldistribution as shown elsewhere [75]. Design choices for optimizing structure of AMR devices warrant further study.

Chapter 4

Two Layer Experimentation

The content of this Chapter is published in Journal of Physics D:Applied Physics [61].

Experimental study of 2-layer regenerators using MnFeSiP materials

T.V. Christiaanse[1], P.V. Trevizoli[1,2], Sumohan Misra[3], Colman Carroll[4], David van Asten[5], Lian Zhang[5], R. Teyber[1], P. Govindappa[1], I. Niknia[1], A. Rowe[1]

[1]University of Victoria, Victoria, B.C. Canada
[2] Department of Mechanical Engineering. Ingá University Center (UNINGÁ),
Rod. PR-317, 6114 - Parque Industrial 200, Maringá, PR, 87035-510, Brazil.
[3]BASF SE Ludwigshafen, Luwigshafen am Rhein, Germany
[4]BASF Future Business, Luwigshafen am Rhein, Germany
[5]BASF Nederland, De Meern, The Netherlands

The idea of this experimental work is to look at the Curie spacing between two layers of Mn-Fe-Si-P material. In this Chapter the experimental methods and data of the 2-layer materials are presented and discussed.

4.1 Abstract

An experimental study determining impacts of composition in a two layer active magnetic regenerator is described. Five Mn-Fe-Si-P materials with Curie temperatures of 294.6 K, 292.3 K, 290.7 K, 282.5 K and 281.4 K are used. These materials are tested as two layered regenerators using an active magnetic regenerator cycle. Three sets of experiments are performed. First, a reference configuration consisting of the 294.6 K material with a second passive layer of lead is tested. Second, the remaining active materials are used as cold layers with the same 294.6 K material as a warm layer. Lastly, a regenerator is created from the 294.6 K and 282.5 K materials. The temperature span is measured for rejection temperatures from 40 °C to 9 °C and at 0 W and 2 W applied load. The experimental results for temperature span and exergetic cooling power are compared based on the differences from the reference configuration. Materials are analyzed based on performance metrics such as peak adiabatic temperature change, peak entropy change and RCP(s) values. It is found that a closer Curie spacing can yield a greater temperature span and exergetic cooling power than further spaced materials, even when materials are used with lower performance metrics. These results show that materials with lower adiabatic temperature change and lower entropy change can outperform materials with higher values when close Curie spacing is used in a layered regenerator at appropriate rejection temperatures.

4.2 Introduction

The development of magnetic heat pumps faces several challenges arising from the nature of the magnetocaloric materials, to the components of an active magnetic regenerator (AMR) [12, 21]. The latter includes the magnetic circuit [93], regenerator bed geometry [14], heat exchangers, and pumping system. A specific area of research is layering of first order materials to create low-cost and high performance regenerators. Layering refers to the arrangement of several materials with different properties in an

AMR. Layered regenerators may use second order materials (SOM's) or first order transition materials (FOM's). Even though SOM's based on rare earths have been successfully employed in AMR's, they tend to use expensive constituents. FOM's, in turn, can be composed of less expensive constituents and, therefore, are more attractive for commercial applications near room temperature [13].

Several works have addressed the challenges of layering materials in an AMR. Simulation studies have been published on layering of SOM's [38, 39, 40, 42, 43, 41, 94], FOM's [36] and a combination of FOM's and SOM's [44, 35, 46, 45]. Experimental results have been published on layering SOM's [23, 24, 95, 25, 27, 96, 26, 97, 33, 98, 99], FOMs [100, 101, 29, 30, 22, 102] and comparing SOM and FOM layered regenerators [103, 104, 105, 106, 28, 107, 31]. Most of these studies use Lanthanum based alloys as an example of a FOM, except for a recently published study which; showed a 32 K temperature span using 8 layers of Mn-Fe-As-P materials [22]. Experimental studies on layering explore varying material properties in a parametric manner. Tušek et al. describes the use of two, four and seven layers of Lanthanum-based material and the impact on temperature span [31]. Saito and Nakagome report a study using one, two and three layers of a SOM material, with an additional three layer configuration where the mass ratio between layers is changed [98]. Teyber et al. study effects of Curie temperature spacing between two SOM materials [99]. Govindappa et al. report a three, six and eight layer experiment with FOM Mn-Fe-As-P material where the impacts of number and thickness of layers is described [22]. A similar study was performed using La materials by Navickaitė et al.; three, five and nine layers of La materials are tested [102]. Balli et al. recently published a review paper summarizing different FOM layering studies [104].

FOM materials from the Mn-Fe-Si-P system are of interest for AMR applications because the constituents are abundantly available and non-toxic [15]. By tuning the ratio of the constituents the transition temperature can be altered to lie between 220 and 380 K [57]. The peak entropy and adiabatic temperature change which occur around the transition temperature of the Mn-Fe-Si-P family can be higher than those of SOM's; however, like other FOM's, the width of the peaks are narrow, thereby requiring the use of layering.

While the Mn-Fe-Si-P system appears to be promising for AMR applications, there is little data in the literature regarding experiments using layered regenerators comprised of these materials. Moreover, previous reports of layering with FOM materials tend to focus on number of layers without a rigorous examination of the impacts of property variations for a fixed number of layers. Given the complexity of the thermodynamic problem, the uncertainty in material properties, and the differences between test devices, the ability to create layered AMR's with desired performance is still a challenge.

This work examines performance of layered regenerators using Mn-Fe-Si-P materials. A set of five materials with different constituent ratios, transition temperatures, and thermal hysteresis are tested in an AMR cycle. The material transition temperatures are near room temperature (297 K) with a thermal hysteresis less than 1.5 K. The materials are combined to create six different 2-layer regenerators; a reference regenerator structure uses one active layer and a passive second layer of lead spheres. We experimentally investigate the impact of Curie temperature spacing and magnetocaloric properties on temperature span and exergetic cooling power produced by the regenerator. Numerous steady-state tests are performed for each regenerator with varying rejection temperature and heat loads.

The following section describes the experimental apparatus, materials, and test procedures. The metrics used to characterize and report results are explained. Finally, the differences in performance are discussed and compared using common material metrics.

4.3 Experimental Methods

In total, six experiments with the available Mn-Fe-Si-P materials are performed. Three set of experiments are performed consisting of: (i) a hot side layer with a passive cold side material; (ii) four additional experiments where the same hot side material is used from (i) while a cold side layer is added with decreasing transition temperature and; (iii) a regenerator is made from two materials previously used as cold side layers from (ii). The experiments are performed in the PM I device [60] using a displaced volume of 2.76 cm^3 and frequency of 1 Hz. The hot side temperature is varied between 40 °C and 9 °C with increments of -1 °C under zero and 2 W applied cooling load conditions. The results are presented as a function of temperature span and gross exergetic cooling versus hot side rejection temperature. Details of the device, material properties, regenerator structure, and test method are presented in the following sections.

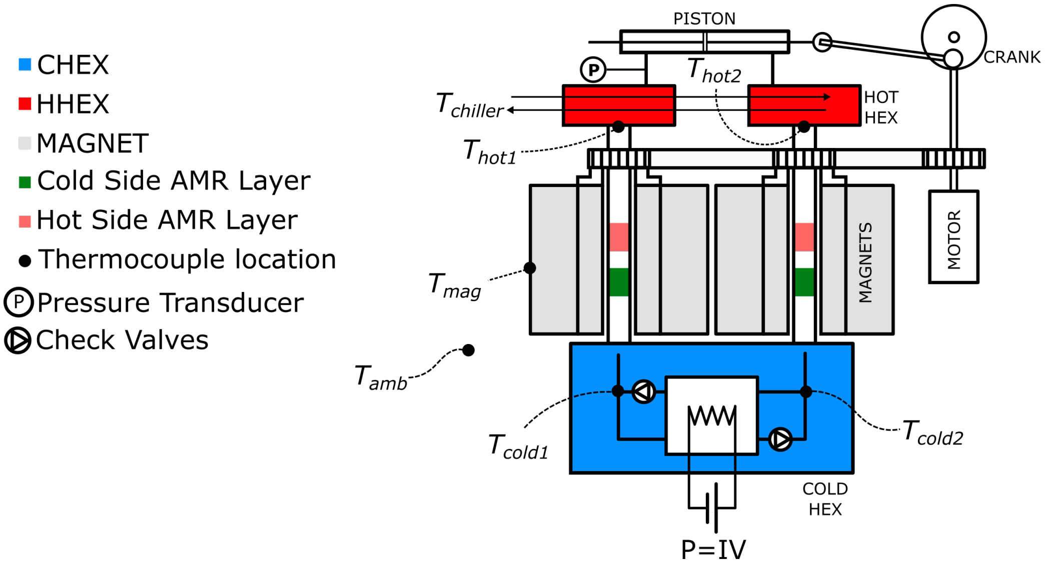

Figure 4.1: Schematic drawing of the PM1 prototype system providing the location of the various thermocouples.

4.3.1 Description of the Experimental Apparatus

The permanent magnet device (PM I) shown schematically in Fig.4.1 is used for the experiments [60]. The magnetic field is generated by two cylindrical nested Halbach arrays [108]. Each array has a magnetic field transverse to the bore direction. The inner Halbach array rotates with respect to the outer array to create a peak field of 1.47 T. When the arrays oppose each other a minimum field of 0.09 T is obtained. The inner bore has a diameter of 19 mm through which the AMR housing connects to hot (HHEX) and cold (CHEX) heat exchangers. Dead volumes between the regenerator matrix and heat exchanger surfaces are reduced by using glass spheres to fill the remaining void space.

The heat transfer fluid is 79.5 % water, 20 % ethylene glycol and 0.5 % corrosion inhibitor (supplied by BASF SE.) Fluid is oscillated by a piston through a loop consisting of the HHEXs, AMR housings, and CHEX. The CHEX has check valves to promote unidirectional flow between the heat exchanger surface and the regenerator, thereby reducing dead volume. The HHEX controls the rejection temperature by exchanging heat with a temperature controlled recirculating chiller.

Pressure drop is measured by an OMEGA PX613 300G5V pressure transducer installed between the piston and the HHEX. OMEGA E-type thermocouples are installed at various locations of the system. Thermocouples are installed between the HHEX and CHEX for each regenerator. The reported hot side (T_{hot}) and cold side temperature (T_{cold}) are based on the average reading of the thermocouples. Two additional thermocouples measure magnet and ambient temperature. Data are collected using Labview®DAQ software with NI 9213 DAQ and NI 9205 DAQ cards used for temperature and pressure sensors respectively. The cooling power is applied to the CHEX by an Omega KHLV-202/10 film heater. The heater voltage and current are supplied by a HP E3631A DC power supply.

4.3.2 Materials Preparation and Regenerator Construction

The Mn-Fe-P-Si materials are produced by BASF SE using gas atomization to create particulate from which a block is formed via sintering at 1100 °C for 20+ hours. The block is ground to produce irregular particles which are sieved to between 300-425 μm (nominal size 360 μm). Several materials are produced using this method with different loading ratios for the elemental constituents. Resulting particles are screened for hysteresis and transition temperature using zero field specific heat measurements. Samples of each material set are then characterised using in-field specific heat, magnetisation and adiabatic temperature change measurements. After correcting for demagnetising fields, the entropy diagram for each Mn-Fe-P-Si material is constructed as described in detail by Christiaanse et al. [20]. The loading material composition before gas atomization, transition temperatures, mass and length for each regenerator is listed in Table 4.1 [1]. The PM I device requires two regenerators, one for each Halbach array.

Table 4.1: Properties of the materials (a) and regenerator (b). This table has been updated with porosity values.

(a)		Transition Temperature (K)			
	Field	0 T	0 T	1 T	1 T
Name	Material	Heating	Cooling	Heating	Cooling
M1	$Mn_{1.16}Fe_{0.75}P_{0.47}Si_{0.53}$	294.7	294.5	294.7	294.5
M2	$Mn_{1.18}Fe_{0.73}P_{0.48}Si_{0.52}$	292.6	292	292.6	292
M3	$Mn_{1.16}Fe_{0.74}P_{0.47}Si_{0.53}$	290.7	290.7	290.7	290.7
M4	$Mn_{1.205}Fe_{0.715}P_{0.49}Si_{0.51}$	283.6	282.4	283.6	282.4
M5	$Mn_{1.21}Fe_{0.74}P_{0.49}Si_{0.51}$	281.3	281.5	281.3	281.5

(b)	packed bed properties					
	length (mm)		mass (g)		porosity(-)	
Name	1	2	1	2	1	2
M1	22	23	12.3	13.0	0.53	0.53
M2	22	23	12.8	12.9	0.52	0.52
M3	23	23	12.4	12.4	0.54	0.55
M4	22	17	12.3	9.5	0.53	0.52
M5	23	22	12.1	13.1	0.57	0.50

The magnetocaloric properties can vary significantly between each composition

---

[1] The mass for the M1-M2 and M4-M5 are incorrectly stated in the publication. This table here contains the correct values for all materials. The editor has been notified of the error. The error does not impact the conclusions of this Chapter or the paper.

[20]. The constructed ΔT and Δs are based on low field heating and high field cooling entropy curves [53, 56, 20]. The field values are based on the internal field values of the regenerator in the PM 1 device. Accounting for the PM I magnets [60], the regenerator shape [85], porosity [109], and material properties [20], the average internal fields are estimated to be approximately 0.3 T and 1.0 T during low and high field blow periods. The modelled adiabatic temperature change and entropy change for the average low and high fields are shown in Fig. 4.2 for each material. The temperature at which we find peak adiabatic temperature change and the FWHM of the adiabatic temperature change curve is listed in Table 4.2.

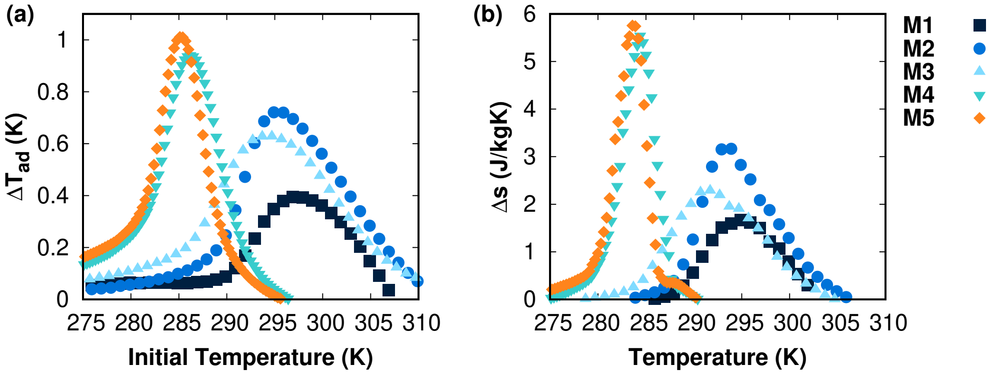

Figure 4.2: Material properties (a) adiabatic temperature change (ΔT (K)) and (b) entropy change (Δs (J/kgK)) extracted from [20] using heating low field to cooling high field. Low field and high field during the blow period is estimated to be 0.3 T to 1.0 T, respectively. Lines are added to guide the eye.

Table 4.2: Temperature of peak adiabatic temperature change and full width half maximum (FWHM) of the adiabatic temperature change curves of each material. These values are extracted from the material data presented in Fig. 4.2(a).

	ΔT_{ad} peak (K)	FWHM (K)
M1	297.1	9.5
M2	295.4	12.1
M3	294.2	14.3
M4	286.2	6.6
M5	285.2	5.4

Individual materials are packed in a G10 tube and tubing segments are assembled to create a two-layer regenerator configuration as shown in Fig. 4.3. Each tube of material is of equal length with connector fixtures on either side. This modular design allows for the exchange of hot and cold layers to create desired combinations of materials. An intermediate connector between materials results in 2.26 cm^3 void volume between the layers. In addition, due to the short length of the beds there is void volume on either side of the regenerator; this void space is reduced by filling with 3.18 mm diameter glass spheres.

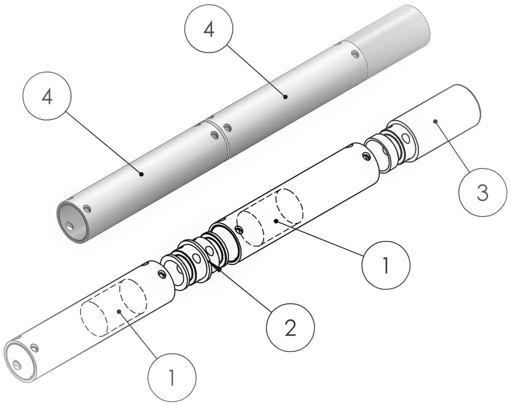

Figure 4.3: Modular design of the regenerator. (1) Packed bed regenerator based on crushed particulate of Mn-Fe-Si-P material. The distance from the centre of the magnet to the face of the regenerator is kept constant; however, the length of the bed varies as indicated in Table 4.3. (2) Intermediate connector, this is placed at the centre of the magnetic field source. (3) End connector, this plug fits into the hot side heat exchanger. (4) G10 tubing that is used to house the regenerators.

4.3.3 Experimental Methods

The different regenerator configurations are listed in Table 4.3. For the first five regenerators (R1-R5) the hot side material is M1. The R1 regenerator has a 23 mm long passive cold layer constructed from 300 μm lead spheres. The lead spheres are used to approximately maintain the overall thermal and hydraulic properties of each regenerator combination. For all remaining regenerators, the passive layer is replaced with an active material such that the cold side Curie temperature is varied from 292.3, 290.7, 282.5 to 281.4 K. A sixth regenerator configuration is also constructed using the 292.3 K transition temperature material (M2) as hot side material and 282.5 K transition temperature material (M4) as the cold side material.

Table 4.3: Regenerator configuration naming convention.

	Transition temperature (K)				
Name	First layer		Second layer		Spacing (K)
R1	M1	294.6	Lead Spheres		-
R2	M1	294.6	M2	292.3	2.3
R3	M1	294.6	M3	290.7	3.9
R4	M1	294.6	M4	282.5	12.1
R5	M1	294.6	M5	281.4	13.2
R6	M2	292.3	M4	282.5	9.8

4.3.4 Data Analysis

Regenerators are tested with applied heat loads of 0 W and 2 W. The temperature span is recorded at steady state for hot side temperatures varying between 40 °C and 9 °C. For all experiments the frequency and displaced volume are fixed. The displaced volume, 2.76 cm^3, is selected to overcome the dead volume due to the intermediate connector. The frequency is 1 Hz to restrict stress on the packed beds due to pressure drop and to lower the chance of the packed structure breaking apart.

Results are presented using temperature span, T_{span}, and gross exergetic cooling power, E, versus hot side rejection temperature, T_{hot}. Temperature span is based on the difference between hot and cold side temperatures at steady state. Some variation in temperature span is due to uncontrolled changes in ambient temperature. Due to the small amount of material being tested, cooling powers are small and parasitic heat leaks are significant. Heat leaks from ambient are included in calculating gross exergetic cooling power of a regenerator [34]. The gross exergetic cooling power is defined by

$$E = Q_{gr} \cdot \frac{T_{span}}{T_{cold}} \tag{4.1}$$

where Q_{gr} is the gross cooling power given by

$$Q_{gr} = Q_{net} + Q_{amb} \tag{4.2}$$

where Q_{net} is the net applied load to the cold hex and Q_{amb} is the load due to the heat leaks. This is calculated by

$$Q_{amb} = K_{amb \leftrightarrow cold} \cdot (T_{amb} - T_{cold}) \tag{4.3}$$

where T_{amb} is the ambient temperature measured at steady state. $K_{amb \leftrightarrow cold}$ is 0.28 W/K, which is estimated by Burdyny et al. for the PM I device [92].

4.4 Results

Fig. 4.4 (a) and (b) present the temperature span and the exergetic cooling power versus hot side rejection temperature of the R1 configuration where material M1 is layered with lead spheres. The red circles indicate data for an applied (or; net) load of 0 W while the green squares are for 2 W applied load. The operating range of the material is graphically indicated at the top of the plot. The green squares indicates the temperature at which we find the peak adiabatic temperature change when using the average low and high internal fields; the horizontal line shows the extent of FWHM of the adiabatic temperature change curve.

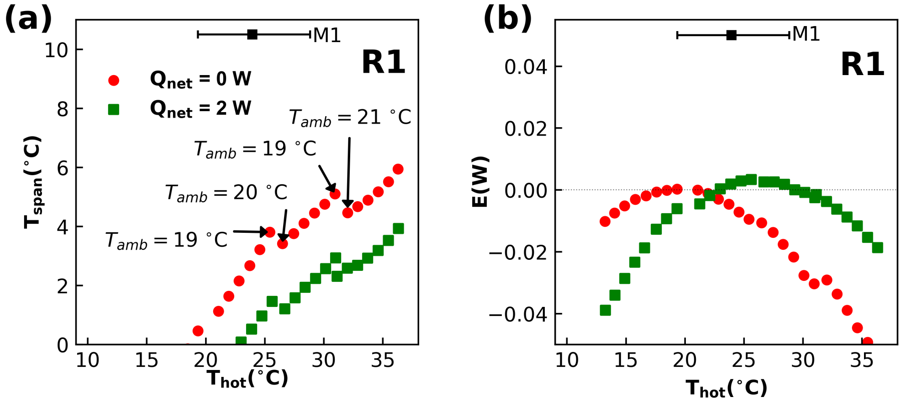

Figure 4.4: (a) Temperature span (T_{span}) versus hot side temperature (T_{hot}), and (b) gross exergetic cooling power versus hot side temperature for R1 regenerator. Some discontinuities in the trend can be explained by the ambient temperature variation, as an example for four points on the 0 W curve.

The collection of steady-state temperature span's are a result of multiple days of experiments where a typical point represents more than an hour of operation. The device is stopped at the end of each day and then restarted the following day. As seen in Fig. 4.4(a), this procedure leads to some discontinuity between the measured spans recorded on different days. There are two main reasons for this behaviour which are related to the test apparatus: (1) hourly and daily changes in ambient temperature (T_{amb}) of the device environment (external dynamics), and (2) transient effects in the device (internal dynamics). The cooling power of the regenerators is small, and, as a result, external and internal dynamics impact the steady-state conditions. Internal forces impacting dynamics are due to thermal masses such as the cold heat exchanger and the magnets. Due to the large thermal mass of the magnets, it can take 2-3 hours for the device to reach a steady-state. These internal transient effects are mitigated by running an experiment for a sufficient amount of time. Periodic steady-state is assumed once the measured average temperature span varies less than 0.1 K for 12 minutes. The data is collected and then the hot side temperature is decreased by 1 °C.

The remaining ambient leak component (1) is addressed by presenting the gross exergetic cooling power. As can be seen in Fig. 4.4 (b), the gross exergetic power tends to remove some of the discontinuities seen in span. In any case, in analysing the results, we focus on comparing differences in performance between the reference configuration R1 and the other configurations.

Based on the results in Fig. 4.4 (a) it appears that the R1 regenerator is able to provide some useful cooling power over a positive temperature span. However, Fig. 4.4 (b) indicates that the gross exeregtic power is near zero or negative for the range of rejection temperatures where temperature span is positive. This is due to the heat leak term in Eq. 4.2 accounting for heat transfer between the ambient and the cold heat exchanger. In effect, the heat leak is largely responsible for the positive temperature span - not the AMR cycle - because the cold heat exchanger is warmer than the ambient temperature. The negative gross exergetic cooling power for the R1 configuration captures the false signal generated by imperfect thermal isolation.

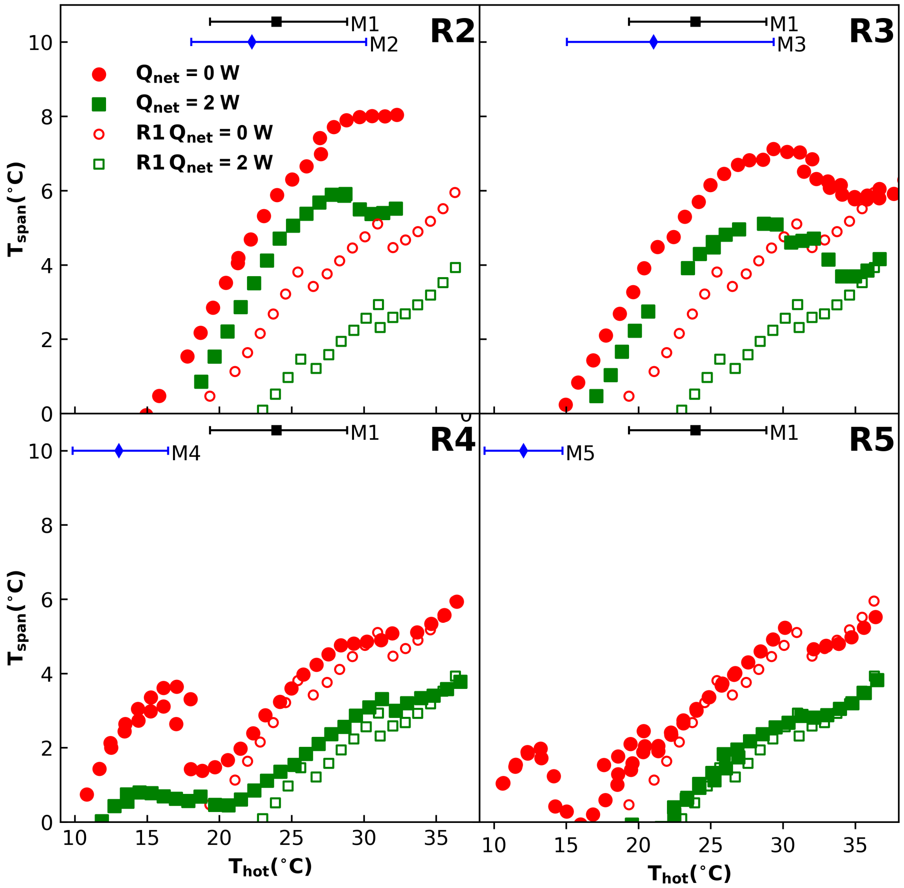

Figure 4.5: Temperature span (T_{span}) versus hot side temperature (T_{hot}) for the R2-R3-R4-R5 configurations. The results from the R1 bed are plotted using the open markers to ease comparison.

In Fig. 4.5 the temperature span (T_{span}) versus the hot side rejection temperature (T_{hot}) is plotted for the R2-R3-R4-R5 configurations using solid markers. Each of these configurations contain, the same hot side material used in the R1 regenerator. To show the differences arising with the varying cold side layers, results from the R1 experiment are plotted in each configuration using open markers. For each layer, the peak and FWHM temperatures are presented at the top of each plot. The blue squares indicate the hot side layer while the black diamonds the cold side layer.

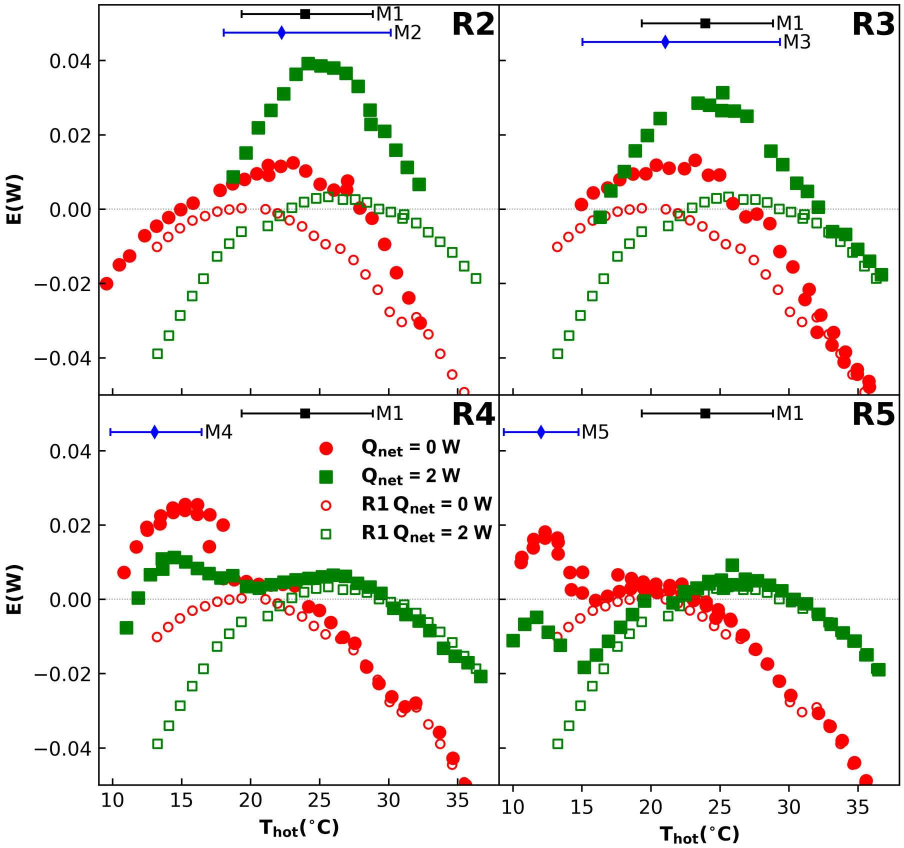

Figure 4.6: Gross exergy (E) versus hot side temperature (T_{hot}) for the R2-R3-R4-R5 configurations. The results from the R1 bed are plotted using the open markers to ease comparison.

Two characteristics are changing in R2-R5: the spacing between activity of the layers is increasing, and FWHM of the magnetocaloric effect. By comparing the solid markers and open markers, the impacts of the two effects on temperature span are evident. As might be expected, replacing the passive layer with active material generally increases the temperature spans. In the cases of R2 and R3, the spacing between layers is small. This leads to an enhanced temperature span performance compared to R1. The region of improved temperature span is near the operating range of the materials. With R4 and R5, the spacing between layers is larger. At higher rejection temperatures, the second layer is outside the active range and the results are similar to the R1 case. At lower rejection temperatures, the second layer becomes active while the warm layer becomes inactive, resulting in a range of operating temperatures where a local minimum arises. Likewise, the location of peak values tend to correlate with the operating range of the individual materials.

The gross exergetic cooling power for each configuration is displayed in Fig. 4.6. The plots for R2 and R3 show the value of layering more clearly when compared to R1. In the R4 and R5 regenerators, the peaks found at lower rejection temperatures align with the operating range of the M4 and M5 material, respectively. At higher rejection temperatures, the performance curves align closely with the operating range of the M1 material. One interesting observation is that the maximum exergetic cooling power is found at lower rejection temperatures where only the cold layer is active.

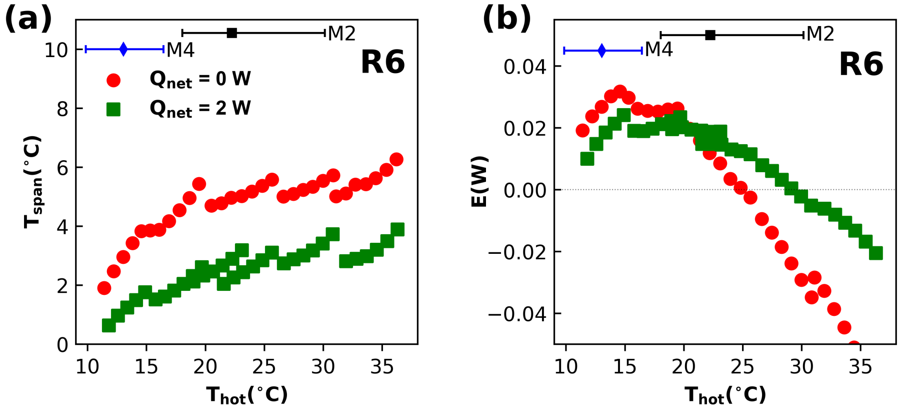

Figure 4.7: (a) Temperature span (T_{span}) versus hot side temperature (T_{hot}), and (b) gross exergetic cooling power versus hot side temperature for R6 regenerator.

Results for the R6 regenerator which combines M2 and M4 are shown in Fig. 4.7. Positive gross exergetic cooling powers are found at rejection temperatures coinciding with the operating range of the M2 and the M4 materials. The R2 regenerator and R6 regenerator use the same M2 material; however, in the case of R6, M2 is the hot side layer whereas in R2 it is the cold side layer. The Curie spacing between layers is 2.3 K for R2 and 9.8 K for R6. These two regenerators perform differently with respect to their optimal rejection temperature and exergetic cooling power. In the case of the R2 regenerator the peak exergetic cooling power is at 25.6 °C rejection temperature which is closer to the M1 operating range. In the case of the R6 regenerator the peak performance is near a rejection temperature of 14.6 °C which is in the operating range of the M4 material.

When the exergetic cooling power of the 2 W net applied load curve is higher than the 0 W curve, the beds might be able to produce a higher cooling power. However, if the exergetic cooling power of the 0 W is higher no higher exergetic cooling could be achieved. The exergetic cooling power produced by the R2 and R3 beds therefore might be improved on if more experiments where done.

4.5 Discussion

The impacts of two active layers are summarised in Fig. 4.8 which shows (a) the differences in maximum temperature span and, (b) gross exergetic power for R2-R6 with respect to R1 performance. Results are plotted with respect to spacing between layer Curie temperatures. While this is not the only parameter that determines performance, there is a correlation between maximum differences and Curie spacing for the regenerators considered. In Fig. 4.8 (a) the largest increase in temperature span is for the R2 regenerator with 7.2 K for the 0 W experiments and 3.7 K for the 2 W experiments. This configuration has the closest Curie temperature spacing of 2.3 K. R3 has the next largest increase in temperature span with 6.0 K for the 0 W experiments and the 2.9 K for the 2 W experiments. This configuration has a 3.9 K Curie spacing.

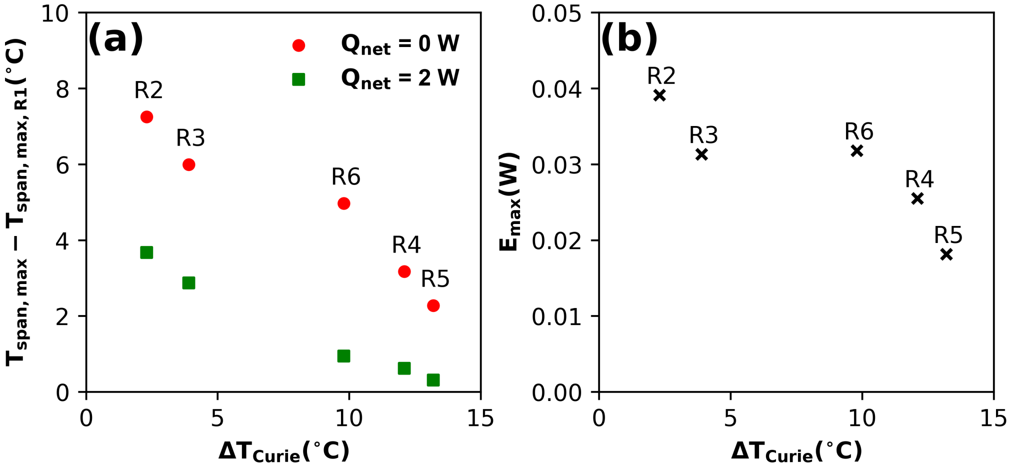

Figure 4.8: (a) Maximum temperature span ($T_{span,max}$) minus the maximum temperature span of the R1 regenerator ($T_{span,max,R1}$) versus Curie spacing between layers (ΔT_{Curie}). (b) Maximum gross exergetic cooling power (E_{max}) versus Curie spacing between layers (ΔT_{Curie}) for each configuration.

Fig. 4.8 (b) shows the maximum exergetic cooling power of the R2-R6 regenerators. Unlike temperature span, decreasing performance does not correlate as well with increased spacing. This is evident with the R6 performance being similar to the R3.

Table 4.4: Performance metrics based on $H_{low,rms} \rightarrow H_{high,rms}$ values.

	Peak Temperature		Performance Metrics			
	ΔT_{ad}	Δs_{max}	$\Delta T_{ad,max}$	Δs_{max}	$FWHM_s$	RCPs
Name	(K)	(K)	(K)	(J/kgK)	(K)	(J/kg)
M1	297.1	294.2	0.39	1.7	8.8	15.4
M2	295.4	293.6	0.72	3.2	8.5	27.4
M3	294.2	291.6	0.63	2.3	10.9	25.0
M4	286.2	284.3	0.94	5.6	3.9	21.9
M5	285.2	283.8	1.0	5.8	3.7	21.3

Besides spacing, the properties of individual materials also vary as shown in Fig. 4.2 and Table 4.4. The latter lists peak adiabatic temperature change, peak entropy change and calculated relative cooling potential (RCP) assuming a 0.3 to 1 T field change. RCP is calculated using Eq. 4.4

$$RCP(s) = -\Delta s_{max} \cdot FWHM_s \tag{4.4}$$

where Δs_{max} is the maximum value of the entropy change and $FWHM_s$ is the full width half maximum of the Δs curve. Niknia et al. found a linear correlation of maximum exergetic cooling power with RCP for a single material AMR [110].

The cases of R1-R5 include M1 as the warm layer; compared to the other materials, except for FWHM, the properties of M1 are significantly lower. M4 and M5 are very similar in terms of the magnitude and shapes of adiabatic temperature change, entropy change, and RCP. Thus, differences in performance for R4 and R5 seen in Fig. 4.5 and Fig. 4.6 are expected to be due to Curie spacing. Comparing R2 and R6, even though the individual material performance metrics are high in R6, it does not outperform the temperature span or exergetic cooling power of the closely spaced materials in R2.

A number of issues in the data make it difficult to draw strong conclusions. All points are taken stepping the temperature down, from an initial set hot side temperature for that day; therefore, the transient dynamic effects are working against the cooling power of the regenerator. Therefore, the temperature span reported in the results section represent a worst case scenario for these materials. Additionally, using this protocol is also more indicative of the functioning of a real refrigerator, where the temperature span has to be build from a point started at room temperature. One consideration not addressed here is a recently identified phenomena of multiple stable points of equilibrium. Hysteresis in temperature span is observed in AMRs comprised of FOM's due to intrinsic stability issues due to varying material properties [111]. These multiple stable points of equilibrium tend to arise when comparing cooling and heating protocols results. Besides ambient temperature variations and device transients, stable operating points may be a factor in the discontinuities in measured temperature span seen in Fig. 4.5. The limited range of materials available for testing results in a gap between Curie spacing for results in Fig. 4.8. This, too, limits the conclusions that can be drawn regarding correlations with Curie spacing. Furthermore, measured exergetic cooling power may not represent maximum values due to a limited number of applied loads being tested. For example, in the case of R2 and R3, higher exergetic cooling power might have been found if higher net applied load was tested. Some of these issues are being addressed using a detailed transient model of the AMRs and are the subject of a future paper.

4.6 Conclusion

A study is designed to show the impact of varying Curie spacing between two layers of Mn-Fe-Si-P materials. Five different materials are selected and combined in different regenerators. The material properties are analysed and performance metrics for each material are computed.

Some general trends emerged from the data that when the Curie spacing is decreased, the maximum temperature span and gross exergetic cooling power is increased. This closer spacing improves the emergent behaviour of the regenerator. Using Mn-Fe-Si-P type materials when a spacing in excess of 10 K is used, the beds seem to function independently of each other. This is shown by having two different distinct operating ranges around the active range of the materials used.

Individual performance of the materials is a key factor that should also be studied. The RCP(s) is linearly correlated with the maximum exergetic cooling power of a single material in AMR [110]. If two materials with a high RCP(s) would be combined we would expect them to outperform materials with a lower RCP(s). However, when two well performing materials are combined in the R6 regenerator ($RCP(s)_{M2,M4} = 27.4, 21.9$), a lower temperature span and exergetic cooling power is found than in the R2 regenerator which combines the M2 material with the low performance M1 material ($RCP(s)_{M1,M2} = 15.4, 27.4$). The sum of RCP(s) times the regenerator mass for the R6 is 7% higher than the R2, while the maximum exergetic cooling power is 21% higher for the R2. Therefore, close Curie spacing (2.3K) of weaker materials (M1,M2) can outperform further Curie spaced (9.8K) higher performing materials (M2,M4).

Chapter 5

Silicon modeling

A manuscript is being prepared from the content of this Chapter.

5.1 Abstract

The use of novel material systems for magnetic heat pump applications requires a full understanding of integrating material properties, regenerator structure and system losses. In this work, material data of Mn-Fe-Si-P is integrated into a system model approach. A framework is proposed to take into account the hysteresis found in the material data. The inclusion of this framework improves the simulation outcomes when compared to experimental results of a single layer. Multi-layering simulation results are compared to a set of experimental results. It was found that the experimental pressure drop improves the temperature span results on the use of a fixed correlation for pressure drop. A further improvement of the simulation results was found by varying the interstitial heat transfer coefficient. This indicates that the beds used degrade during handling, and accurate pressure drop and interstitial heat transfer correlations are needed to improve modeling further. At lower rejection temperatures, with far spacing, we find multiple points of equilibrium, and the model is not able to capture the details.

5.2 Introduction

The modeling of first order transition materials in layered configurations is an important step to developing cost effective magneto caloric heat pumps. Novel first order materials are potentially less expensive than rare-earth second order magnetocaloric materials. However, due to the narrow temperature region of useful a magnetocaloric effect (MCE), layering the materials is essential.

Several studies have looked into the numerical evaluation of first order materials in a layered structure.

Jacobs studies La(Fe,Si)H materials in a five layer configuration [44]. The material data is obtained from a single sample and shifted according to its transition temperature to represent the other materials in the layer. Hysteresis is not implemented in the study. Jacobs shows how to use an optimization function to determine the maximum cooling power by changing the Curie temperature of the layers, cycle frequency, flow rate and hot reservoir temperature for a fixed bed length, temperature span and field properties. For an optimized configuration, the Curie spacing between the materials is approximately 3 K. The impact on cooling power due to Curie temperature variation, flow imbalance, dead volume and off phase flow and magnet are determined using the same model.

Lei et al. studies La(Fe,Mn,Si)H materials in a layered structure [36]. Material properties are obtained from a single material and are shifted according to the transition temperature. Hysteresis is not implemented in the study. The materials are layered according to their transition temperature along a linear temperature distribution from hot to cold temperatures. The impact on performance of number of layers, rejection temperature and Curie temperature variation is analysed.

Kamran et al. build a 3D parallel plate regenerator model in FLUET to model second order and first order transition materials [46]. The first order transition La based material data is obtained by using a polynomial fit of adiabatic temperature change, while other properties are assumed constant. The model is used to validate previously obtained experimental data of layering first order transition materials [28, 31]. Modeling results predict the temperature span of the experiments within 25%. Further performance investigation of layering FOM is performed by looking at the number of layers, Curie spacing and utilization of the AMR.

Zhang et al. modeled a 16 layer regenerator consisting of La(Fe,Mn,Si)H materials [37]. The model is initially validated using Gd. The Curie temperatures of the La materials are spaced close together between 2-3K. The material data was obtained from experimental measurements provided by the manufacturer. The layer length distribution is analyzed, by trying 137 different layering configurations, to find the optimal distribution of the materials. It was found that linear distribution of the layers is close to a determined optimal design strategy.

Navickaitė et al. studied two, five and nine layer epoxy fixed packed bed configurations of La(Fe,Mn,Si)H based materials [102]. In the two layer configuration the epoxy content of the regenerator was varied. It is found that 1, 2, 3 and 4 % epoxy did not impact the performance of the regenerator, however, the 1 % epoxy regenerator broke during experimentation. The numerical model is based on the previously developed model of Lei et al. [36]. Numerical results are found to be in good agreement with each other, when peak obtained temperature span is considered. There is a slight offset between the peak temperature span found in the model and experiments. The five and nine layer regenerators showed an experimental temperature span performance of 20.9 K.

The integration of FOM properties bring with it some challenges, especially when considering multiple FOM's. It is time consuming to obtain the correct material properties for each material used in a layering configuration. Therefore, some authors when modeling FOM's will obtain the material properties from the manufacture, or measure a single material and shift the material properties according to the desired transition temperature. Some details might be lost using this method as small variations in material properties occur when the Curie temperature is shifted for some FOM's. A recent study shows that not only the peak entropy change and adiabatic temperature change, but also the width of the entropy and adiabatic temperature change curve is of importance [45].

Another difficulty is the implementation of hysteresis. The thermal-magnetic hysteresis in the first order transition impacts the material behavior during the magnetocaloric cycle. Three frameworks have been described thus far to treat the hysteresis in magnetocaloric cycle modeling.

Brey et al. describes a framework in which the energy loss due to the magnetic hysteresis is imposed on the MCE energy term [35]. This implementation has shown to produce little impact on modeled temperature span. Also, only magnetic hysteresis is considered in this model, the hysteresis found in the specific heat measurements is neglected. For some FOM's, the measured magnetic hysteresis will be smaller than the hysteresis measured on the specific heat [53]; this suggests that using this framework might underestimate the impact of hysteresis.

The second approach is using the HC thermal pathway. Engelbrecht et al. model an AMR using a *single magnetic field change*. The material properties in this model are based on the HH thermal pathway of Mn-Fe-As-P material. Two simulations are set up, using either the HH thermal pathway or the HH shifted to fit the HC thermal pathway. The modeled temperature span using the HC fitted thermal pathway is smaller than the HH thermal pathway. The HC pathway for Mn-Fe-Si-P is in agreement with cyclic adiabatic temperature measurements [20]. These cyclic adiabatic temperature change values correspond with the adiabatic temperature change measured in a single material Brayton cycle [59, 112], suggesting that this is the reversible component of the adiabatic temperature change expected during the magnetocaloric cycling.

The last framework is the use of Preisach modeling. The Preisach model treats the first order transition as a summation of multiple two phase transitions switches. Several works have fitted Preisach modeling to the FOM's such as Mn-As [54], $Gd_5Si_2Ge_2$ [56] and Mn-Fe-As-P [113]. These studies show that they are able to recreate measured values of entropy and magnetization through the transition where hysteresis is found.

Basso et al. showed that by using a Preisach model on a single FOM, the temperature span is decreased on a magnetocaloric cycle [114]. A recent study advances this work quantifying the impact of hysteresis on the cooling power and temperature span for different rejection temperatures [115]. The integration of this method into 1D modeling would however incur large computational costs. A Preisach model would need to, stored in the memory for each AMR node. Secondly, each material would need detailed magnetization and specific heat measurements to fit the Preisach model.

We have therefore chosen to develop a new approach that uses the HC thermal pathway. The approach uses the material data obtained in Chapter 2 and allows for *continuous magnetic field change*. The new approach is integrated into the 1D system model described in Chapter 3. The multi-layering modeling outcomes using this approach are compared to the experimental results from Chapter 4.

5.3 Methods

5.3.1 Dead Volume and Casing Losses

In Chapter 3 we have outlined the methods of integrating dead volume sections and casing losses into a 1D simulation. These methods are used to take into account the dead volume sections in the silicon experiments. The casing losses in all the silicon simulations are set to the **(grad)** assumption. In Fig. 5.1 a description of the regenerator housing assembly is presented based on the experiments in Chapter 4.

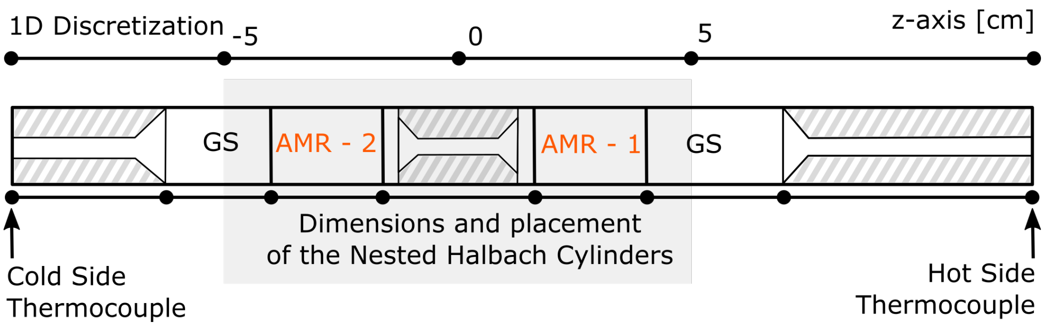

Figure 5.1: A sketch of the silicon configuration.

In Table 4.3 the materials used as regenerator 1 (AMR-1) and regenerator 2 (AMR-2) are listed. The porosity of the beds is calculate based on a material density of 6100 kg/m^3 and are found in Tab. 4.1. The lead spheres used in the R1 configuration are constructed from 23g of 300 um spheres leading to 23 mm.

5.3.2 Regenerator Closure Relationships Packed Bed

The closure relationships used in Chapter 3 are used for the lead sphere regenerator section. The thermo-hydraulic properties of the epoxy fixed crushed particulate regenerators differ from the spheres. The interstitial heat transfer coefficient used for these beds is based on the Nusselt value from Wakao et al. [79] and using the degrading factor by Engelbrecht [80].

The effective static conductivity and effective dynamic conductivity for the bed are the same correlations used as for the spheres. According to Kaviany these correlations are valid for the porosity range of the silicon beds. The effective heat transfer coefficient corrected for internal conduction [80] according to [116] provides a good approximation for these type of beds. The heat transfer from the particulate to the casing wall is assumed equal to spherical particles [79].

The pressure drop measurements of the beds are used for the viscous dissipation term. The pressure drop measured during the experiment is due to the sum of the pressure drop components analogous to a resistor network. In Eq. 5.1 the system pressure is divided into three different components.

$$\Delta p_{exp} = \Delta p_{bl} + \Delta p_{ls} + \Delta p_r \tag{5.1}$$

where Δp_{exp} is the total pressure drop in the system measured during the experiment, Δp_{bl} is the base line pressure drop of the system, Δp_{ls} is the pressure drop if the lead spheres passive regenerator and lastly, Δp_r is the pressure drop from the packed bed regenerator.

The pressure drop of the regenerator is unknown, the other two components are measured and calculated. The baseline pressure drop of the system is measured by filling the regenerator housing with glass spheres and running the device at the same operating conditions as the experiments. The baseline pressure drop for the system is measured at 2.1 ± 0.2 psi. The pressure drop in the lead spheres is calculated using Ergun's pressure drop for packed lead spheres. Slight variations in fluid temperature during the experiment produce the variation in the calculated pressure drop of lead spheres.

In Tab 5.1 the pressure drop for each of the bed experiments are listed. The value is calculated by taking the average and the maximum and minimum value for all the experimental points. The regenerator pressure drop is calculated subtracting the baseline pressure drop and, in the case of the R1 configuration, subtracting the pressure drop component of the lead spheres .

Table 5.1: The average measured experimental pressure drop and ambient temperature found at the determined steady state points. The pressure drop of the lead spheres is determined from Ergun's equation. The regenerator pressure drop is the pressure drop due to two regenerators; this value is used to correct for viscous dissipation.

	Δp (psi)				
	Δp_{exp}	Δp_{ls}	Δp_r	L_r (mm)	T_{amb} (°C)
R1	17.6 ± 3.0	10.3 ± 1.4	5.2	22.5	19.8 ± 1.3
R2	16.8 ± 9.9		14.7	45	20.3 ± 1.7
R3	25.9 ± 8.14		23.8	45	20.3 ± 1.4
R4	10.3 ± 5.1		8.2	42	20.5 ± 1.1
R5	13.3 ± 3.2		11.2	45	20.3 ± 1.5
R6	39.6 ± 7.6		37.5	42	19.5 ± 0.8

The pressure drop is changing in each experiment. It cannot be considered that the pressure on the first layer remains the same. We therefore distribute the pressure drop term across both regenerators in the simulation. The viscous dissipation term for the regenerator sections is implemented using the following equation:

$$\frac{\partial p}{\partial z} = \frac{\Delta p_r \cdot 6894.76}{2 \cdot L_{reg}} \pi f \sin(t 2 \pi f) \tag{5.2}$$

where Δp_r is the pressure drop of two regenerators in the system measured during the experiment and L_r is the total length of both regenerators in the housing assembly. The pressure drop is converted from psi to SI unit Pa using a multiplication of 6894.76 (Pa/psi).

Lastly, the ambient temperature of the lab varies with each experiment. A correction of the gross cooling power is required as stated in Chapter 3. In Tab. 5.1 the experimental values are listed. The ambient temperature for the simulations is set to the average configuration temperature listed in Tab. 5.1. Only a small variation in temperature span is expected from ± 1.5 °C variation in ambient temperature.

5.3.3 Material Properties

In Chapter 2 the magnetization and specific heat of the silicon materials is obtained for a heating and cooling direction of the material, thereby characterizing the hysteresis of the sample. The entropy of the materials is calculated from the heating and the cooling direction integrating Eq. 5.3 and Eq. 5.4.

$$ds_{he} = \left.\frac{c_{\mu_0 H}}{T}\right|_{he} dT + \left.\left(\frac{\partial M}{\partial T}\right)_{\mu_0 H}\right|_{he} d\mu_0 H_{int} \tag{5.3}$$

$$ds_{co} = \left.\frac{c_{\mu_0 H}}{T}\right|_{co} dT + \left.\left(\frac{\partial M}{\partial T}\right)_{\mu_0 H}\right|_{co} d\mu_0 H_{int} \tag{5.4}$$

A anhysteretic component of the material can be defined using Eq. 5.5.

$$s_{an}\left(\mu_0 H, T\right) = s_{he}\left(\mu_0 H, T\right) \cdot \alpha_{ch} + s_{co}\left(\mu_0 H, T\right) \cdot \left(1 - \alpha_{ch}\right) \tag{5.5}$$

The α_{ch} parameter weights the heating versus the cooling component. This results in the fact that several options are available which are listed in Tab 5.2.

Table 5.2: Material Properties Selection Parameter

α_{ch}	Operation
0	Cooling Material properties only
1	Heating Material properties only
0.5	Averaging Heating and Cooling properties

Similar, the anhysteretic magnetization per unit mass of the material are found using Eq. 5.6

$$M_{an}\left(\mu_0 H, T\right) = M_{he}\left(\mu_0 H, T\right) \cdot \alpha_{ch} + M_{co}\left(\mu_0 H, T\right) \cdot \left(1 - \alpha_{ch}\right) \tag{5.6}$$

The MCE in the numerical model is integrated using the energy production term

$$Q'_{MCE} = -\rho_r A_{rh} \left(1-\epsilon\right) \left(T_r \left[\left. \frac{\partial s_{an}}{\partial \mu_0 H} \right|_{T_r} \frac{\partial \mu_0 H}{\partial t} \right] \right) \tag{5.7}$$

with the specific heat found from the anhysteretic component of the entropy curve.

$$c_H = T_r \left(\left| \frac{\partial s_{an}}{\partial T} \right| \right)_{\mu_0 H} \tag{5.8}$$

In Fig. 5.2 the adiabatic temperature of the M1 silicon material is calculated based on four thermal paths: The heating low field to heating high field (HH), the cooling low field to cooling high field (CC), the heating low field to cooling high field (HC), and based on the low field to high field anhysteretic entropy curves (AVE). The HH and CC thermal paths represent the adiabatic temperature change if only heating data or cooling data are selected, respectively. The AVE is the result of the average of the heating and cooling data.

The HC curve is considered the reversible component of the material during the magnetocaloric cycle. Therefore, the AVE thermal path is reduced with a reduction factor, η_m, to match the HC thermal path. For the AVE to match the HC curve the AVE thermal path needs to be reduced with η_m=0.55.

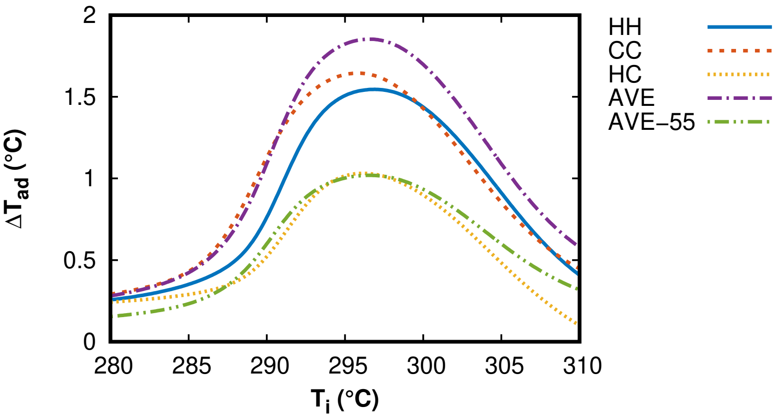

Figure 5.2: The calculated adiabatic temperature based on the thermal paths; heating low field to heating high field (HH), the cooling low field to cooling high field (CC), the heating low field to cooling high field (HC), the anhysteretic entropy curves (AVE) and the anhysteretic curve reduced with 0.55 (AVE-55).

In the simulation the reduction factor is integrated in the MCE term using Eq. 5.9.

$$Q'_{MCE,m} = Q'_{MCE} \cdot \eta_m \tag{5.9}$$

5.3.4 Multiple Points of Equilibrium

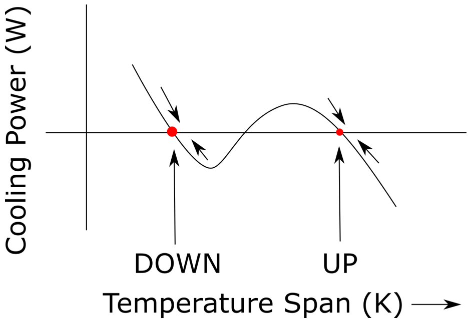

Figure 5.3: Schematic of the interpolation function.

Multiple points of equilibrium (MPE) show up in systems with significant heat leak losses and using materials with sharp changing material properties [111]. These MPE cause two stable operating points at a single cooling power and hot side temperature setting. Fig. 5.3 shows the cooling power curve versus temperature span at a single hot side temperature. When the cooling power is positive the temperature span increases. Whereas, when the cooling power is negative the temperature span decreases.

The UP steady state point is the steady state point found starting from the high temperature span. The DOWN steady state point is the steady state point starting from zero temperature span. From the work of Niknia et al., it is shown that experimental points can be forced into one position by the experimental method.

When the cold heat exchanger is first cooled below the UP steady state point, the experiment will settle at this UP steady state point. The DOWN steady state point is found when the cold heat exchanger is brought up to the temperature of the hot heat exchanger. The temperature span will then develop to settle at the

DOWN steady state point. The experiments in Chapter 4 are performed using the latter experimental method; therefore, the DOWN steady state points are found in the experiments. An interpolation function is written to find the UP and DOWN points from the simulation data [1].

5.4 Single Layer Results

In the single layer results we explain the impact of material data on the simulation outcomes. No multiple points of equilibrium are found for the single layer results for the zero and 2 W cooling curves. In Fig. 5.4 the temperature span results for α_{ch}=0 and 1 are given. These results correspond to using only the cooling or heating material data respectively.

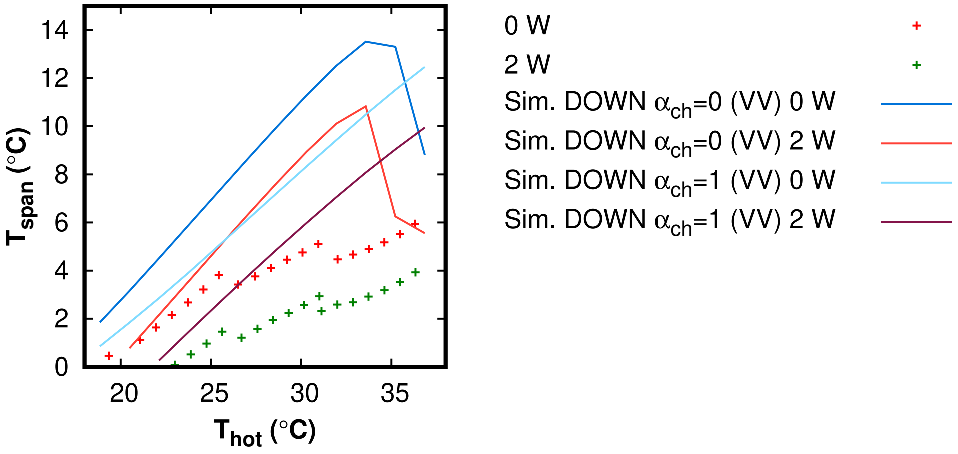

Figure 5.4: The temperature span modeling the regenerator with dead volume sections. Using $\alpha_{ch} = 0$ and $\alpha_{ch} = 1$.

Both the heating and cooling material data result in an over-prediction of the temperature span results. The cooling data is shifted left of the heating data, as is to be expected. The spread between the heating and cooling data is much larger than the hysteresis measured in the material. The shift between cooling and heating

---

[1] `https://github.com/TheoChristiaanse/AMRmodel/tree/master/MPE`

the zero watt cooling curve is at some points five degrees Celsius. At lower rejection temperatures, the heating data provides the closest results to the experimental data. However, when going to higher rejection temperatures they move away from the experimental data points.

In Fig. 5.5 the results for α_{ch}=0.5 are plotted. These are the simulation results obtained using the average of heating and cooling material data. Similar to the heating and cooling data the temperature span results over-predict the experimental result at higher rejection temperatures. At lower rejection temperatures, the results approach the experimental results.

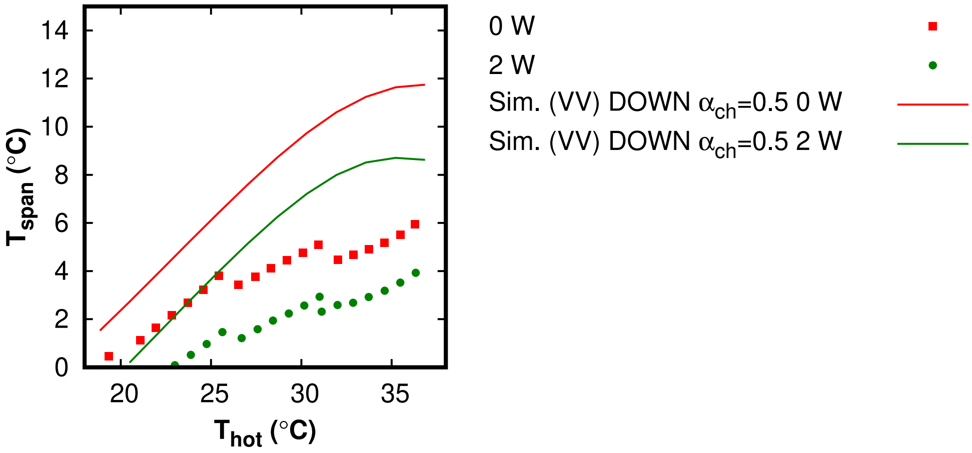

Figure 5.5: The temperature span modeling the regenerator with dead volume sections. Using $\alpha_{ch} = 0.5$.

If we consider that for the HC curve to represent the reversible component of the silicon material, a reduction factor, η_m, is introduced to reduce the AVE thermal path to the HC thermal path. In the case of the M1 material this reduction factor is 0.55 of the AVE curve. In Fig. 5.6 the results of the simulation including reduction factor are presented. Indeed a lower temperature span is obtained for the R1 configuration. The reduced curve provides a better fit of the experimental data than using the averaged values. The improvement is most substantial at the higher rejection temperatures.

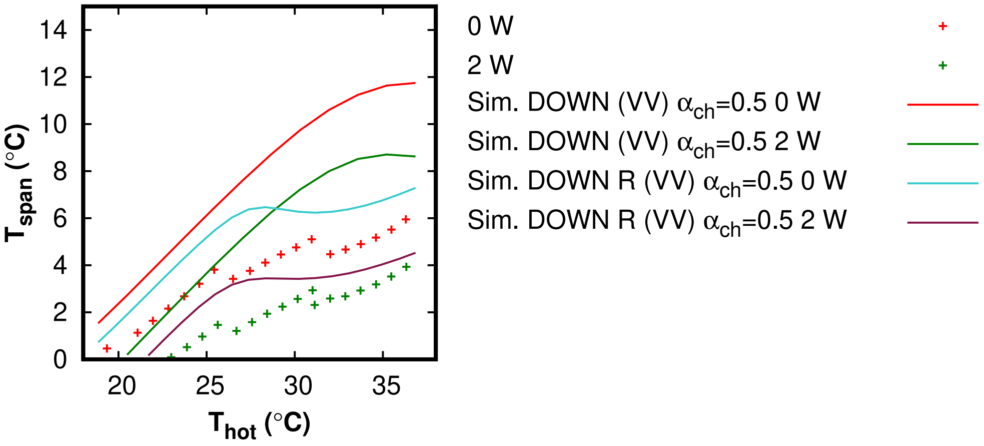

Figure 5.6: Temperature span modeling results of the regenerator with dead volume sections. Using $\alpha_{ch} = 0.5$ with and without (R) reduced Q_{MCE}.

For the single layer, the results of the simulation of the reduced curve with averaged material data properties yields the best results of the simulations ran.

5.5 Multi Layer Results

Since the reduction factor yielded the best results we modeled the layering configurations using this method. In Tab. 5.3 we have listed the reduction factors for each material. The temperature span results of the modeling are found in Fig. 5.7.

Table 5.3: Set of reduction factors extracted for each material used in the multilayering experiments.

Material	η_m
M1	0.55
M2	0.77
M3	0.73
M4	0.75
M5	0.72

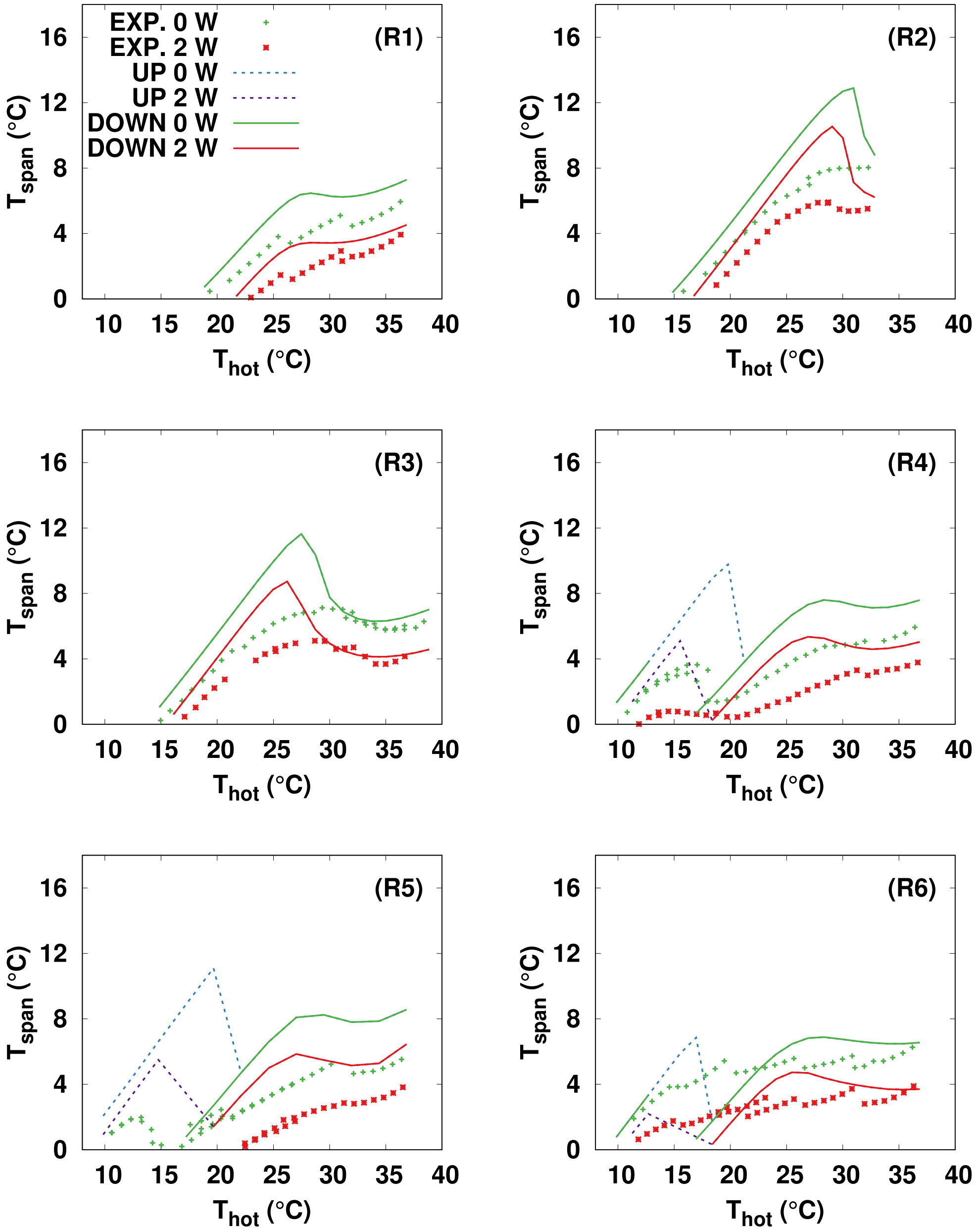

Figure 5.7: The temperature span modeling results for DOWN and UP points for the layering study in Chapter 4

In the R1 we found good matching results with the experimental results. The 2 W curve of the model and experimental results match well. For the zero Watt curve we found that there is a over-prediction of 2.8 °C on the experimental temperature span. The region in which the modeling results over-predict the experimental results matches with the high end of the active region of the M1 material. Looking at R2 and R3, this trend is continued. The R2 and R3 modeling results match the experimental results closely. However, is over-predicting the higher end of the active region of the M2 and M3 materials.

In configurations R4-5-6 we find MPE at the lower end of the rejection temperatures. This is where the M4-M5 materials are. These materials have much steeper material property changes than the M1-2-3 materials. These sharp changing material properties have shown to produce these MPE [111]. In Fig. 5.7 for most of the lower rejection temperatures only the UP points are displayed because the DOWN points result in a negative temperature span. The model is also not able to Chapter the details at these lower rejection temperatures. The experimental result is found between the UP and DOWN temperature span points found by the model. In the R4 and R6 case we found that the zero Watt UP temperature span curve beyond the transition temperature of the M4 material meets up again with the DOWN temperature span curve.

5.6 Discussion

An issue with shifting the material's properties, when it comes to the material samples we have measured, is that there seems to be a large variation in material properties even for small changes in transition temperature [20]. Therefore, each material was measured for its magnetization and specific heat properties. The integration of the material properties was achieved by using average properties for specific heat and magnetization while decreasing the MCE energy term to coincide with the HC thermal path. This is successfully applied to the regenerator composed of the M1 material and good matching results are found for the 2 W net applied cooling power temperature span curve. The zero Watt results, however, over-predict the experimental results at the high end of the active region of the material. The zero Watt curve is more susceptible to casing heat leaks than the 2 W curves.

We found that in the R1-2-3 configurations the MPE are avoided in the simulation; however, in the R4-5-6 we found MPE in the lower layer of the regenerator, all of which use the M4-5 materials. These materials have a sharp narrow peak compared to the M1-2-3 materials. This narrow peak has been shown to produce these MPE in the measurements.

Since we did cooling curve experiments, we do not expect to find UP steady state points in the experiments. The modeling results point out that at lower rejection temperatures MPE might exist for R4-R5-R6 configuration. These simulation results show that MPE are able to exist in layering configurations. This is to be avoided. R1-2-3 indicate that these materials with the closer Curie temperature spacing result do not encounter these MPE. Close spacing might be a solution for these MPE in some systems and these results could be explored further.

The heat leak system model is validated around room temperature. The model shows good trend in around these room temperature conditions. However, at lower rejection temperatures below 20 °C the predictions of the model move away from the experimental results. This indicates that the heat leak model should be revised for these lower rejection temperatures. A 2D conduction model of the outer system components could be implemented to improve the heat leaks through the casing. To validate the model in this region of lower rejection temperatures, experiments could be performed with a SOM that has a lower Curie temperature.

Through the different bed configurations and experiments we found a large variation in pressure drop. The pressure drop is changing in the beds. When the R6 beds are tested, the M2 and M4 material beds are used. These beds are reused from R2 and R4 configurations and show a the highest pressure drop. This indicates that the beds degrade during the experimentation, in storage, assembly and disassembly. The pressure drop in the experiments increases as the beds are used more. This degradation process could cause channeling of the fluid through matrix structure impacting the heat transfer and effective conduction properties of the material. A post calculation of the weight of bed showed that on average 1 g of material is lost during experimentation of each bed.

The implementation of the experimental pressure drop provided an improvement in the trend. In Fig. 5.8 we have plotted the simulation results using the experimental pressure drop and using a modified version of Ergun's equation. Lei et al. measured that similar packed beds, based on irregular particles, produce a pressure drop 2.8x higher than expected using Ergun's equation at equivalent porosity. In the R1 bed we found that in comparison between 2.8x Ergun's and experimental pressure drop, little variation is found. However, in the R3 configuration for example, there is an improvement in the trend. This indicates that the pressure drop in the M3 material is much higher than in M1 beds or that the M1 beds have started degrading in such a way that the pressure drop is increasing.

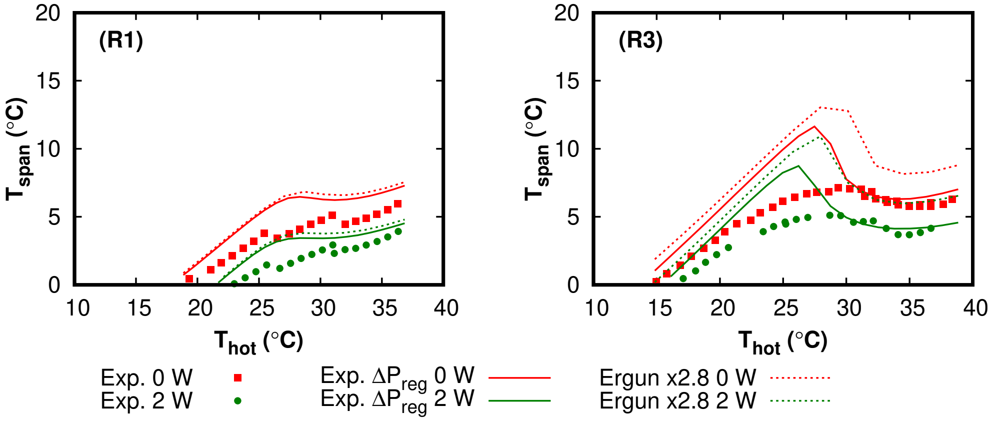

Figure 5.8: A comparison between using a modified version of Ergun's equation for the pressure drop or the experimental pressure drop to determine the viscous dissipation term.

To analyze the structure in further detail a scanning electron microscope is used to find close up images of the regenerator.

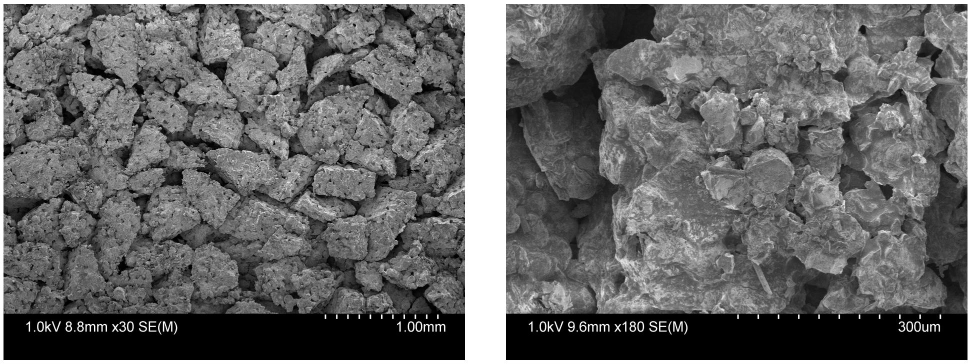

(a) Image taken of the internal region of the regenerator.

(b) Close up of a single particle in the regenerator

Figure 5.9: SEM images taken from the packed bed regenerators.

The SEM images in Fig. 5.9 (a), show that the particles are closely packed but are themselves quite porous. The close up image of a single particle in Fig. 5.9 (b) shows the crystalline structures of the silicon material but also gaps within the particle. Using the porosity of the regenerator, Ergun's equation results in a pressure drop which is a third of the measured pressure drop for the R1 configuration. The high porosity and high pressure drop compared to spheres could be due to the close packing of the rough porous particulate seen in Fig. 5.9 (a). The high porosity is due to the porous irregular shaped particles, and the high pressure drop is due to a smaller than expected flow channel.

The degradation of the beds might result in impacting the effective heat transfer or the available surface area per unit volume. A set of simulations is done where the interstitial heat transfer coefficient is multiplied by 50 %. A comparison between the results is shown in Fig. 5.10.

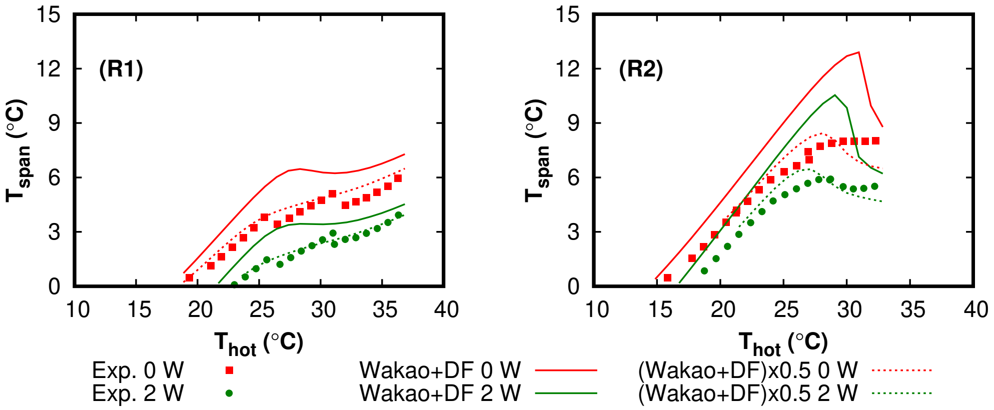

Figure 5.10: A comparison between using the relationship of using in chapter 3 and reducing the effective interstitial heat transfer coefficient with 50 %.

The results in Fig. 5.10 show that the higher temperature span around the active region of the material is lowered. In future research, the characterization of the bed structure closure relationships is important.

These packed structures are cheap to produce compared to other structures; however, they seem to have issues with breaking down and varying thermo-hydraulic properties [116]. Improvements have been made in the past by varying epoxy content, and the beds are stable, in so far no large particulate is found in the device after use. Mn-Fe-Si-P volume change due to the phase change results in additional strain in the packed bed. A rigorous analysis is required to determine the passive characteristics of these regenerator structures over a longer use period. By using passive characterization, the static conduction, pressure drop term, interstitial heat transfer and wall heat transfer coefficient can be derived under use case conditions [14].

5.7 Conclusion

Layering experimental results are modeled using a 1D system model approach. An integration of material properties is proposed that allows for continuous changing magnetic field properties. In the single layer regenerator results, this method yields significantly improved trends over the use of average material properties.

In the discussion the impact of using a fixed pressure drop correlation and the experimental pressure drop is compared. For the R1 configuration, there is little variation between the determined temperature span results. For the R3 configuration, we see a large drop in performance when using the experimental pressure drop. This indicates that the beds might be degrading inducing a higher pressure drop than expected.

To explore this point further the interstitial heat transfer coefficient is modeled using Wakao corrected with the degrading factor, and a 50 % reduced version of the same correlation. When using the original correlations, we found for R1 and R2 that the temperature span is over-predicted around the active region of the materials. Reducing the interstitial heat transfer coefficient improve the simulation results providing a better match for R1-2-3, between experimental and simulation results. Due to limited time, we are unable to present the results further however, these will be included in a future publication. However, at lower rejection temperatures, the details of the experiments are not captured in the simulation. In the R3-4-5 we also encounter multiple points of equilibrium. The experimental points fall between UP and DOWN steady state points. This is due to a combination of sharp changing material properties and heat leaks within the experimental setup. The M1-2-3 materials, which have a less sharp phase transition than the M4-5 material, avoid the MPE in this system. These modeling results show that MPE can exist in layering configurations when materials are spaced in with large transition temperature spacing. The details for these lower rejection temperatures could be either in the simulation or experimental methods. The loss model from Chapter 3 is not validated for these rejection temperatures; therefore, this could be the cause.

The modeling of the crushed particulate packed beds can be improved by accurately determining the passive characteristic of the porous matrix during real use. The degrading of the beds is suspected to be due to the cycling of the beds in the apparatus and handling of the beds outside of the experiment.

Chapter 6

Conclusion and Recommendations

6.1 Summary

In Chapter 2, six samples of a Mn-Fe-Si-P magnetocaloric material are characterized based on the specific heat and magnetization properties. The entropy diagram is constructed based on these material properties and the adiabatic temperature change is found using several different path ways. Using a toy model of the Mn-Fe-Si-P material system the sensitivities of the material data are explored to find the impact on the calculated adiabatic temperature change according to the four thermal paths. The HC thermal pathway provides an adiabatic temperature change curve, which is the closest to the cyclic temperature change measured on the sample. This cyclic temperature change is considered to be the reversible component of the Mn-Fe-Si-P during a magnetocaloric Brayton cycle [112, 59].

In Chapter 3, a 1D system model was developed specifically to analyse regenerators and the impacts of large dead volumes. The 1D model is written in Python, an open source programming language, and has been made publicly available to continue development. Two casing loss boundary condition assumptions are tested; the temperature at the outer casing is assumed to be a fixed value along the entire domain, or a temperature gradient is assumed using hot and cold fluid boundary conditions. To validate the system model, experiments are performed with Gd for rejection temperatures around room temperature. The inclusion of dead volume sections in the model shows improvement for a wide range of different regenerator configurations. The casing losses impact the zero Watt cooling power; however, they have little impact on the higher cooling power temperature span results.

Chapter 4 describes experimental results obtained using five Mn-Fe-Si-P materials in six different layering configurations. The layering configurations vary the material composition of the regenerator beds and are characterized by their transition temperature spacing. The temperature span is found for different hot side temperatures and cooling power. It is found that using materials that have close transition temperature spacing can improve the temperature span. Properly layering material properties can improve the system performance even when materials with a lower $\mathrm{RCP_s}$ are used in the combination. When the same material is combined with a higher $\mathrm{RCP_s}$ material and further transition temperature spacing, it produces a lower temperature span compared to a lower $\mathrm{RCP_s}$ material and closer spacing.

Finally in Chapter 5 a numerical study is performed with the obtained material properties, using the 1D system model comparing the modeling outcomes to the experimental results obtained. The material properties are integrated using either the heating data, cooling data, or an average of both heating and cooling data.

For the single bed configuration, the simulation based on heating, cooling, and average data, over-predict the temperature span results. A reduction factor is introduced to reduce the averaged material data to fit the results of the HC thermal pathway. This reduction factor improves the temperature span to closely match the trend of the experimentally measured results for the R1 configuration. This agrees with recent work of Govindappa et al. who use a step field change 1D simulation [117]. The modeled temperature span does still over-predict the experimental results for rejection temperatures around room temperature. For rejection temperatures below room temperature the model is not able to capture the details of the experimental data. This is likely due to the heat leak model that was only tested around room temperature. It was found that the pressure drop and interstitial heat transfer term have a large impact on the modeled trends.

6.2 Recommendations

Several factors could be improved in this work. The measured material properties in this work are a distinguishing factor among FOM modeling studies. The devices to obtain infield specific heat and magnetization data are costly and the measurements take considerable amount of time. The detailed measurements of the magnetization and specific heat add value in detailed modeling approaches. Variations in the material data are found with small changes in transition temperature. And a recent study shows the impact on performance, of varying the width of the determined entropy change and specific heat can be significant [45]. The potential of Mn-Fe-Si-P material is reduced due to the hysteresis, which can be reduced by selecting the right atomic ratios and the production method. In Fig. 6.1 lab samples are compared to samples from the pre-industrial process used in this study. As can be seen, the published lab material data has a much larger entropy change than the samples used in this study.

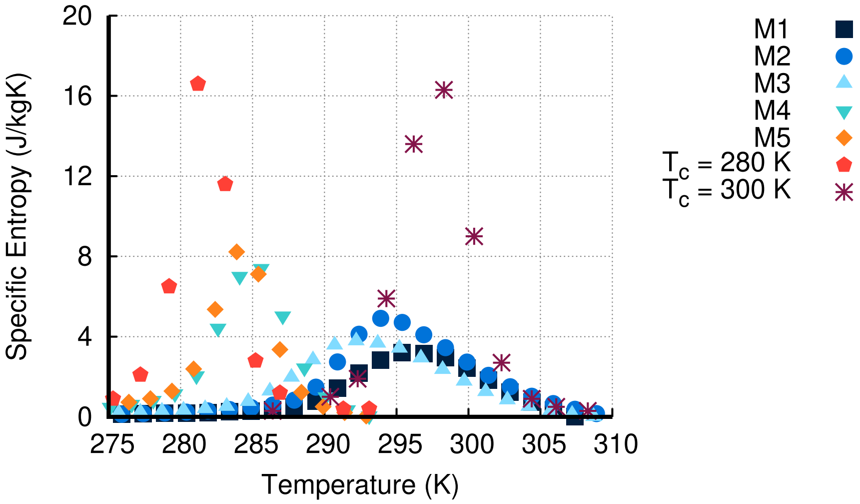

Figure 6.1: The HC entropy of the silicon materials compared to two samples published by Dung [15].

The regenerator design of these materials could also be improved. High effectiveness and low pressure drop are essential for the production of high efficiency magnetocaloric heat pumps [52]. These beds showed a high variability in pressure drop. In the R1 bed the pressure drop is 5.2 psi, while in the R6 bed the pressure drop was 37.5 psi for two regenerator layers. The difference in pressure drop could be due to improper handling of the beds.

A recent study showed that an epoxy fixed packed bed regenerator structure showed variable porosity throughout the bed and cracks in the material [118]. We also found, with the use of SEM imaging, that the materials have irregular shapes and are themselves porous. A possible solution is cold pressing the material into small tubes, which would prevent breaking of the material and increase density of the material in the regenerator [119]. These tubes could be aligned or staggered into micro structures to provide a high effectiveness and lower pressure drop. This would also prevent further degradation of the regenerator. The degradation of the regenerator has been seen in this work and in the work of [102], where beds that use a low epoxy content break after numerous cycling.

The 1D model of the PM1 system should be further developed. While the model is able to capture the details of the Gd experiments well for conditions around room temperature, the experiments with Mn-Fe-Si-P are taken at lower rejection temperatures, where the loss model is not validated. Little Mn-Fe-Si-P material was available for the experimental work leading to low cooling powers. These are susceptible to the heat leaks in the system, which make it difficult to validate the model without a rigorous analysis into these heat leaks. Experiments could aid in the validation of the model. The use of magnetocaloric material GdY, which can be found to lower Gd's transition temperature to 10 °C, could be optimal for these experiments. Similar to Gd, the GdY has a predictable second order transition that can be modeled by shifting the Gd material data [33].

The experimental method is improved to be consistent and use a protocol to determine the steady state of each point. Several data points can be taken during a single day operating the device by automatically stepping the hot side rejection temperature. During experimentation, the transient behaviour of the temperature span is monitored. This state of the device is determined by the experimental settings and the ambient lab conditions. We found that the ambient temperature in the lab varies continuously in the lab. Small variation in the ambient temperature lead to small varying temperature span during the experiments. Thus, the experiments can further be improved on by constructing a climate chamber that maintains a single ambient temperature.

6.3 Conclusion

In conclusion the use of Mn-Fe-Si-P materials can be improved by focusing on; improving the purity and density of the samples from the industrial production process. Layering has shown to improve the performance of Mn-Fe-SI-P materials in a regenerator. The regenerator structures can be improved by ensuring stable matrix structures. By shaping the materials into effective regenerator shapes, the interstitial heat transfer and pressure drop is improved. The durability is important to provide long lasting and easy to handle regenerators beds. A model which captures the loss mechanisms of the system can be used for optimization of the layered structures. We have shown that system losses can significantly impact the performance of materials in the AMR system for packed Gd spheres. The use of experimentally determined pressure drop improves the Mn-Fe-Si-P modeling outcomes. Therefore, more research is needed to determine the crushed particulate packed bed structure's thermo-hydraulic properties.

Bibliography

[1] K. J. Chua, S. K. Chou, and W. M. Yang. Advances in heat pump systems: A review. *Applied Energy*, 87(12):3611–3624, December 2010. ISSN 0306-2619. doi: 10.1016/j.apenergy.2010.06.014.

[2] I. Sarbu. A review on substitution strategy of non-ecological refrigerants from vapour compression-based refrigeration, air-conditioning and heat pump systems. *International Journal of Refrigeration*, 46:123–141, October 2014. ISSN 0140-7007. doi: 10.1016/j.ijrefrig.2014.04.023.

[3] IIR. 35th Informatory Note on Refrigeration Technologies "The impact of the refrigeration sector on climate change" - Summary for Policymakers, November 2017.

[4] V. W. Bhatkar, V. M. Kriplani, and G. K. Awari. Alternative refrigerants in vapour compression refrigeration cycle for sustainable environment: A review of recent research. *International Journal of Environmental Science and Technology*, 10(4):871–880, July 2013. ISSN 1735-1472, 1735-2630. doi: 10.1007/s13762-013-0202-7.

[5] R. Ciconkov. Refrigerants: There is still no vision for sustainable solutions. *International Journal of Refrigeration*, 86:441–448, 2018. ISSN 01407007. doi: 10.1016/j.ijrefrig.2017.12.006.

[6] X. Moya, E. Defay, V. Heine, and N. D. Mathur. Too cool to work. *Nature Physics*, 11(3):202–205, 2015.

[7] I. Takeuchi and K. Sandeman. Solid-state cooling with caloric materials. *Physics Today*, 68(12):48–54, December 2015. ISSN 0031-9228, 1945-0699. doi: 10.1063/PT.3.3022.

[8] G. V. Brown. Magnetic heat pumping near room temperature. *Journal of Applied Physics*, 47(8):3673–3680, August 1976. ISSN 0021-8979, 1089-7550. doi: 10.1063/1.323176.

[9] S. Y. Dan'kov, A. M. Tishin, V. K. Pecharsky, and K. A. Gschneidner. Magnetic phase transitions and the magnetothermal properties of gadolinium. *Physical Review B*, 57(6):3478–3490, February 1998. doi: 10.1103/PhysRevB.57.3478.

[10] J. A. Barclay and W. A. Steyert. Active Magnetic Regenerator, June 1 1982. US Patent 4,332,135.

[11] C. Zimm, A. Jastrab, A. Sternberg, V. Pecharsky, K. Gschneidner, M. Osborne, and I. Anderson. Description and Performance of a Near-Room Temperature Magnetic Refrigerator. In *Advances in Cryogenic Engineering*, Advances in Cryogenic Engineering, pages 1759–1766. Springer, 1998. doi: 10.1007/978-1-4757-9047-4_222. URL `https://link.springer.com/chapter/10.1007/978-1-4757-9047-4_222`.

[12] P. V. Trevizoli, T. V. Christiaanse, P. Govindappa, I. Niknia, R. Teyber, J. R. Barbosa, and A. Rowe. Magnetic heat pumps: An overview of design principles and challenges. *Science and Technology for the Built Environment*, 22(5):507–519, July 2016. ISSN 2374-4731, 2374-474X. doi: 10.1080/23744731.2016.1171632.

[13] A. Smith, C. R.H. Bahl, R. Bjørk, K. Engelbrecht, K. K. Nielsen, and N. Pryds. Materials Challenges for High Performance Magnetocaloric Refrigeration Devices. *Advanced Energy Materials*, 2(11):1288–1318, nov 2012. ISSN 1614-6840. doi: 10.1002/aenm.201200167.

[14] P. V. Trevizoli, A. T. Nakashima, G. F. Peixer, and J. R. Barbosa. Performance assessment of different porous matrix geometries for active magnetic regenerators. *Applied Energy*, 187:847–861, February 2017. ISSN 03062619. doi: 10.1016/j.apenergy.2016.11.031.

[15] N. H. Dung. *Moment Formation and Giant Magnetolocaloric Effects in Hexagonal Mn-Fe-P-Si Compounds*. PhD thesis, TU-Delft, 2012.

[16] J. M. D. Coey. *Magnetism and Magnetic Materials*. Cambridge University Press, 2010. ISBN 978-0-511-84500-0. doi: 10.1017/CBO9780511845000.

[17] R. Bjørk, C. R. H. Bahl, and M. Katter. Magnetocaloric properties of $\mathrm{LaFe}_{13-x-Y}\mathrm{Co}_x\mathrm{Si}_y$ and commercial grade Gd. *Journal of Magnetism and Magnetic Materials*, 322(24):3882–3888, December 2010. ISSN 03048853. doi: 10.1016/j.jmmm.2010.08.013.

[18] Yibole. *Nature of the first-order magnetic phase transition in giant-magnetocaloric materials*. PhD thesis, Technical University of Delft, Delft, 2016.

[19] N. H. Dung, L. Zhang, Z. Q. Ou, L. Zhao, L. van Eijck, A. M. Mulders, M. Avdeev, E. Suard, N. H. van Dijk, and E. Brück. High/low-moment phase transition in hexagonal Mn-Fe-P-Si compounds. *Physical Review B*, 86(4), July 2012. ISSN 1098-0121, 1550-235X. doi: 10.1103/PhysRevB.86.045134.

[20] T. V. Christiaanse, O. Campbell, P. V. Trevizoli, S. Misra, D. van Asten, L. Zhang, P. Govindappa, I. Niknia, R. Teyber, and A. Rowe. A concise approach for building the diagram for Mn–Fe–P–Si hysteretic magnetocaloric material. *Journal of Physics D: Applied Physics*, 50(36):365001, 2017. doi: https://doi.org/10.1088/1361-6463/aa7bcd.

[21] A. Kitanovski, J. Tušek, U. Tomc, U. Plaznik, M. Ožbolt, and A. Poredoš. *Magnetocaloric Energy Conversion: From Theory to Applications*. Green En-

ergy and Technology. Springer International Publishing, Cham, 2015. ISBN 978-3-319-08740-5 978-3-319-08741-2. doi: 10.1007/978-3-319-08741-2. URL `http://link.springer.com/10.1007/978-3-319-08741-2`.

[22] P. Govindappa, P. V. Trevizoli, O. Campbell, I. Niknia, T. V. Christiaanse, R. Teyber, S. Misra, M. A. Schwind, D. van Asten, L. Zhang, and A. Rowe. Experimental investigation of Mn Fe P 1-x As x multilayer active magnetic regenerators. *Journal of Physics D: Applied Physics*, 50(31):315001, August 2017. ISSN 0022-3727, 1361-6463. doi: 10.1088/1361-6463/aa7a33.

[23] G. Green, J. Chafe, J. Stevens, and J. Humphrey. A Gadolinium-Terbium Active Regenerator. In *Advances in Cryogenic Engineering*, Advances in Cryogenic Engineering, pages 1165–1174. Springer, Boston, MA, 1990. ISBN 978-1-4612-7904-4 978-1-4613-0639-9. doi: 10.1007/978-1-4613-0639-9_140. URL `https://link.springer.com/chapter/10.1007/978-1-4613-0639-9_140`.

[24] M. A. Richard, A. M. Rowe, and R. Chahine. Magnetic refrigeration: Single and multimaterial active magnetic regenerator experiments. *Journal of Applied Physics*, 95(4):2146–2150, January 2004. ISSN 0021-8979. doi: 10.1063/1.1643200.

[25] A. Rowe and A. Tura. Experimental investigation of a three-material layered active magnetic regenerator. *International Journal of Refrigeration*, 29(8):1286–1293, December 2006. ISSN 0140-7007. doi: 10.1016/j.ijrefrig.2006.07.012.

[26] D.S. Arnold, A. Tura, and A. Rowe. Experimental analysis of a two-material active magnetic regenerator. *International Journal of Refrigeration*, 34(1):178–191, January 2011. ISSN 01407007. doi: 10.1016/j.ijrefrig.2010.08.015.

[27] T. Okamura, K. Yamada, N. Hirano, and S. Nagaya. Performance of a room-temperature rotary magnetic refrigerator. *International Journal of Refrigeration*, 29(8):1327–1331, December 2006. ISSN 01407007. doi: 10.1016/j.ijrefrig.2006.07.020.

[28] U. Legait, F. Guillou, A. Kedous-Lebouc, V. Hardy, and M. Almanza. An experimental comparison of four magnetocaloric regenerators using three different materials. *International Journal of Refrigeration*, 37:147–155, January 2014. ISSN 01407007. doi: 10.1016/j.ijrefrig.2013.07.006.

[29] Y. Chiba, O. Sari, A. Smaïli, C. Mahmed, and P. Nikkola. Experimental Study of a Multilayer Active Magnetic Regenerator Refrigerator-Demonstrator. In Ibrahim Dincer, C. Ozgur Colpan, Onder Kizilkan, and M. Akif Ezan, editors, *Progress in Clean Energy, Volume 1*, pages 225–233. Springer International Publishing, Cham, 2015. ISBN 978-3-319-16708-4 978-3-319-16709-1. doi: 10.1007/978-3-319-16709-1_16. URL `http://link.springer.com/10.1007/978-3-319-16709-1_16`.

[30] B. Pulko, J. Tušek, J. D. Moore, B. Weise, K. Skokov, O. Mityashkin, A. Kitanovski, C. Favero, P. Fajfar, O. Gutfleisch, A. Waske, and A. Poredoš. Epoxy-bonded La–Fe–Co–Si magnetocaloric plates. *Journal of Magnetism and Magnetic Materials*, 375:65–73, February 2015. ISSN 03048853. doi: 10.1016/j.jmmm.2014.08.074.

[31] J. Tušek, A. Kitanovski, U. Tomc, C. Favero, and A. Poredoš. Experimental comparison of multi-layered La–Fe–Co–Si and single-layered Gd active magnetic regenerators for use in a room-temperature magnetic refrigerator. *International Journal of Refrigeration*, 37:117–126, January 2014. ISSN 0140-7007. doi: 10.1016/j.ijrefrig.2013.09.003.

[32] P. V. Trevizoli, A. T. Nakashima, and J. R. Barbosa. Performance evaluation of an active magnetic regenerator for cooling applications – part II: Mathematical modeling and thermal losses. *International Journal of Refrigeration*, 72:206–217, December 2016. ISSN 0140-7007. doi: 10.1016/j.ijrefrig.2016.07.010.

[33] R. Teyber, P.V. Trevizoli, T.V. Christiaanse, P. Govindappa, I. Niknia, and A. Rowe. Performance evaluation of two-layer active magnetic regenerators with

second-order magnetocaloric materials. *Applied Thermal Engineering*, 106:405–414, August 2016. ISSN 13594311. doi: 10.1016/j.applthermaleng.2016.06.029.

[34] I. Niknia, O. Campbell, T.V. Christiaanse, P. Govindappa, R. Teyber, P.V. Trevizoli, and A. Rowe. Impacts of configuration losses on active magnetic regenerator device performance. *Applied Thermal Engineering*, 106:601–612, August 2016. ISSN 13594311. doi: 10.1016/j.applthermaleng.2016.06.039.

[35] W. Brey, G. Nellis, and S. Klein. Thermodynamic modeling of magnetic hysteresis in AMRR cycles. *International Journal of Refrigeration*, 47:85–97, 2014. ISSN 0140-7007. doi: 10.1016/j.ijrefrig.2014.07.013.

[36] T. Lei, K. K. Nielsen, K. Engelbrecht, C. R. H. Bahl, H. N. Bez, and C. T. Veje. Sensitivity study of multi-layer active magnetic regenerators using first order magnetocaloric material La(Fe,Mn,Si) $_{13}$ H $_{y}$. *Journal of Applied Physics*, 118(1):014903, 2015. ISSN 0021-8979, 1089-7550. doi: 10.1063/1.4923356.

[37] M. Zhang, O. Abdelaziz, A. M. Momen, and A. Abu-Heiba. A numerical analysis of a magnetocaloric refrigerator with a 16-layer regenerator. *Scientific Reports*, 7(1), 2017. ISSN 2045-2322. doi: 10.1038/s41598-017-14406-9.

[38] C. Aprea, A. Greco, and A. Maiorino. A numerical analysis of an active magnetic regenerative refrigerant system with a multi-layer regenerator. *Energy Conversion and Management*, 52(1):97–107, 2011. ISSN 01968904. doi: 10.1016/j.enconman.2010.06.048.

[39] T. Burdyny and A. Rowe. Simplified modeling of active magnetic regenerators. *International Journal of Refrigeration*, 36(3):932–940, May 2013. ISSN 0140-7007. doi: 10.1016/j.ijrefrig.2012.10.022.

[40] C. M. Hsieh, Y. C. Su, C. H. Lee, P. H. Cheng, and K. C. Leou. Modeling of Graded Active Magnetic Regenerator for Room-Temperature, Energy-Efficient

Refrigeration. *IEEE Transactions on Magnetics*, 50(1):1–4, January 2014. ISSN 0018-9464. doi: 10.1109/TMAG.2013.2274097.

[41] B. Monfared and B. Palm. Optimization of layered regenerator of a magnetic refrigeration device. *International Journal of Refrigeration*, 57:103–111, 2015. ISSN 01407007. doi: 10.1016/j.ijrefrig.2015.04.019.

[42] Z.C. Xu, G.X. Lin, and J.C. Chen. A GdxHo1x-based composite and its performance characteristics in a regenerative Ericsson refrigeration cycle. *Journal of Alloys and Compounds*, 639:520–525, 2015. ISSN 09258388. doi: 10.1016/j.jallcom.2015.03.147.

[43] Y. You, S. Yu, Y. Tian, X. Luo, and S. Huang. A numerical study on the unsteady heat transfer in active regenerator with multi-layer refrigerants of rotary magnetic refrigerator near room temperature. *International Journal of Refrigeration*, 65:238–249, 2016. ISSN 01407007. doi: 10.1016/j.ijrefrig.2016.02.002.

[44] S. Jacobs. Modeling and optimal design of a multilayer active magnetic refrigeration system. In *Proceedings of the 3th IIF-IIR International Conference on Magnetic Refrigeration*, pages 267–273, 2009.

[45] T. Lei, K. Engelbrecht, K. K. Nielsen, H. N. Bez, and C. R. H. Bahl. Study of multi-layer active magnetic regenerators using magnetocaloric materials with first and second order phase transition. 49(34):345001, 2016. ISSN 0022-3727, 1361-6463. doi: 10.1088/0022-3727/49/34/345001.

[46] M. S. Kamran, H. Ali, M. Farhan, Y. B. Tang, Y. G. Chen, and H. S. Wang. Performance optimisation of room temperature magnetic refrigerator with layered/multi-material microchannel regenerators. *International Journal of Refrigeration*, 68:94–106, 2016. ISSN 0140-7007. doi: 10.1016/j.ijrefrig.2016.04.013.

[47] K.K. Nielsen, J. Tusek, K. Engelbrecht, S. Schopfer, A. Kitanovski, C.R.H. Bahl, A. Smith, N. Pryds, and A. Poredos. Review on numerical modeling of active magnetic regenerators for room temperature applications. *International Journal of Refrigeration*, 34(3):603–616, 2011. ISSN 01407007. doi: 10.1016/j.ijrefrig.2010.12.026.

[48] T. F. Petersen, K. Engelbrecht, C.R.H. Bahl, B. Elmegaard, N. Pryds, and A. Smith. Comparison between a 1D and a 2D numerical model of an active magnetic regenerative refrigerator. *Journal of Physics D: Applied Physics*, 41 (10):105002, 2008.

[49] I. Mugica, S. Poncet, and J. Bouchard. 3D Direct Numerical Simulation of Magneto-Caloric regenerators. page 11, 2018.

[50] A. Rowe. Thermodynamics of active magnetic regenerators: Part I. *Cryogenics*, 52(2):111–118, 2012. ISSN 0011-2275. doi: 10.1016/j.cryogenics.2011.09.005.

[51] A. Rowe. Thermodynamics of active magnetic regenerators: Part II. *Cryogenics*, 52(2-3):119–128, 2012. ISSN 00112275. doi: 10.1016/j.cryogenics.2011.09.007.

[52] P. V. Trevizoli. *Development of Thermal Regenerators for Magnetic Cooling Applications*. Ph. D. Thesis, Federal University of Santa Catarina, Florianpolis, SC, Brazil, 2015.

[53] K. Engelbrecht, K. K. Nielsen, C. R. H. Bahl, C. P. Carroll, and D. van Asten. Material properties and modeling characteristics for MnFeP1xAsx materials for application in magnetic refrigeration. *Journal of Applied Physics*, 113(17): 173510, 2013. ISSN 0021-8979. doi: 10.1063/1.4803495.

[54] V. Basso, M. Kuepferling, C. P. Sasso, and M. LoBue. Modeling Hysteresis of First-Order Magneto-Structural Phase Transformations. *IEEE Transactions*

on Magnetics, 44(11):3177–3180, 2008. ISSN 0018-9464. doi: 10.1109/TMAG.2008.2002796.

[55] V. Basso. Basics of the magnetocaloric effect. *arXiv*, 2017. URL `http://arxiv.org/abs/1702.08347`.

[56] Lars von Moos, C. R. H. Bahl, K. Kirstein Nielsen, and Kurt Engelbrecht. The influence of hysteresis on the determination of the magnetocaloric effect in Gd5Si2Ge2. *Journal of Physics D: Applied Physics*, 48(2):025005, 2014.

[57] N. H. Dung, Z. Q. Ou, L. Caron, . Zhang, D. T. C. Thanh, G. A. de Wijs, R. A. de Groot, K. H. J. Buschow, and E. Brück. Mixed Magnetism for Refrigeration and Energy Conversion. *Advanced Energy Materials*, 1(6):1215–1219, November 2011. ISSN 16146832. doi: 10.1002/aenm.201100252.

[58] L. Caron, Z. Q. Ou, T. T. Nguyen, D. T. Cam Thanh, O. Tegus, and E. Brck. On the determination of the magnetic entropy change in materials with first-order transitions. *Journal of Magnetism and Magnetic Materials*, 321(21):3559–3566, 2009. ISSN 0304-8853. doi: 10.1016/j.jmmm.2009.06.086.

[59] F. Guillou, H. Yibole, G. Porcari, L. Zhang, N. H. van Dijk, and E. Brück. Magnetocaloric effect, cyclability and coefficient of refrigerant performance in the MnFe(P, Si, B) system. *Journal of Applied Physics*, 116(6):063903, August 2014. ISSN 0021-8979. doi: 10.1063/1.4892406.

[60] A. Tura and A. Rowe. Permanent magnet magnetic refrigerator design and experimental characterization. *International Journal of Refrigeration*, 34(3):628–639, May 2011. ISSN 01407007. doi: 10.1016/j.ijrefrig.2010.12.009.

[61] T. V. Christiaanse, P. V. Trevizoli, S. Misra, C. Carroll, D. van Asten, L. Zhang, R. Teyber, P. Govindappa, I. Niknia, and A. Rowe. Experimental Study of 2-Layer Regenerators Using Mn-Fe-Si-P Materials. *Journal of Physics D: Applied Physics*, 2018. ISSN 1361-6463. doi: 10.1088/1361-6463/aaaba7.

[62] K. A. Gschneidner and V. K. Pecharsky. Thirty years of near room temperature magnetic cooling: Where we are today and future prospects. *International Journal of Refrigeration*, 31(6):945–961, September 2008. ISSN 0140-7007. doi: 10.1016/j.ijrefrig.2008.01.004.

[63] O. Gutfleisch, T. Gottschall, M. Fries, D. Benke, I. Radulov, K. P. Skokov, H. Wende, M. Gruner, M. Acet, P. Entel, and M. Farle. Mastering hysteresis in magnetocaloric materials. *Philosophical Transactions. Series A, Mathematical, Physical, and Engineering Sciences*, 374(2074), August 2016. ISSN 1364-503X. doi: 10.1098/rsta.2015.0308.

[64] J. A. Lozano, K. Engelbrecht, C. R. H. Bahl, K. K. Nielsen, J. R. Barbosa, A. T. Prata, and N. Pryds. Experimental and numerical results of a high frequency rotating active magnetic refrigerator. *International Journal of Refrigeration*, 37:92–98, January 2014. ISSN 0140-7007. doi: 10.1016/j.ijrefrig.2013.09.002.

[65] K. K. Nielsen, H. N. Bez, L. von Moos, R. Bjørk, D. Eriksen, and C. R. H. Bahl. Direct measurements of the magnetic entropy change. *Review of Scientific Instruments*, 86(10):103903, October 2015. ISSN 0034-6748, 1089-7623. doi: 10.1063/1.4932308.

[66] V. K. Pecharsky and K. A. Gschneidner. Magnetocaloric effect from indirect measurements: Magnetization and heat capacity. *Journal of Applied Physics*, 86(1):565–575, June 1999. ISSN 0021-8979. doi: 10.1063/1.370767.

[67] S. Jeppesen, S. Linderoth, N. Pryds, L. T. Kuhn, and J. B. Jensen. Indirect measurement of the magnetocaloric effect using a novel differential scanning calorimeter with magnetic field. *Review of Scientific Instruments*, 79(8):083901, August 2008. ISSN 0034-6748. doi: 10.1063/1.2957611.

[68] S. Foner. Versatile and Sensitive Vibrating-Sample Magnetometer. *Review of Scientific Instruments*, 30(7):548–557, July 1959. ISSN 0034-6748. doi: 10.1063/1.1716679.

[69] V. Basso, C. P. Sasso, K. P. Skokov, O. Gutfleisch, and V. V. Khovaylo. Hysteresis and magnetocaloric effect at the magnetostructural phase transition of Ni-Mn-Ga and Ni-Mn-Co-Sn Heusler alloys. *Physical Review B*, 85(1), January 2012. ISSN 1098-0121, 1550-235X. doi: 10.1103/PhysRevB.85.014430.

[70] R. I. Joseph. Ballistic Demagnetizing Factor in Uniformly Magnetized Cylinders. *Journal of Applied Physics*, 37(13):4639–4643, December 1966. ISSN 0021-8979. doi: 10.1063/1.1708110.

[71] X. F. Miao. *Magnetoelastic Coupling in Mn-Fe-P-Si Compounds*. PhD thesis, TU-Delft, Delft, 2016. URL `http://repository.tudelft.nl/islandora/object/uuid%3Ad3a25568-3dff-4d71-acf3-c302314a4670`.

[72] P. V. Trevizoli and J. R. Barbosa. Thermal-hydraulic behavior and influence of carryover losses in oscillating-flow regenerators. *International Journal of Thermal Sciences*, 113:89–99, March 2017. ISSN 1290-0729. doi: 10.1016/j.ijthermalsci.2016.11.002.

[73] I. Park, Y. Kim, and S. Jeong. Development of the tandem reciprocating magnetic regenerative refrigerator and numerical simulation for the dead volume effect. *International Journal of Refrigeration*, 36(6):1741–1749, September 2013. ISSN 0140-7007. doi: 10.1016/j.ijrefrig.2013.03.012.

[74] Y. Liu. *Dead Volume Effects in Passive Regeneration: Experimental and Numerical Characterization*. Master Thesis, University of Victoria, Victoria, BC, 2015.

[75] P.V. Trevizoli, G.F. Peixer, A.T. Nakashima, M.S. Capovilla, J.A. Lozano, and J.R. Barbosa. Influence of inlet flow maldistribution and carryover losses on the performance of thermal regenerators. *Applied Thermal Engineering*, 133:472–482, March 2018. ISSN 13594311. doi: 10.1016/j.applthermaleng.2018.01.055.

[76] K. Engelbrecht. A Numerical Model of an Active Magnetic Regenerator Refrigeration System, 2004.

[77] K.K. Nielsen, C.R.H. Bahl, A. Smith, R. Bjørk, N. Pryds, and J. Hattel. Detailed numerical modeling of a linear parallel-plate Active Magnetic Regenerator. *International Journal of Refrigeration*, 32(6):1478–1486, September 2009. ISSN 01407007. doi: 10.1016/j.ijrefrig.2009.03.003.

[78] M. Kaviany. *Principles of Heat Transfer in Porous Media*. Springer Science & Business Media, 2012.

[79] N. Wakao and S. Kagei. *Heat and Mass Transfer in Packed Beds*. Number v. 1 in Topics in chemical engineering. Gordon and Breach Science Publishers, New York, 1982. ISBN 978-0-677-05860-3.

[80] K. L. Engelbrecht, G. F. Nellis, and S. A. Klein. The Effect of Internal Temperature Gradients on Regenerator Matrix Performance. *Journal of Heat Transfer*, 128(10):1060–1069, March 2006. ISSN 0022-1481. doi: 10.1115/1.2345428.

[81] S. Ergun and A. A. Orning. Fluid Flow through Randomly Packed Columns and Fluidized Beds. *Industrial & Engineering Chemistry*, 41(6):1179–1184, June 1949. ISSN 0019-7866, 1541-5724. doi: 10.1021/ie50474a011.

[82] Scientificglass. Physical Properties of Borosilicate Glass 3.3, Accessed online; March 2018. URL `http://www.scientificglass.co.uk/contents/en-uk/d115_Physical_Properties_of_Borosilicate_Glass.html`.

[83] T. F. Petersen, N. Pryds, A. Smith, J. Hattel, H. Schmidt, and H.J.K. Høgaard. Two-dimensional mathematical model of a reciprocating room-temperature Active Magnetic Regenerator. *International Journal of Refrigeration*, 31(3):432–443, May 2008. ISSN 0140-7007. doi: 10.1016/j.ijrefrig.2007.07.009.

[84] R. Bjørk and C. R. H. Bahl. Demagnetization factor for a powder of randomly

packed spherical particles. *Applied Physics Letters*, 103(10):102403, September 2013. ISSN 0003-6951, 1077-3118. doi: 10.1063/1.4820141.

[85] D. X. Chen, J. A. Brug, and R. B. Goldfarb. Demagnetizing factors for cylinders. *IEEE Transactions on Magnetics*, 27(4):3601–3619, July 1991. ISSN 0018-9464. doi: 10.1109/20.102932.

[86] Y. Brunet and M. Renard. Heat transfer between two horizontal concentric cylinders: The outer cylinder rotating, the inner at rest. *Cryogenics*, 17(7): 423–427, July 1977. ISSN 00112275. doi: 10.1016/0011-2275(77)90291-0.

[87] M. Fénot, Y. Bertin, E. Dorignac, and G. Lalizel. A review of heat transfer between concentric rotating cylinders with or without axial flow. *International Journal of Thermal Sciences*, 50(7):1138–1155, July 2011. ISSN 12900729. doi: 10.1016/j.ijthermalsci.2011.02.013.

[88] NIST. Cryogenic material properties G-10 CR (Fiberglass Epoxy), Accessed online; March 2018. URL `http://cryogenics.nist.gov/MPropsMAY/G-10%20CR%20Fiberglass%20Epoxy/G10CRFiberglassEpoxy_rev.htm`.

[89] L.P.B.M. Janssen and M.M.C.G. Warmoeskerken. *Transport Phenomena Data Companion*. Delft Academic Press, Delft, third edition edition, 1987. ISBN 978-90-71301-59-9.

[90] T. L. Bergman, Adrienne S. Lavine, Frank P. Incropera, and David P. Dewitt, editors. *Fundamentals of Heat and Mass Transfer*. Wiley, Hoboken, NJ, 7th ed edition, 2011. ISBN 978-0-470-50197-9.

[91] Plastics international. Ultem(Polytherimide) data sheet, 2018. URL `https://www.plasticsintl.com/datasheets/ULTEM_GF30.pdf`. Accessed on 2018-03-08.

[92] T. Burdyny, D. S. Arnold, and A. Rowe. AMR thermodynamics: Semi-analytic

modeling. *Cryogenics*, 62:177–184, July 2014. ISSN 0011-2275. doi: 10.1016/j.cryogenics.2014.03.013. hello.

[93] R. Bjørk, C.R.H. Bahl, A. Smith, and N. Pryds. Review and comparison of magnet designs for magnetic refrigeration. *International Journal of Refrigeration*, 33(3):437–448, May 2010. ISSN 01407007. doi: 10.1016/j.ijrefrig.2009.12.012.

[94] J. E. Cararo, J. A. Lozano, P. V. Trevizoli, A. Rowe, and J. R. Barbosa Jr. Optimization of active magnetic regenerators with two and three layers of Gd-alloys. International Institute of Refrigeration (IIR), 2016. doi: 10.18462/iir.thermag.2016.0126.

[95] A. Rowe, A. Tura, J. Dikeos, and R. Chahine. Active Magnetic regenerator experimental optimization. In *Proceedings of the International Green Energy Conference*, Waterloo, Ontario, Canada, 2005. URL `https://www.uvic.ca/research/centres/iesvic/assets/docs/dissertations/Dissertation-Tura.pdf`.

[96] A. Rowe and A. Tura. Active magnetic regenerator performance enhancement using passive magnetic materials. *Journal of Magnetism and Magnetic Materials*, 320(7):1357–1363, April 2008. ISSN 0304-8853. doi: 10.1016/j.jmmm.2007.11.018.

[97] D. Eriksen, K. Engelbrecht, C.R.H. Bahl, R. Bjørk, K.K. Nielsen, A.R. Insinga, and N. Pryds. Design and experimental tests of a rotary active magnetic regenerator prototype. *International Journal of Refrigeration*, 58:14–21, October 2015. ISSN 01407007. doi: 10.1016/j.ijrefrig.2015.05.004.

[98] A. T. Saito and H. Nakagome. Room-temperature magnetic refrigeration: From basic research to development for application., 2016.

[99] R. Teyber, P. V. Trevizoli, T. V. Christiaanse, P. Govindappa, I. Niknia, and

A. Rowe. Semi-analytic AMR element model. *Applied Thermal Engineering*, 128:1022–1029, 2018.

[100] C. R. H. Bahl, D. Velázquez, K. K. Nielsen, K. Engelbrecht, K. B. Andersen, R. Bulatova, and N. Pryds. High performance magnetocaloric perovskites for magnetic refrigeration. *Applied Physics Letters*, 100(12):121905, March 2012. ISSN 0003-6951, 1077-3118. doi: 10.1063/1.3695338.

[101] S. Jacobs, J. Auringer, A. Boeder, J. Chell, L. Komorowski, J. Leonard, S. Russek, and C. Zimm. The performance of a large-scale rotary magnetic refrigerator. *International Journal of Refrigeration*, 37:84–91, January 2014. ISSN 01407007. doi: 10.1016/j.ijrefrig.2013.09.025.

[102] K. Navickaitė, H. N. Bez, T. Lei, A. Barcza, H. Vieyra, C. R. H. Bahl, and K. Engelbrecht. Experimental and numerical comparison of multi-layered La(Fe,Si,Mn)13Hy active magnetic regenerators. *International Journal of Refrigeration*, November 2017. ISSN 0140-7007. doi: 10.1016/j.ijrefrig.2017.10.032.

[103] K. Engelbrecht, C.R.H. Bahl, and K.K. Nielsen. Experimental results for a magnetic refrigerator using three different types of magnetocaloric material regenerators. *International Journal of Refrigeration*, 34(4):1132–1140, June 2011. ISSN 01407007. doi: 10.1016/j.ijrefrig.2010.11.014.

[104] M. Balli, O. Sari, L. Zamni, C. Mahmed, and J. Forchelet. Implementation of La(Fe, Co)13-xSix materials in magnetic refrigerators: Practical aspects. *Materials Science and Engineering: B*, 177(8):629–634, May 2012. ISSN 09215107. doi: 10.1016/j.mseb.2012.03.016.

[105] J. Cheng, G. Liu, J. Huang, C. Liu, P. Jin, and H. Yan. Refrigeration effect of La(FeCoSi)13B0.25 compounds and gadolinium metal in reciprocating magnetic refrigerator. *Journal of Rare Earths*, 31(12):1163–1167, December 2013. ISSN 10020721. doi: 10.1016/S1002-0721(12)60421-9.

[106] N. Hirano, Y. Miyazaki, S. Bae, H. Takata, T. Kawanami, F. Xiao, T. Okamura, and H. Wada. Development of room temperature magnetic heat pump technologies as a national project in japan. In *Proceedings of the 6th IIF-IIR International Conference on Magnetic Refrigeration*, Victoria, BC, September 2014.

[107] C. Zimm, A. Boeder, J. Chell, A. Sternberg, A. Fujita, S. Fujieda, and K. Fukamichi. Design and performance of a permanent-magnet rotary refrigerator. *International Journal of Refrigeration*, 29(8):1302–1306, December 2006. ISSN 0140-7007. doi: 10.1016/j.ijrefrig.2006.07.014.

[108] P. V. Trevizoli, J. A. Lozano, G. F. Peixer, and J. R. Barbosa Jr. Design of nested Halbach cylinder arrays for magnetic refrigeration applications. *Journal of Magnetism and Magnetic Materials*, 395:109–122, December 2015. ISSN 03048853. doi: 10.1016/j.jmmm.2015.07.023.

[109] B. Bleaney and R. A. Hull. The effective susceptibility of a paramagnetic powder. *Proc. R. Soc. Lond. A*, 178(972):86–92, May 1941. ISSN 0080-4630, 2053-9169. doi: 10.1098/rspa.1941.0045.

[110] I. Niknia, P. V. Trevizoli, T. V. Christiaanse, P. Govindappa, R. Teyber, and A. Rowe. Material screening metrics and optimal performance of an active magnetic regenerator. *Journal of Applied Physics*, 121(6):064902, February 2017. ISSN 0021-8979. doi: 10.1063/1.4975833.

[111] I. Niknia, P. V. Trevizoli, P. Govindappa, T. V. Christiaanse, R. Teyber, and A. Rowe. Multiple points of equilibrium for active magnetic regenerators using first order magnetocaloric material. *Journal of Applied Physics*, 123(20):204901, 2018. ISSN 0021-8979, 1089-7550. doi: 10.1063/1.5026633.

[112] F. Guillou, G. Porcari, H. Yibole, N. van Dijk, and E. Brück. Taming the First-Order Transition in Giant Magnetocaloric Materials. *Advanced Materials*, 26(17):2671–2675, 2014. ISSN 1521-4095. doi: 10.1002/adma.201304788.

[113] L. von Moos, C. R. H. Bahl, K. K. Nielsen, K. Engelbrecht, M. Kpferling, and V. Basso. A Preisach approach to modeling partial phase transitions in the first order magnetocaloric material MnFe(P,As). *Physica B: Condensed Matter*, 435: 144–147, 2014. ISSN 0921-4526. doi: 10.1016/j.physb.2013.09.054.

[114] V. Basso, C. P. Sasso, G. Bertotti, and M. LoBue. Effect of material hysteresis in magnetic refrigeration cycles. *International Journal of Refrigeration*, 29(8): 1358–1365, 2006. ISSN 0140-7007. doi: 10.1016/j.ijrefrig.2006.08.001.

[115] T. D. Brown, T. Buffington, and P. J. Shamberger. Effects of hysteresis and Brayton cycle constraints on magnetocaloric refrigerant performance. *Journal of Applied Physics*, 123(18):185101, 2018. ISSN 0021-8979, 1089-7550. doi: 10.1063/1.5022467.

[116] T. Lei, K. Navickaitė, K. Engelbrecht, A. Barcza, H. Vieyra, K. K. Nielsen, and C. R.H. Bahl. Passive characterization and active testing of epoxy bonded regenerators for room temperature magnetic refrigeration. *Applied Thermal Engineering*, 128:10–19, January 2018. ISSN 13594311. doi: 10.1016/j.applthermaleng.2017.08.152.

[117] P. Govindappa. *Active magnetic regenerator cycles: impact of hysteresis in* $MnFeP_{1-x}(As/Si)_x$. Ph.D. dissertation, University of Victoria, Victoria, BC, Canada, 2018.

[118] A. Funk, M. Zeilinger, A. Miehe, D. Sopu, J. Eckert, Fl. Dötz, and A. Waske. MnFePSi-based magnetocaloric packed bed regenerators: Structural details probed by X-ray tomography. *Chemical Engineering Science*, 175:84–90, January 2018. ISSN 0009-2509. doi: 10.1016/j.ces.2017.09.030.

[119] A. Funk, J. Freudenberger, A. Waske, and M. Krautz. Getting magnetocaloric materials into good shape: Cold-working of La(Fe, Co, Si)13 by powder-in-tube-processing. *Materials Today Energy*, 9:223–228, 2018. ISSN 2468-6069. doi: 10.1016/j.mtener.2018.05.009.

[120] N. Bez H., K. Navickaite, T. Lei, K. Engelbrecht, Barcza A., and Bahl C. R. H. Epoxy-bonded La(Fe,Mn,Si)13Hz as a multilayered active magnetic regenerator. International Institute of Refrigeration (IIR), 2016.

[121] S. V. Patankar. *Numerical Heat Transfer and Fluid Flow.* Series in computational methods in mechanics and thermal sciences. Hemisphere Publ. Co, 1980. ISBN 978-0-89116-522-4. OCLC: 31743097.

Appendix A

Experimental Literature Table

A literature review of the experimental layering studies is done before the experimental study of the FOM's. Type of materials, number of layers, Curie temperature spacing, and performance are highlighted. In Tab. A.1 experimental data of layering experiments based on chronological order, grouped by second and first order materials are shown. Several layering experiments might have been performed in the reference but listed are the results from the best performing layering. The material system and Curie temperatures are listed as reported in the paper. The transition temperature of the materials is based on the reported Curie temperature, or based on the adiabatic temperature peak temperature (indicated by ΔT). The number of beds and mass of each bed is listed. The weight is based on an average weight between all regenerators constructed. The applied field of the apparatus greatly influences the performance, therefore it is listed. The maximum temperature span (T_{span}) is reported for this layering and if zero span cooling power (Q_c) is reported this is also listed. The materials are active around their transition temperature. If the temperature span does not cover all material transition temperatures the layering is not optimal. These inactive layers take up precious magnetic volume and could be replaced with other materials. If the temperature span reported span all the transition temperatures, a (+) is set under Covers (Cov.). If the temperature span does not cover all transition temperatures, a (-) is set. The current work (c.w.) is listed as the last entry.

Table A.1: Experimental literature review of layered magnetocaloric regenerators.

Ref.	Materials	Tran. temp. (K)	-	Reg. Num.(-) x Mass (g)	Apl. B (T)	T_{span} (K)	Cov.	Q_c (W)
				Second Order Materials				
[23]	Gd, Tb	293, 235	-	1x500	0-7	24	-	-
[24]	Gd, $Gd_{.74}Tb_{.26}$	293, 278	-	2x90	0-2	19.5	+	-
[25]	Gd, $Gd_{.74}Tb_{.26}$, $Gd_{.85}Er_{.15}$	293, 278, 265	-	2x135	0-2	50	+	-
[107]	Gd, Gd.94Er.06	291, 280	-	-	0-1.5T	25	+	-
[27]	$Gd_{.89}Dy_{.11}$, $Gd_{.87}Dy_{.13}$, $Gd_{.84}Dy_{.16}$, $Gd_{.92}Y_{.08}$	283.5, 280.5, 277.5, 278.5	ΔT	4x250	0-0.77	7.5	+	60
[26]	Gd, $Gd_{.85}Er_{.15}$	293, 265	-	2x 68	0-5	59	+	1.94
[97]	$Gd_{1-x}Y_x$	291, 287, 282.5, 272	-	11x155	0-1.13	20	+	140
[98]	$Gd_{.985}Y_{.015}$, $Gd_{.95}Y_{.5}$, $Gd_{.9}Ho_{.1}$	290, 283.5, 277.5	-	1x100	0-1.1	40	+	-
[33]	$Gd_{1-x}Y_x$	291, 277	-	2x250	0.06-1.45	24.5	+	-

Ref.	Materials	Tran. temp. (K)	-	Reg. Num. (-) x Mass (g)	Apl. B (T)	T_{span} (K)	Cov.	Q_c (W)
[99]	$\mathrm{Gd_{1-x}Y_x}$	291, 277	-	2x225	0.06-1.45	40	+	-
				First Order Materials				
[103]	$\mathrm{La(Fe,Co,Si)_{13}}$	286, 289	-	1x71.3	0-1.03	8.5	+	-
[104]	$\mathrm{La(Fe,Co)_{13-x}Si_x}$	280, 295	-	-	0-1.45	16	+	-
[100]	$\mathrm{(La,Ca,Sr)MnO_3}$	273, 277	-	1x51.1	0-1.1	9.5	+	-
[105]	$\mathrm{La(FeCoSi)_{13}B_x}$	291, 279	ΔT	2x290	0-1.5	15.3	+	-
[101]	LaFeSiH	303.5, 306.2, 309.1, 311.6, 313.7, 316	-	4x380	0-1.44	17.7	+	3042
[28]	$\mathrm{La(Fe,Co)_{13-x}Si_x}$	283, 288, 293, 298.5	-	1x150	0-0.8	10.5	-	-
[31]	$\mathrm{LaFe_{13-x-y}Co_xSi_y}$	308, 303, 296.8, 291.2	-	1x144	0-1.15	20	+	
[29]	$\mathrm{La(Fe,Co)_{13-x}Si_x}$	301, 294, 287, 280	-	2x358	0-1.45	15.6	-	-

Ref.	Materials	Tran. temp. (K)	-	Reg. Num. (-) x Mass (g)	Apl. B (T)	T_{span} (K)	Cov.	Q_c (W)
[30]	$\mathrm{LaFe_{13-x-y}Co_xSi_y}$	286, 293	-	1x90	0-1.15	9	-	-
[120]	$\mathrm{La(Fe, Mn, Si)_{13}H_z}$	299.6 296	-	1x95	0-1.1	13.5	+	-
[22]	$\mathrm{MnFeAs_{1-x}P_x}$	302.9, 299.2, 295.3, 291.2, 287.5, 282.8, 279.0, 275.0	-	2x158	0.09-1.47	32	+	-
[102]	$\mathrm{La(Fe, Si, Mn)_{13}H_y}$	299.2, 294.7, 290.6, 286.7, 284.5	-	5x24.6	0-1.1	20.9	+	-
c. w.	$\mathrm{(MnFe)_x(SiP)}$	294.6, 292.3	-	2x23.45	0.09-1.47	8	+	-

Appendix B

Discretization Method

In this appendix the discretization methods of the governing equations are reported. The numerical methods are developed by Pantankar [121]. Moreover, the AMR numerical methods described in the work of Engelbrecht [76] and Trevizoli [108] are used to construct the numerical governing equations.

Fig. B.1 shows a sketch of the discretized 1D domain for solid and fluid along the nodes. The 0 and N nodes are ghost nodes used to apply the Neumann and Dirichlet boundary conditions as specified in Tab. 3.3 for the fluid and solid domain.

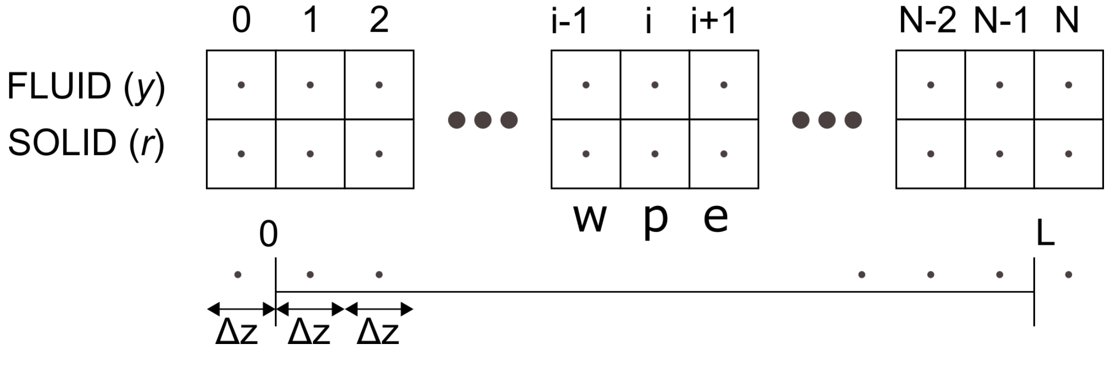

Figure B.1: Sketch of the numerical domain.

The time and space are discretized. The time is discretized for one cycle and the space is discretized along the length of the domain.

$$\Delta z = L/(N-1) \tag{B.1}$$

where Δz is the control volume length, L is the total length of the domain and N is the number of nodes

$$\Delta t = \frac{1}{f(nt+1)} \tag{B.2}$$

where Δt is the time step of the simulation, nt is the number of time nodes and f is the frequency of the device.

To simplify the notation of the governing equations and boundary conditions both fluid and solid temperature are non-dementionalized

$$y_i^n = \frac{T_{f,i}^n - T_{cold}}{T_{hot} - T_{cold}} \tag{B.3}$$

$$r_i^n = \frac{T_{r,i}^n - T_{cold}}{T_{hot} - T_{cold}} \tag{B.4}$$

where i is the spatial coordinate, n is the time coordinate in the cycle. y_i^n is non-dimentionalized temperature of the fluid and r_i^n is the non-dimentionalized temperature of the solid. $T_{r,i}^n$ and $T_{f,i}^n$ are the temperature of the solid and fluid for spatial coordinate i and time step n. T_{hot} is the hot side temperature, T_{cold} is the cold side temperature.

The calculated matrix is stored in $y_{cy,c}$ for the fluid and $r_{cy,c}$ for the solid while the previous cycle values are stored in the $y_{cy,p}$ for the fluid and $r_{cy,p}$ for the solid. The terms of the governing equation are converted to symbols to improve ease of programming of the numerical equations

$$C_{f,i}^n = \rho_f c_f A_{rh,i} \epsilon_i \tag{B.5}$$

$$C_{r,i}^n = \rho_{r,i}^n c_r A_{rh,i} \left(1 - \epsilon_i\right) \tag{B.6}$$

where

$$\rho_f = \rho_{f,i}^n w_o + \rho_{f,i}^{n-1}(1 - w_o) \tag{B.7}$$

$$c_f = c_{f,i}^n w_o + c_{f,i}^{n-1}(1 - w_o) \tag{B.8}$$

$$c_r = c_{r,i}^n w_o + c_{r,i}^{n-1}(1 - w_o) \tag{B.9}$$

where $C_{f,i}^n$ and $C_{r,i}^n$ are the capacitance of the fluid and solid determined for each node and timestep, $A_{rh,i}$ is the cross sectional area of the regenerator determined for each node, ϵ_i is the porosity determined for each node, $\rho_{r,i}^n$ is the density of the fluid and the solid determined for each node and timestep, ρ_f, c_f and c_r are fluid density, fluid specific heat and solid specific heat determined for each node and timestep, and w_o is the timestep averaging factor which is set to 0.5. Similar for fluid conduction coefficient and dynamic viscosity the values are averaged over the timestep.

$$\mu_f = \mu_{f,i}^n w_o + \mu_{f,i}^{n-1}(1 - w_o) \tag{B.10}$$

$$k_f = k_{f,i}^n w_o + k_{f,i}^{n-1}(1 - w_o) \tag{B.11}$$

The timestep average values are used to calculate the closure relationship values.

$$F_{f,i}^n = \dot{m}^n c_f \tag{B.12}$$

Where $F_{f,i}^n$ is the mass transport term determined for each node and timestep and $\dot{m}^n$ is the mass flow determined for each timestep. For the conduction the east and west node approach is taken as proposed by Patankar. In Fig. B.1 the location of the west and east node with respect to the present node are indicated by w, p, e, respectively.

$$K_{w,f,i}^{n} = \frac{1}{\Delta z} \left(\frac{0.5}{k_{\text{eff},f,i-1}^{n} A_{rh,i-1} \epsilon_{i-1}} + \frac{0.5}{k_{\text{eff},f,i}^{n} A_{rh,i} \epsilon_{i}} \right)^{-1} \tag{B.13}$$

$$K_{e,f,i}^{n} = \frac{1}{\Delta z} \left(\frac{0.5}{k_{\text{eff},f,i}^{n} A_{rh,i} \epsilon_{i}} + \frac{0.5}{k_{\text{eff},f,i+1}^{n} A_{rh,i+1} \epsilon_{i+1}} \right)^{-1} \tag{B.14}$$

Where, $K_{w,f,i}^{n}$ and $K_{e,f,i}^{n}$ is the fluid conduction term for the west and east node determined for each timestep at each node except nodes 0 and N, and $k_{\text{eff},f}^{n}$ is the effective conductivity of the fluid determined at each node and timestep. Similar for the solid domain these can be determined.

$$K_{w,r,i}^{n} = \frac{1}{\Delta z} \left(\frac{0.5}{k_{\text{eff},r,i-1}^{n} A_{rh,i-1} \left(1 - \epsilon_{i+1}\right)} + \frac{0.5}{k_{\text{eff},r,i}^{n} A_{rh,i} \left(1 - \epsilon_{i}\right)} \right)^{-1} \tag{B.15}$$

$$K_{e,r,i}^{n} = \frac{1}{\Delta z} \left(\frac{0.5}{k_{\text{eff},r,i}^{n} A_{rh,i} \left(1 - \epsilon_{i+1}\right)} + \frac{0.5}{k_{\text{eff},r,i+1}^{n} A_{rh,i+1} \left(1 - \epsilon_{i+1}\right)} \right)^{-1} \tag{B.16}$$

where $K_{w,r,i}^{n}$ and $K_{e,r,i}^{n}$ is the solid conduction term for the west and east node determined for each timestep at each node except the dummy nodes 0 and N, and $k_{\text{eff},r}^{n}$ is the effective conductivity of the solid determined at each node and timestep. The source terms for both fluid and solid domains are given by the following equations

$$S_{p,i}^{n} = \frac{\frac{\dot{m}^{n}}{\rho_f} \left| \frac{\partial p}{\partial z} \right|_{i}^{n}}{\left(T_{hot} - T_{cold}\right)} \tag{B.17}$$

where $S_{p,i}^{n}$ is the pressure drop loss term determined for each node and timestep, and $\left| \frac{\partial p}{\partial z} \right|_{i}^{n}$ is the pressure drop gradient determined at each node and timestep.

$$\mathrm{L}_{f,i}^{n} = P_{rh,i} U_{i}^{n} \tag{B.18}$$

where $\mathrm{L}_{f,i}^{n}$ is the ambient interaction term determined for each node and timestep, and $P_{rh,i}$ is the perimeter determined at each node, and U_{i}^{n} is the global heat transfer coefficient determined at each node and timestep.

$$\Omega_{f,i}^{n} = \Omega_{r,i}^{n} = A_{rh,i}\beta_i h_{e,i}^{n} \tag{B.19}$$

where $\Omega_{f,i}^{n}$ and $\Omega_{r,i}^{n}$ are the interstitial heat transfer term determined for each node and timestep, and β_i is the specific surface area per unit volume determined at each node, and $h_{e,i}^{n}$ is the interstitial heat transfer coefficient determined at each node and timestep.

$$S_{mce,i}^{n} = \rho_{r,i}^{n} A_{rh,i}\left(1-\epsilon_i\right)\frac{T_{r,i}^{n-1}\left(s_i^{n}-s_i^{n-1}\right)}{\left(T_{hot}-T_{cold}\right)\Delta t} \tag{B.20}$$

where $S_{mce,i}^{n}$ is the magnetocaloric energy term determined for each node and timestep, and $T_{r,i}^{n-1}$ is the temperature determined at each node from the previous time step, and s_i^{n} and s_i^{n-1} is the entropy determined at each node for the current and previous timestep. Given the governing equations a general upwinding discretization is formulated by integrating the terms with respect to time and node length. To implement upwinding two equations are constructed for fluid and solid. Upwinding is taken into account into the mass transfer term and the interstitial heat transfer term.

$F_f >= 0$

$$\begin{gathered} C_f\frac{y_i^{n}-y_i^{n-1}}{\Delta t}+\frac{1}{\Delta z}\left(F_{f,i}^{n}y_i^{n}-F_{f,i-1}^{n}y_{i-1}^{n}\right)+ \\ \frac{K_{f,w}}{\Delta z}\left(\frac{y_i^{n}+y_i^{n-1}}{2}-\frac{y_{i-1}^{n}+y_{i-1}^{n-1}}{2}\right)+\frac{K_{f,e}}{\Delta z}\left(\frac{y_i^{n}+y_i^{n-1}}{2}-\frac{y_{i+1}^{n}+y_{i+1}^{n-1}}{2}\right) \\ =S_p+\mathrm{L}_f\left(y_{amb}-\frac{y_i^{n}+y_i^{n-1}}{2}\right)+\Omega_f\left(\frac{r_i^{n}+r_i^{n-1}}{2}-\frac{y_i^{n}+y_{i-1}^{n-1}}{2}\right) \end{gathered} \tag{B.21}$$

$F_f < 0$

$$\begin{aligned} C_f \frac{y_i^n - y_i^{n-1}}{\Delta t} + \frac{1}{\Delta z}\left(F_{f,i+1}^n y_{i+1}^n - F_{f,i}^n y_i^n\right) + \\ \frac{K_{f,w}}{\Delta z}\left(\frac{y_i^n + y_i^{n-1}}{2} - \frac{y_{i-1}^n + y_{i-1}^{n-1}}{2}\right) + \frac{K_{f,e}}{\Delta z}\left(\frac{y_i^n + y_i^{n-1}}{2} - \frac{y_{i+1}^n + y_{i+1}^{n-1}}{2}\right) \\ = S_p + \mathrm{L}_f\left(y_{amb} - \frac{y_i^n + y_i^{n-1}}{2}\right) + \Omega_f\left(\frac{r_i^n + r_i^{n-1}}{2} - \frac{y_i^n + y_{i+1}^{n-1}}{2}\right) \end{aligned} \tag{B.22}$$

For solid only upwinding needs to be taken into account in the interstitial heat transfer term.

$F_f >= 0$

$$\begin{aligned} C_r \frac{r_i^n - r_i^{n-1}}{\Delta t} + \frac{K_{r,w}}{\Delta z}\left(\frac{r_i^n + r_i^{n-1}}{2} - \frac{r_{i-1}^n + r_{i-1}^{n-1}}{2}\right) + \frac{K_{r,e}}{\Delta z}\left(\frac{r_i^n + r_i^{n-1}}{2} - \frac{r_{i+1}^n + r_{i+1}^{n-1}}{2}\right) \\ = S_{MCE} + \Omega_r\left(\frac{y_i^n + y_{i-1}^n}{2} - \frac{r_i^n + r_i^{n-1}}{2}\right) \end{aligned} \tag{B.23}$$

$F_f < 0$

$$\begin{aligned} C_s \frac{r_i^n - r_i^{n-1}}{\Delta t} + \frac{K_{r,w}}{\Delta z}\left(\frac{r_i^n + r_i^{n-1}}{2} - \frac{r_{i-1}^n + r_{i-1}^{n-1}}{2}\right) + \frac{K_{r,e}}{\Delta z}\left(\frac{r_i^n + r_i^{n-1}}{2} - \frac{r_{i+1}^n + r_{i+1}^{n-1}}{2}\right) \\ = S_{MCE} + \Omega_r\left(\frac{y_i^n + y_{i+1}^n}{2} - \frac{r_i^n + r_i^{n-1}}{2}\right) \end{aligned} \tag{B.24}$$

These equations are reformulated into the form Eq. B.25 and Eq. B.26 through which the tri-diagonal matrices are constructed.

$$a_f y_{i-1}^n + b_f y_i^n + c_f y_{i+1}^n = d_f \tag{B.25}$$

$$a_r r_{i-1}^n + b_r r_i^n + c_r r_{i+1}^n = d_r \tag{B.26}$$

For the upwind case referred to in Chapter 3 uses the following equations:

$$F^n_{f,i} \geq 0$$

$$a_f = -\frac{F^n_{f,i-1}}{\Delta z} - \frac{K^n_{f,w,i}}{2\Delta z} + \frac{\Omega^n_{f,i}}{2} \tag{B.27}$$

$$b_f = \frac{C^n_{f,i}}{\Delta t} + \frac{F^n_{f,i}}{\Delta z} + \frac{K^n_{f,w,i}}{2\Delta z} + \frac{K^n_{f,e,i}}{2\Delta z} + \frac{\mathrm{L}^n_{f,i}}{2} + \frac{\Omega^n_{f,i}}{2} \tag{B.28}$$

$$c_f = -\frac{K^n_{f,e,i}}{2\Delta z} \tag{B.29}$$

$$\begin{aligned} d_f = & y^{n-1}_{i-1}\left[\frac{K^n_{f,w,i}}{2\Delta z}\right] + \\ & y^{n-1}_{i}\left[\frac{C^n_{f,i}}{\Delta t} - \frac{K^n_{f,w,i}}{2\Delta z} - \frac{K^n_{f,e,i}}{2\Delta z} + \frac{\mathrm{L}^n_{f,i}}{2}\right] + \\ & y^{n-1}_{i-1}\left[\frac{K^n_{f,e,i}}{2\Delta z}\right] + \\ & y_{amb,i}\left[\mathrm{L}^n_{f,i}\right] + r^n_i\left[\frac{\Omega^n_{f,i}}{2}\right] + r^{n-1}_i\left[\frac{\Omega^n_{f,i}}{2}\right] + S^n_{p,i} \end{aligned} \tag{B.30}$$

$$F^n_{f,i} < 0$$

$$a_f = -\frac{K^n_{f,w,i}}{2\Delta z} \tag{B.31}$$

$$b_f = \frac{C^n_{f,i}}{\Delta t} - \frac{F^n_{f,i}}{\Delta z} + \frac{K^n_{f,w,i}}{2\Delta z} + \frac{K^n_{f,e,i}}{2\Delta z} + \frac{\mathrm{L}^n_{f,i}}{2} + \frac{\Omega^n_{f,i}}{2} \tag{B.32}$$

$$c_f = \frac{F^n_{f,i+1}}{\Delta z} - \frac{K^n_{f,e,i}}{2\Delta z} + \frac{\Omega^n_{f,i}}{2} \tag{B.33}$$

$$\begin{aligned} d_f = & y^{n-1}_{i-1}\left[\frac{K^n_{f,w,i}}{2\Delta z}\right] + \\ & y^{n-1}_{i}\left[\frac{C^n_{f,i}}{\Delta t} - \frac{K^n_{f,w,i}}{2\Delta z} - \frac{K^n_{f,e,i}}{2\Delta z} - \frac{\mathrm{L}^n_{f,i}}{2}\right] + \\ & y^{n-1}_{i+1}\left[\frac{K^n_{f,e,i}}{2\Delta z}\right] + \\ & y_{amb,i}\left[\mathrm{L}^n_{f,i}\right] + r^n_i\left[\frac{\Omega^n_{f,i}}{2}\right] + r^{n-1}_i\left[\frac{\Omega^n_{f,i}}{2}\right] + S^n_{p,i} \end{aligned} \tag{B.34}$$

The upwind case discussed in Chapter 3 for solid the following equations are used:

$$F_{f,i}^{n} \geq$$

$$a_r = -\frac{K_{r,w,i}^{n}}{2\Delta z} \tag{B.35}$$

$$b_r = \frac{C_{r,i}^{n}}{\Delta t} + \frac{K_{r,w,i}^{n}}{2\Delta z} + \frac{K_{r,e,i}^{n}}{2\Delta z} + \frac{\Omega_{r,i}^{n}}{2} \tag{B.36}$$

$$c_r = -\frac{K_{r,e,i}^{n}}{2\Delta z} \tag{B.37}$$

$$\begin{aligned} d_r = & r_{i-1}^{n-1}\left[\frac{K_{r,w,i}^{n}}{2\Delta z}\right] + \\ & r_{i}^{n-1}\left[\frac{C_{r,i}^{n}}{\Delta t} - \frac{K_{r,w,i}^{n}}{2\Delta z} - \frac{K_{r,e,i}^{n}}{2\Delta z} - \frac{\Omega_{r,i}^{n}}{2}\right] + \\ & r_{i+1}^{n-1}\left[\frac{K_{r,e,i}^{n}}{2\Delta z}\right] + \\ & y_{i}^{n}\left[\frac{\Omega_{r,i}^{n}}{2}\right] + y_{i+1}^{n}\left[\frac{\Omega_{r,i}^{n}}{2}\right] + S_{MCE,i}^{n} \end{aligned} \tag{B.38}$$

$$F_{f,i}^{n} < 0$$

$$a_r = -\frac{K_{r,w,i}^{n}}{2\Delta z} \tag{B.39}$$

$$b_r = \frac{C_{r,i}^{n}}{\Delta t} + \frac{K_{r,w,i}^{n}}{2\Delta z} + \frac{K_{r,e,i}^{n}}{2\Delta z} + \frac{\Omega_{r,i}^{n}}{2} \tag{B.40}$$

$$c_r = -\frac{K_{r,e,i}^{n}}{2\Delta z} \tag{B.41}$$

$$\begin{aligned} d_r = & r_{i-1}^{n-1}\left[\frac{K_{r,w,i}^{n}}{2\Delta z}\right] + \\ & r_{i}^{n-1}\left[\frac{C_{r,i}^{n}}{\Delta t} - \frac{K_{r,w,i}^{n}}{2\Delta z} - \frac{K_{r,e,i}^{n}}{2\Delta z} - \frac{\Omega_{s,i}^{n}}{2}\right] + \\ & r_{i+1}^{n-1}\left[\frac{K_{r,e,i}^{n}}{2\Delta z}\right] + \\ & y_{i}^{n}\left[\frac{\Omega_{r,i}^{n}}{2}\right] + y_{i+1}^{n}\left[\frac{\Omega_{r,i}^{n}}{2}\right] + S_{MCE,i}^{n} \end{aligned} \tag{B.42}$$

A generalized power law formulation is implemented to improves the speed of the simulation.

$$F_{f,i}^{n} \geq 0$$

$$\Delta_w = \max\left(0, 1 - 0.1\left|\frac{F_{f,i-1}^{n}}{K_{f,w,i}^{n}}\right|^5\right) \tag{B.43}$$

$$\Delta_e = \max\left(0, 1 - 0.1\left|\frac{F_{f,i}^{n}}{K_{f,e,i}^{n}}\right|^5\right) \tag{B.44}$$

$$F_{f,i}^{n} < 0$$

$$\Delta_w = \max\left(0, 1 - 0.1\left|\frac{F_{f,i}^{n}}{K_{f,w,i}^{n}}\right|^5\right) \tag{B.45}$$

$$\Delta_e = \max\left(0, 1 - 0.1\left|\frac{F_{f,i+1}^{n}}{K_{f,e,i}^{n}}\right|^5\right) \tag{B.46}$$

$$\tag{B.47}$$

The power law adaptations modify the conduction term as shown in Eq. B.48 and Eq. B.49.

$$K_{f,w,i}^{n} = \Delta_w K_{f,w,i}^{n} \tag{B.48}$$

$$K_{f,e,i}^{n} = \Delta_e K_{f,e,i}^{n} \tag{B.49}$$

After constructing the tridiagonal matrices the boundary conditions are applied using the following equations for fluid:

$$F_i^n \geq 0$$

$$d_{f,1} = d_{f,1} - a_{f,1} \cdot [y_{cold} = 0] \tag{B.50}$$

$$b_{f,N-1} = b_{f,N-1} - c_{f,N-1} \tag{B.51}$$

$$F_i^n < 0$$

$$b_{f,1} = b_{f,1} - c_{f,1} \tag{B.52}$$

$$d_{f,N-1} = d_{f,N-1} - a_{f,N-1} \cdot [y_{hot} = 1] \tag{B.53}$$

and solid:

$$b_{r,1} = b_{r,1} - c_{r,1} \tag{B.54}$$

$$b_{r,N-1} = b_{r,N-1} - c_{r,N-1} \tag{B.55}$$

The timestep is computed until the tolerance between the guess values and the values is less than variable stepping tolerance δ_{var}. The variable stepping tolerance solves the entire cycle first at $1e-2$, than goes down to $1e-3$, until $1e-6$ is reached. It was found that using a coarser tolerance for the initial computed cycled improved the speed of the simulation.

$$\delta_{var} > |y^n - y^n_{\text{Prev.Guessed}}| \text{ AND } \delta_{var} > |r^n - r^n_{\text{Prev.Guessed}}| \tag{B.56}$$

At the end of each cycle the first row of y and r are replaced with the last value of the cycle.

$$y^0 = y^{nt} \tag{B.57}$$

$$r^0 = r^{nt} \tag{B.58}$$

$$\tag{B.59}$$

The cycle steady state is reached when the following condition is met.

$$1e - 6 > |y_{cy} - y_{cy,\text{Prev.Guessed}}| \text{ AND } 1e - 6 > |y_{cy} - y_{cy,\text{Prev.Guessed}}| \tag{B.60}$$

The gross cooling power is then computed using the following equation.

$$T_{ave}^n = \frac{T_{f,1}^n + T_{f,1}^{n+1}}{2} \tag{B.61}$$

$$Q_{gr} = f \sum_{n=0}^{nt} c_f \dot{m}^n \Delta t \left(T_{ave}^n - T_{cold}\right) \tag{B.62}$$

Appendix C

Purging Manual for PMMR 1

In this appendix a standardized protocol is outlined to remove all air bubbles from the PM1 system. Purging the PM 1 of all air is important to ensure incompressible flow. Below in Fig. C.1 is an image that outline the labeling scheme. Tab. C.1 outlines the steps to be taken. Values are to be opened or closed after which the flow of the external pump system should be directed as indicated by the table.

Duration:

The first two steps (flush section) should take between 15 and 25 min. Then every subsequent step should take 15 min (except for the purge stage which should be done after several seconds).

The Purge Tool Step:

Connected to the pump are a number of valves and tubes. The middle part is removed to connect to the PM1 device. By using this tool we prevent the issue of when removing and reconnecting the tubes air getting into the system. Purging the tool is important because between switch of the flow direction with the tool there is some air in the tool. Keep the pump running and open up all the valves on the tool. Then close the valves on the tool to get the appropriate flow direction.

Meaning of “o”,“c” & “c(o)”:

In the table below “o” indicate that the valve should be opened and “c” indicates that it should be closed. Going from 1→2 for the first time you open (f) and (e) to get the air out of the tube, then (e) and (f) can be closed for the remaining duration of the step. This is indicated by “c(o)”.

Comment on the Last Step:

During the last step over the cold hex you can really turn up the speed of the pump without harming the material.

Table C.1: Steps to purge the PM1.

	flow	valve number						
STEP	from to	A	B	C	D	E	F	G
1	2→1	**o**	**o**	**o**	**o**	**c**	**c**	**c**
2		purge tool						
3	1→2	**o**	**o**	**o**	**o**	**c(o)**	**c(o)**	**c**
4	1→2	**o**	**c**	**c**	**o**	**o**	**o**	**c**
5		purge tool						
6	2→1	**o**	**c**	**c**	**o**	**o**	**o**	**c**
7	2→3	**c**	**o**	**o**	**o**	**c**	**c**	**o**
8		purge tool						
9	3→2	**c**	**o**	**o**	**o**	**c**	**c**	**o**
10	3→2	**c**	**c**	**c**	**o**	**o**	**o**	**o**
11		purge tool						
12	2→3	**c**	**c**	**c**	**o**	**o**	**o**	**o**

Pressurize system

relieve R1, R2

Re-pressurize system

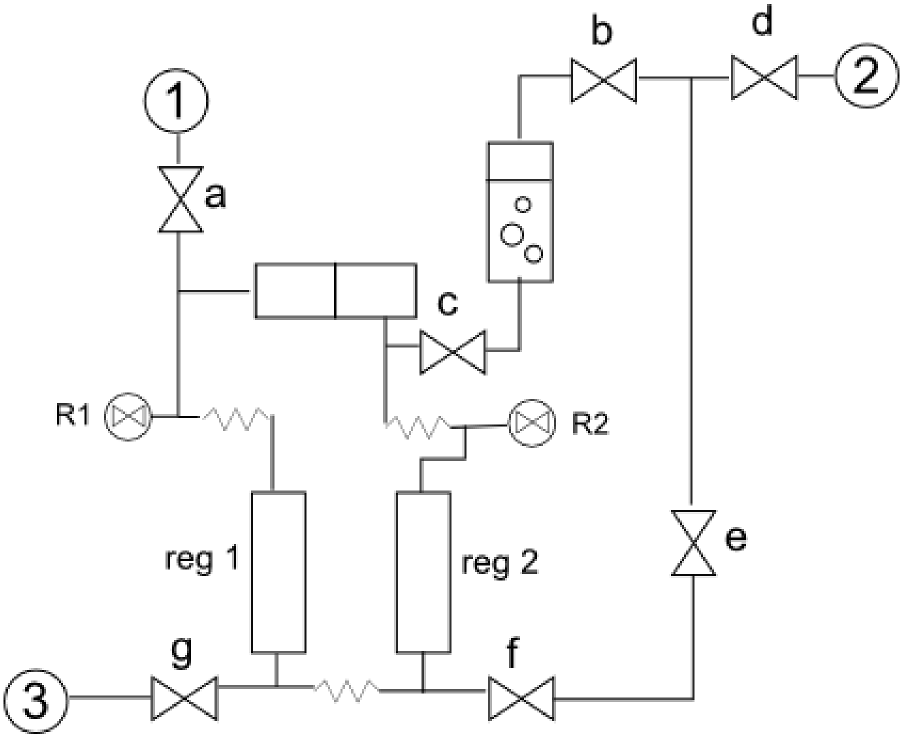

Figure C.1: Naming convention of the PM1 valves.

Appendix D

PM1 Adaptations

In this appendix the upgrades to the system are documented. Two aspect of the PM1 device are critically studied. First the device was analyzed to see if there are any new places where the ambient heat interactions could be improved. The second was to look into the steady state criteria and experimental procedure of the PM1 device.

D.1 Heat Leak Improvements PM1

An analysis of the PM1 was done to see if there are any places where heat leak improvements could be made to the PM1 device. Fig. D.1 depicts a cut through of the PM1 system. On the left are the cold heat exchangers and on the right are the hot side heat exchangers. The inner flanges connect the regenerator to the outer housing components. These flanges are made of aluminum which easily allows for heat conduction between the lab and the regenerator. These aluminum inner flanges are replaced with Ultem material. The Ultem improves the insulation of the regenerator housing by increasing the thermal resistance.

The performance impact of the new flanges is determined by redoing the short centre and cold side beds from Chapter 3. In Fig. D.2 (a) the result of the center beds are plotted. The results shown for the 0 W results are limited to a range to ambient temperatures of 20.5 ± 0.5 °C. In Fig. D.2 (b) the results of the cold side

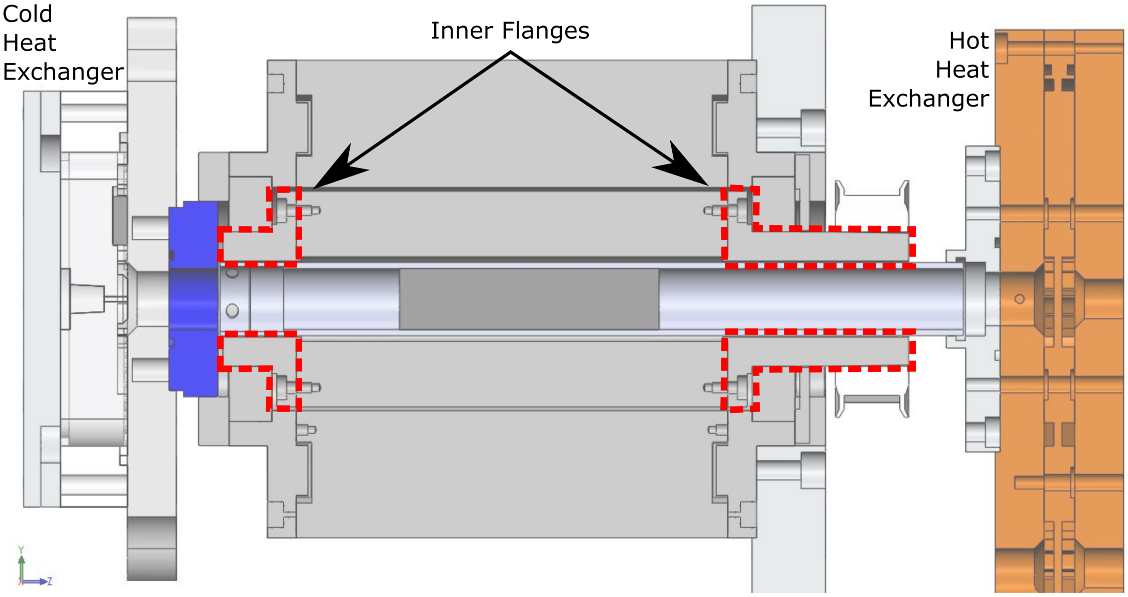

Figure D.1: Cut through of the PM1

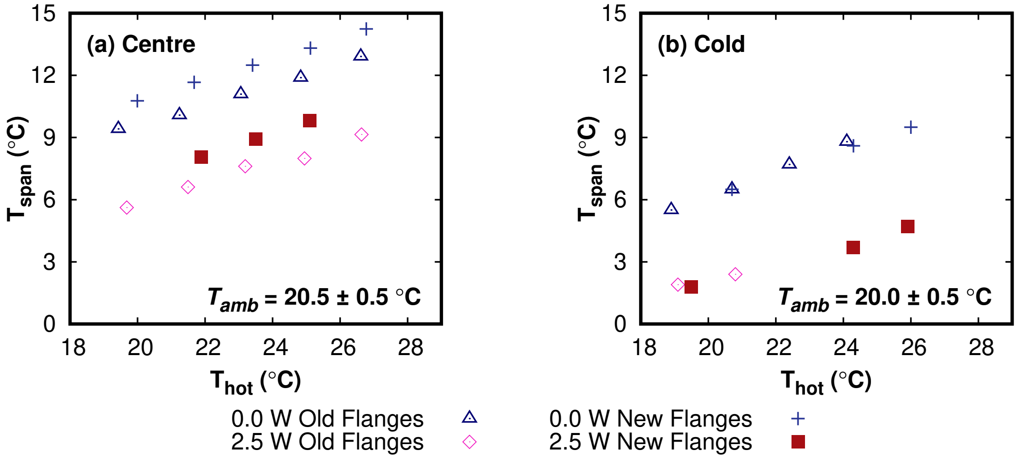

Figure D.2: A comparison between the steady state temperature span results with the new and old flanges. (a) The center beds experimental temperature span steady state points for $T_{amb} = 20.5 \pm 0.5$ °C. (b) The cold beds experimental temperature span steady state points for $T_{amb} = 20.0 \pm 0.5$ °C.

beds are shown. The results for the 0 W and the 2.5 W are are limited to an ambient temperature of 20.5 ± 0.5 °C.

The zero Watt curve results improve in temperature span with the new flanges. On average a 2 K temperature span improvement is found. Similar for the 2.5 W curve for rejection temperatures an increase in temperature span of 2 K is found. For the cold side beds; however, no improvement is found on the temperature span.

By removing the thermal conductor of the inner magnet to the outer components this magnet becomes a insulator of the center bed. However, the main leak of the cold side bed is probably the cold heat exchanger which is still in contact.

D.2 New DAQ of the PM1

The PM1 system is build to stress test the performance of a regenerator at different hot side temperatures. The protocol we developed is to measure the temperature span created by the device at a set hot side temperature and cooling load. The hot side temperature is set by using heat exchangers on the hot side of the device. These are connected to a chiller to maintain a set hot side temperature. The cooling load is applied by adding an electric resistor pad to the cold heat exchanger. After fixing the chiller setting and applying cooling load the system is set to run at a fixed frequency and displaced volume. When the temperature span remains constant for a long period of time the system is considered in steady state and these values are recorded.

The old procedure was to log the results by allowing the DAQ software to output 1000 rows of data, which represents about 10 seconds of running the device. The various sensory data stored in the columns would be averaged and logged as the steady state point values for the experimental set parameters.

The system is upgraded to do automatic recording of these files during the experiment to capture the transients. Furthermore, a control component is added to define a strict definition of what constitutes steady state in a lab where the ambient temperature is constantly varying.

Several additional temperature sensors are installed to provide more details of the adjacent system components. In Tab. D.1 comparisons of the features of the software are listed.

The most important sensor that was added was the ambient temperature of the lab. As will be discussed more extensively in Chapter 4 the small temperature variations in the lab impact the regenerator performance. By recording the temperature in the lab at each acquired steady state point this can be more accounted for.

The new software records about eight seconds of data points every three minutes. These eight seconds are approximately 1000 data points that are written into a file. These files are later used to do a post analysis of the experimental data. The temperature span values are calculated by the software and monitored during the experiment. These values are used to determine if the device has reached a steady state point. In Eq. D.1 the rule is given to determine steady state

$$T_{span}^{n} - T_{span}^{n-4} \begin{cases} < SS_{criteria} & \text{Steady state reached} \\ \geq SS_{criteria} & \text{Not steady state} \end{cases} \tag{D.1}$$

Table D.1: A comparison between the old and new software of the PM1 system.

	Old Labview Sofware	New Labview Software
Data Recorded	Hot side temperature, Cold side temperature, pressure signal, pressure drop, frequency	Hot side temperature, Cold side temperature, pressure signal, pressure drop, frequency, Ambient Temperature, chiller inlet flow temperature, chiller outlet flow temperature, Outer magnet shell temperature, Outer cold side flange temperature
Store Data	Operator controlled	Automatic recording every 3 minutes
Control	Operator controlled	Automatic chiller temperature changes based using the SS-criteria to determine steady state

where T^{n}_{span} is the averaged temperature span value at the nth measurement of the experiment. The $SS_{criteria}$ is used to determine the amount of variation on the temperature span that determines when the next hot side temperature can be set.

After the steady state criteria is reached the new DAQ software will record a last point of the steady state and set a new chiller temperature. Before it starts checking the steady state criteria it has to wait for 40 min. This allows for enough time for the chiller to reach its temperature and the large thermal mass of the magnets which is strongly dependent on the hot side temperature to settle to its steady state.

Post analysis of the measured data is done using an R script. [1] The R script does all the averaging and outputs two files. A file that contains all the measured values throughout the entire experiment and a file that contains just the steady state points.

---

[1] The R processing script can be found at: `https://github.com/TheoChristiaanse/ExperimentalSearchAndProcess`

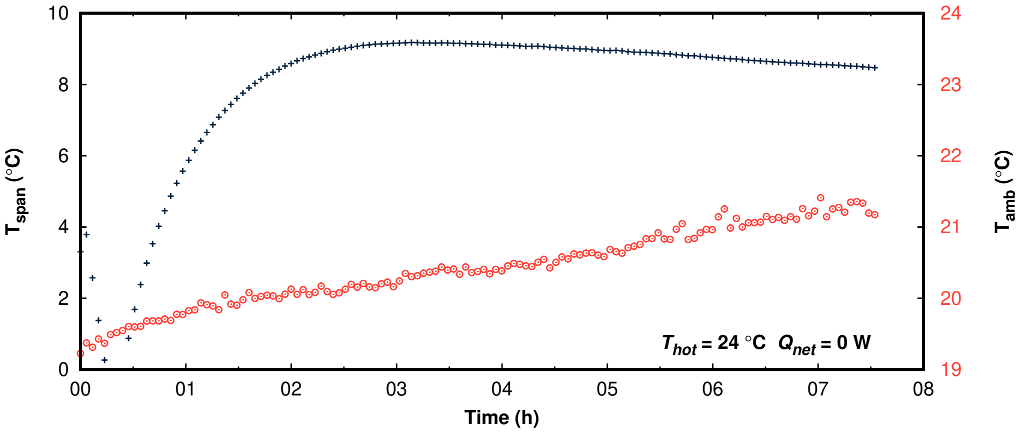

Figure D.3: The temperature span development over several hours of running the PM1 in the lab.

D.2.1 Sweeping Different Points Versus Long Settle

Sweeping the points is efficient; however, we need to determine the impact of this intermediate state and letting the device settle for several hours. The cold side short bed configuration from Chapter 3 is rebuilt in the PM1 device to look at the steady state criteria.

In this section we compare steady state points found in the device in two ways. First we take several hot side steady state points using hot side sweeping method and steady state criteria as described in the previous section. Then several hot side temperatures of the device will be fixed and the device will be run an entire day with this single hot side temperature.

By allowing the device to run for many hours the device will operate in steady state, responding only to the varying ambient temperature in the lab.

In Fig. D.3 we have plotted an example long run of the cold side beds at 24 °C hot side and 0 W cooling power.

The temperature span is collapsed at the start of the experiment by turning up the cooling power to 15 W. When the temperature span reaches zero the cooling power is turned off. Then the temperature span develops. After two hours the maximum temperature span is reached. The ambient temperature increases in the lab,

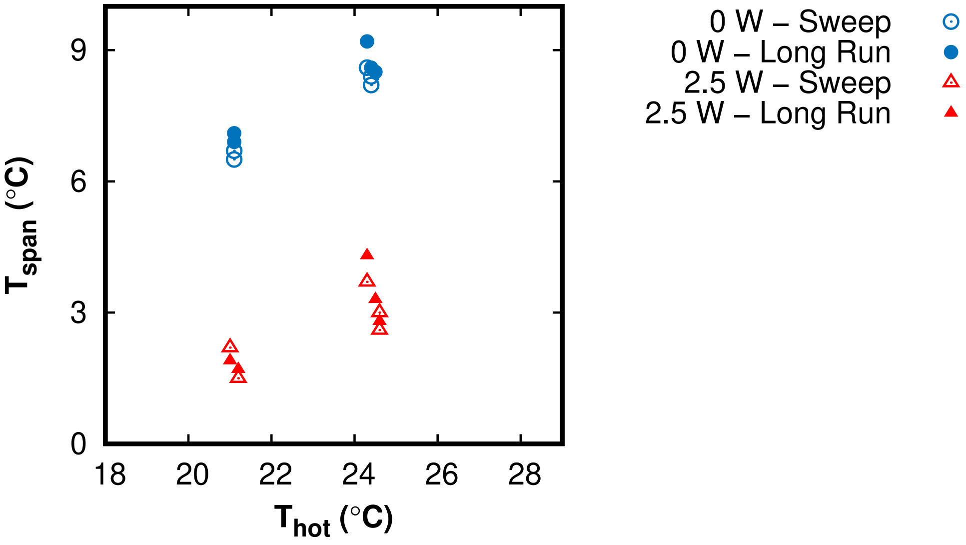

Figure D.4: A comparison between sweeping and long run of the PM1 steady state-points.

increasing the cooling load on the cold heat exchanger and reducing the temperature span. The temperature span is continuously adapting to the ambient temperature variation; however, during this time the device would be considered steady state since the variation is small.

The rate of variation of the temperature span due to the changing ambient temperature is 0.03 K/12 min. This value is the minimal value which can be set as the automated steady state criteria if multiple points are to be done.

In Fig. D.3 we have compared the values obtained from the automated sweep and the values that are found along this long run. The open markers are the values from the automated sweep while the closed markers are taken from the long runs. Two hot side temperatures at two different cooling powers are selected. To find corresponding values from the long run to the automated sweep steady state points for some ambient temperatures the values are extrapolated. A linear regression is made of the steady state temperature span with respect to ambient temperature in the long run. This fit is used to find the values of the 20 °C 0 W case.

The largest variation is found for the 24 °C 2.5 W measurement. The difference between the lowest value and the highest value is 1.7 K. However, when ambient temperature is taken into account the temperature span variation between the methods is +0.7 K and -0.3 K. The steady state points taken with the sweep tend to under-predict the temperature span compared to the values obtained from the long run experimental data.